TECHNISCHE UNIVERSITÄT WIEN
Vienna University of Technology

HEPHY
INSTITUT FÜR HOCHENERGIEPHYSIK

DIPLOMARBEIT

Enhancing the Electromagnetic Background Model in the CRESST Experiment by Considering Surface-Induced Contamination using Measured Surface Roughness

zur Erlangung des akademischen Grades

Diplom-Ingenieur

im Rahmen des Studiums

Masterstudium Technische Physik

eingereicht von

Christoph Grüner
Matrikelnummer 01429139

ausgeführt am Institut für Atomphysik
der Fakultät Physik der Technischen Universität Wien
in Zusammenarbeit mit dem Institut für Hochenergiephysik

Betreuung:
Univ.-Prof. Dipl.-Phys. Dr. Jochen Schieck
Dr. Valentyna Mokina
Dr. Samir Banik

Wien, 09.09.2024 ______________________ ______________________
(Unterschrift Verfasser) (Unterschrift Betreuer)

Abstract

For decades, CRESST (Cryogenic Rare Event Search with Superconducting Thermometers) experiment is one of the leading experiments searching for Dark Matter. With cryogenic ($\sim$ 15 mK) detectors using different crystals as a target material, it is well suited to search for Weakly Interacting Massive Particles with masses in the sub-GeV range ($\lesssim 1$ GeV).
A simulation-based background model was developed to understand the components of measured background. The latest version of which by only considering bulk contamination already explains $\sim 76.1\,\%$ of the observed background. However, a first study investigating the effects of surface roughness and surface contamination of CRESST's crystals shows that these two properties can explain differences between measured and simulated data.
In this thesis, I am working on well-known and very challenging problem of simulating surface roughness and its contamination, which many rare event search experiments suffer from. I have developed a novel framework which can be used to replicate a crystal surface-roughness profile and simulate its effects on the energy deposition spectra in the crystal. This work consisted of two major parts: a) developing a model allowing a user to define different kinds of surface structures in the order of microns, and b) optimizing existing Geant4 models to accurately simulate interactions on and in the rough surface. Using this framework, I investigated the contributions of most probable contaminants, such as ^{210}Po and ^{238}U, to the measured spectrum by CRESST. This work carried out in the thesis led to an improved electromagnetic background model for the CRESST experiment.

Kurzfassung

Seit Jahrzehnten ist das CRESST (Cryogenic Rare Event Search with Superconducting Thermometers) Experiment eines der führenden Experimente auf der Suche nach Dunkler Materie. Durch die Verwendung von cryogene ($\sim 15\,\mathrm{mK}$) Detektoren, ist es bestens gerüstet für die suche nach Weakly Interacting Massive Particles mit Massen im sub-GeV Bereich ($\lesssim 1\,\mathrm{GeV}$).
Um den gemessenen Hintergrund zu analysieren, wurde ein simulation-basiertes Hintergrundmodell entwickelt. Bereits unter der Annahme einer homogenen Kristallverunreinigung kann das Modell $\sim 76.1\,\%$ des Hintergrunds erklären. Eine erste Studie zeigt jedoch, dass Effekte durch Oberflächen-Rauigkeit und Verunreinigung einige der Differenzen zwischen der Simulation und den Messdaten erklären können.
In dieser Arbeit behandle ich das bekannte Problem von Oberflächenrauhigkeitssimulationen und deren Verunreinigung, welchem viele Experimente auf der Suche nach "Rare Events" gegenüber stehen. Dafür entwickelte ich ein neues Framework welches die Oberflächenrauhigkeit eines Kristalles nachbilden und dessen Effekte auf das Energieeintragsspektrum simulieren kann. Die Arbeit beinhaltet zwei wesentliche Punkte: a) Entwicklung eines Modells um Oberflächenrauhigkeit in der Grössenordnung von Mikrometern zu simulieren; b) Optimierung der Geant4 basierenden Modelle um akurate Simulationen in der rauen Oberfläche durchzuführen. Mit diesem Framework untersuche ich die Beiträge verschiedener Verunreinigungen, wie beispielsweise ^{210}Po und ^{238}U, zum gemessenen Hintergrundspektrum von CRESST. Diese Arbeit fühte in Folge zu einem verbesserten elektromagnetischen Hintergrundmodell für das CRESST Experiment.

Contents

1 Introduction

More than 90 years ago, the first evidence for Dark Matter (DM) was found. Since then the search for DM has been one of the hot topics of our time in cosmology and astrobiology. Today we have clear evidence that there is roughly five times more DM than baryonic matter [1]. It's effect can be found on different macroscopic scales starting at single galaxies, to galaxy clusters to the scale of the Cosmic Microwave Background (CMB) [2].

Many different ideas arise from there explaining the observations, some of them by modifying the gravitation on big scales, the so-called MOdified Newton Dynamics (MOND) theories [3], others use already known particles like right handed neutrinos [4], or assume super massive black holes [5] however many of them introduce new particles like axions or Weakly Interacting Massive Particles (WIMPs) [6, 7]. To find particle type of DM, different search techniques are employed in direct-, indirect- and collider-based searches. The review of our current DM knowledge and search methods can be found in chapter 2.

The Cryogenic Rare Event Search with Superconducting Thermometers (CRESST) experiment is at the forefront in DM research by direct interaction, measuring DM recoil off nuclei. Located at Laboratori Nazionali del Gran Sasso (LNGS) in Italy below the Gran Sasso massive it employs cold crystals ($\sim 15\,\mathrm{mK}$) to probe the parameter space for WIMPs with sub-GeV mass ($\lesssim 1\,\mathrm{GeV}/c^2$), capable of detecting recoil events down to $10\,\mathrm{eV}$ and lower. Different detector materials are used [8–10], e.g. $CaWO_4$. Multiple shielding and other precautions help reduce the background measured by CRESST. Using scintillating crystals such as $CaWO_4$ allows CRESST to employ a two-channel approach, which allows particle discrimination. However, the origin of some background remains unclear. A more detailed description of the experiment, the detector modules TUM40 and TUM93A and different background sources can be found in chapter 3.

For a better understanding of the measured data, a background model was developed and its state is discussed in chapter 5. A Monte Carlo (MC) based approach is used to simulate decay processes and particle interactions within the experimental setup of CRESST. For that ImpCRESST [11] a Geant4 and Root based simulation tool was developed, explicitly to be used in rare event search experiments and is primarily used by CRESST. The simulated templates are fitted to the measurement data using the software Bliss [12] which utilizes a likelihood normalization fit method. The model used, which only considers bulk contamination, can explain a large share of the data measured by CRESST, however, some discrepancies are observable and must be investigated [11, 12].

These differences suggest either that some sources not accounted for in the simulation or that some characteristics of the experiment are not well represented in the simulations. A missing source can be ^{210}Pb, which is part of the ^{222}Rn decay chain. ^{222}Rn is a naturally occurring radioactive gas. Exposure of the detector module (particularly crystals after growth and during cutting and polishing/diffusing the surface) to airborne ^{222}Rn can lead to an accumulation of ^{210}Pb at the surface which has a half-life of $\sim 22.2\,\mathrm{yrs}$ and can result in continuous decay during measurement, contributing to different energy ranges. ^{210}Po, which is in the sub-chain of ^{210}Pb is α decaying and can therefore introduce energies up to several MeV. Although it has a fixed decay energy signature, if it decays in the vicinity of a surface, an interaction with the surface can result in an unclear signature, leading to deposited energy of any amount, also affecting the region of interest (ROI) for DM. This effect can be further reinforced by a rough surface, which changes the likelihood of decay products escaping the surface while depositing a share of their energy. A first investigation, conducted by me and discussed in [13], simulating ^{210}Po nuclei placed exactly on a simple rough surface, approximated by similar looking spikes with heights and widths in the µm range, confirmed this assumption of partially deposited energy and its potential impact on the measured electromagnetic background. The further study indicates that the depth of implantation of contaminants in the vicinity of the surface has a non-negligible influence too. Many of the detector crystals used by CRESST are diffused, an investigation showed that this diffused/roughened surface has structures on the scale of µm. Therefore, adding rough surfaces combined with the implantation of contaminants below the surface to the background model of CRESST is of absolute importance. This problem is not specific to CRESST, but to many rare event search experiments, such as CUORE, COSINE-100 or AMoRE, employing solid crystals as detectors face [14, 15].

In this thesis, I developed a Geant4/C++ library to simulate measured rough surfaces and their contamination by placing nuclei below the surface. I extended the simple surface generator from [13] that simulates a small patch of rough surface to cover any size of area. I overcame the memory limitation due to a large number of simulated volumes by introducing the concept of a portal which allows to reuse already placed volumes, thereby enabling to simulate rough surfaces of any size. I enhance the particle generator for the placement of nuclei to be compatible with portals and introduced a shift to permit more realistic surface contamination by placing nuclei below the surface, following any self-defined distribution. The developed module and the other used simulation and fitting tools are described in chapter 4.

Further in chapter 6 I test the spatial accuracy of the physics model used to simulate nuclear recoil, which was used in the previous surface simulation [13]. This is of importance to yield realistic surface simulations. Lastly, based on the developed module I simulate energy deposition templates for ^{210}Po and ^{238}U placed as a surface contamination of a rough surface, as a test case for the TUM40 $CaWO_4$ crystal. I test different distributions of contaminants below the rough surface of the TUM40 crystal and simulate a realistic distribution of ^{210}Po based on the whole ^{222}Rn decay chain. In addition, a potential contribution from rough contaminated surfaces facing the detector crystal was investigated.

The findings of simulating different surface sources and different implantation distributions are used to simulate realistic energy deposition templates and fit them to the TUM40 data using Bliss and thereby improving the electromagnetic background model of CRESST. Based on the fit of the templates, surface activity can be calculated. Finally, the same findings are applied, to generate surface contamination-dependent energy deposition templates for the TUM93A crystal and to extend its background model too.

In chapter 7 I summarize all results and elaborate further improvements to get a clearer picture of the influence of surface contamination and surface roughness in the CRESST experiment.

2 Dark Matter

The term DM was introduced at the beginning of the last century and describes non-visible and gravitationally interacting matter. However, the idea of invisible or dark objects in the universe is much older. In 1846 the planet Neptune was found just by observing the motion of the planet Uranus, which was slightly off to its predicted trajectory due to gravitational interaction with an invisible object (Neptune) [16]. Today we have a variety of different observations supporting the idea of invisible mass, DM, from investigating the motion of galaxies [2], galaxy clusters and their mass [17], fluctuations in the CMB [18] or other findings. All these observations suggest that DM exists and can even impose some limitations on the nature of DM. This and the fact that there is $\sim$ five times more DM than baryonic matter are very intriguing and lead to many theories about the nature of DM. Many different ideas have been developed that introduce different particles as candidates for DM such as sterile neutrinos [19], axions [6] or WIMPs [7], etc., and different methods and experiments have been built to find them.

2.1 Evidence

The existence of DM is proven by its observed gravitational effects on macroscopic objects of different sizes like galaxies, galaxy clusters or even the CMB. Although they are different observations, they all lead to the same conclusion, the existence of DM. Some of the observations are described below.

2.1.1 Rotation Curve

One of the earliest indications for existence of DM, starting with Zwicky in the 1930s, comes from rotational velocity of gravitational bound systems like galaxies or galaxy clusters. Similarly to how planets revolve around the Sun in our Solar System, stars orbit the center of their galaxy. The rotations speed is defined by the balance between the centrifugal force and the gravitational force due to the galaxy's mass, which keeps them on their orbital trajectories. The majority of the galaxy's visible mass is in its center and the rotational velocity of orbiting objects should decrease as follows:

$$v(r) \propto \sqrt{\frac{1}{r}} \tag{2.1}$$

as the distance to the center increases.

However, observations show that the velocity dispersion in galaxies does not follow this expected behavior. This can be seen in Figure 2.1 where the velocities of objects inside the galaxy NGC 6503 are presented as an example. It is evident that the velocity is constant over a wide distance from the center of the galaxy. This can be explained by an invisible mass that pulls on orbiting stars gravitationally and thereby allows a much higher speed.

2.1.2 Galaxy Clusters

Another approach is to measure the mass of a galaxy and compare it with the mass deduced from visible matter. The total mass of the galaxy can be measured by gravitational lensing, which occurs when a massive object warps the surrounding spacetime. This causes light from a source behind it to follow a curved path which allows it to be seen from Earth, even though it would not have reached us otherwise. By studying the distorted images of objects behind the massive object, we can determine the mass of the galaxy causing the bending. This method

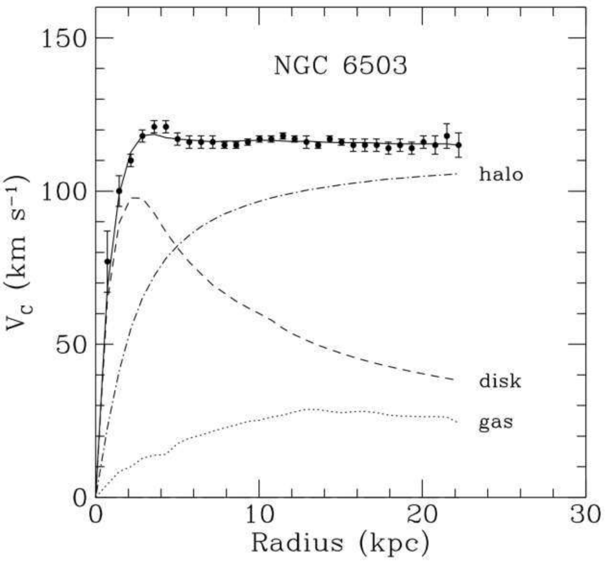

Figure 2.1: Observed rotation curve of objects inside galaxy NGC 6503 with pictured contributions from the gas (dotted), disk (dashed) and DM (dash-dotted) and the combined curve (solid line) [20, 21].

reveals that many galaxies have a significantly greater mass than is inferred from visible matter alone [17].

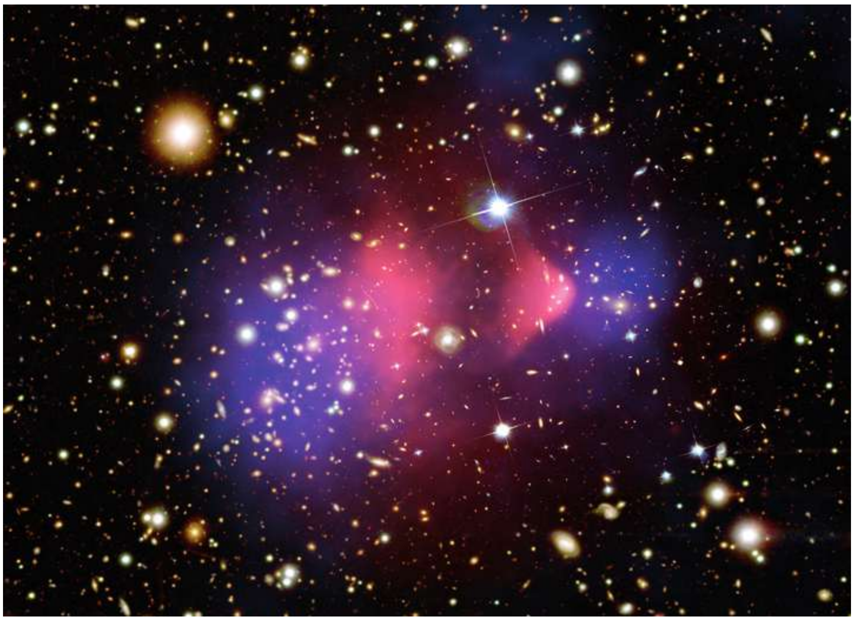

Figure 2.2: The processed image shows the bullet cluster [22], observed by different telescopes. Pink represents hydrogen clouds as seen in X-rays. The galaxies can be seen in orange and white in the optical image. Blue depicts the concentration of mass deduced via gravitational lensing. The picture is taken from [23].

A very prominent example of a cluster studied with gravitational lensing is the Bullet cluster, illustrated in Figure 2.2. These are two galaxy clusters that have traversed each other. During this passage, most of the visible matter, the hydrogen gas shown in pink, interacted with each other and slowed down, whereas the center of mass, shown in blue, seems unaffected [22].

This is a direct observation of DM that cannot be explained by a modification of the gravitational force. The MOND (MOdified Newton Dynamics) theories are an alternative interpretation of the observed phenomena without the need for additional mass [3].

2.1.3 Cosmic Microwave Background

A further clue for DM is provided by the CMB, which represents the radiation footprint from the universe's recombination era shifted to lower energy due to redshift because of the universe expansion [18]. Although it is almost an ideal black body with a temperature of $(2.725\,48 \pm 0.000\,57)\,\mathrm{K}$ [24], minor temperature fluctuations in $\mathcal{O}(10^{-5})$ can be detected. Analyzing a power spectrum from these fluctuations permits one to derive information regarding the composition of the universe, suggesting a baryonic matter density of 4.9 % and roughly five times more DM with 26.8 %. The rest is expected to be dark energy [25, 26].

2.2 Dark Matter Candidates

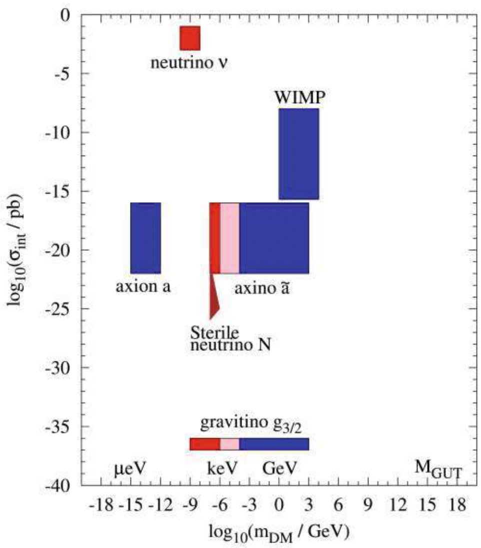

Figure 2.3: Mass dependent cross-sections for different DM candidates. Blue is CDM, red is HDM and pink is WDM. Figure adapted from [7].

The term dark matter is very generic and addresses many different ideas of DM with various different characteristics. However, according to observations, all DM candidates must exhibit some fundamental properties [7]: DM must be electrically neutral and should only interact weakly with Standard Model (SM) particles, or if other interactions occur, they must be minimal enough to be neglected. DM self-interaction should not be excessively strong. DM needs to be stable or at least have an extremely long lifetime.

Even with these shared characteristics, there are numerous different theories and concepts regarding DM candidates, covering different mass ranges and cross sections (see Figure 2.3). DM can be divided into three types Hot Dark Matter (HDM), Warm Dark Matter (WDM), and Cold Dark Matter (CDM) [27]. While HDM is referred to very light ($\lesssim$ few keV), relativistic and free streaming DM, WDM is interacting much more weakly with masses an order of magnitude higher. For CDM free streaming is not important and it can have masses magnitudes higher than HDM and WDM. The most significant candidates for DM, baryonic DM, neutrinos, axions, WIMPs, etc., are presented in [2, 5–7, 19]. In the following, some of them are briefly described.

2.2.1 Baryonic Dark Matter

Over the years, numerous different ideas about DM came to life. To keep an overview, they can be broadly categorized. An initial classification separates non-baryonic from baryonic DM.

Although baryonic DM is largely ruled out by observations of the CMB, theories involving very massive objects persist and continue to be explored. Some well-established candidates for baryonic DM are massive compact halo objects (MACHOs). Examples of these objects include brown dwarfs, remnants of stellar black holes, or neutron stars. All of these MACHOs can be detected by using microlensing. However, studies indicate that MACHOs can only account for up to 20 % of DM [5].

2.2.2 Neutrino

Neutrinos are the only particle from the SM that exhibit all previously described properties. They have mass, do not have charge, and interact via weak force. In addition, they do possess a long lifetime. However, they can be ruled out as the primary constituent to DM because they are relativistic and would contribute to HDM; however, simulations show that HDM does not explain the structure formation of the universe [28].

In addition to standard neutrinos, a sterile neutrino is proposed. Unlike neutrinos, it would be right-handed and would solely interact with neutrons. If existing, it could address issues such as neutrino mixing, the baryon asymmetrie in the universe, or it can contribute to DM [4].

2.2.3 Axion

Axions and axion-like particles expand the SM and are often introduced by spontaneous breaking of one or more global symmetries at high energies. They offer solutions to the shortcomings of the SM such as the CP-violation and can account for cosmological observations like the baryon asymmetry of the universe. Typical models assume particles with masses below 1 eV [6]. Due to their low mass, it would be compelling to assume that axions are HDM similar to neutrions; however, a mechanism closely connected to the Peccei-Quinn symmetry was found that could populate the universe with a substantial amount of CDM axions [29, 30]. Despite this, until now no evidence of an axion or axion-like particle was found.

2.2.4 Weakly Interacting Massive Particles

A very large class of DM candidates are WIMPs which encompass a variety of different particles and theories related to DM outside the SM. It is assumed that WIMPs decoupled from thermal equilibrium after the early universe cooled down, leading to particles that are not relativistic and therefore contribute to CDM. They are predicted to be in the mass range of $\mathcal{O}(10\,\text{GeV})$, with calculated cross-sections comparable to that of the weak force. This relatively large cross section, compared to many other DM candidates like axions or sterile neutrinos (see Figure 2.3), makes them a good candidate for direct detection experiments [7].

2.3 Detection Methods

For a potential detection of DM, it is necessary to consider one of interaction channels between DM and SM particles. This would allow to observe other DM/SM particle interactions in addition to gravitational effects on big scales. Three different approaches are used to search for DM, each using a unique form of DM interaction with SM particles (see Figure 2.4): Indirect detection looks for SM remnants resulting from DM interactions, such as the annihilation of DM into SM particles. A collider-based method attempts to generate DM by colliding SM particles, whereas direct detection experiments seek DM by observing scattering off SM particles. Different experiments are developed using different detection methods. Those are briefly discussed below, together with some experiments which are given as examples.

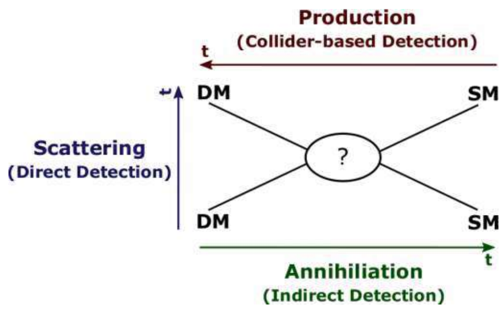

Figure 2.4: Three different detection channels are used for dark matter research, each having different ad- and disadvantages. Figure taken from [31].

2.3.1 Creation of Dark Matter in Particle Colliders

This concept involves generating particles and probing whether some are unfamiliar. For particle generation, energy is an essential part, which can be provided by particle colliders. This approach is followed at CERN using the Large Hadron Collider. However, due to the weak interaction of DM with SM particles, it is expected that DM will not generate a visible signal itself, so the search focuses on other observable effects, such as the use of transverse momentum conservation. Because the net momentum in the plane perpendicular to the interacting beams must be zero, a deviation can be seen quite easily. Therefore, missing momentum is the main signal for the creation of DM in collider experiments [32].

2.3.2 Indirect Detection

Indirect DM detection experiments search for a SM particle signal arising from an annihilation of DM resulting in SM particles. With this type of experiment, the lifetime and the annihilation cross section of DM is investigated. Various telescopes and detectors, as well as SM particles, can be used for the search. For example, IceCube [33], a neutrino telescope located at the south pole, measures neutrinos with a $\sim 1\,\mathrm{km}^3$ detector, while some neutrinos possibly result from DM annihilation [34]. Another experiment is the Fermi Gamma-ray Space Telescope [35], a satellite that searches for high-energy sources and DM photon signals from DM annihilation [36].

2.3.3 Direct Detection

Direct detection experiments aim to identify DM interactions with terrestrial detectors. For this research, it is assumed that there is a local non vanishing DM density and it is often expected that DM scatters elastically off nuclei. However, given the uncertain characteristics of DM, it is crucial to explore a wide range of DM masses. Therefore, different types of detectors are needed, using different materials in different physical states (solid, liquid, and gaseous). Furthermore, three different channels are available to measure the signals from particle interactions within the detector. Each channel varies in its sensitivity to energy and the amount of energy collected per particle interaction (see Table 2.1). In more recent experiments, often a two-channel approach is utilized. This enables particle id discrimination.

Table 2.1: The table represents the different channels, the minimum energy required to generate a single excitation or particle and the fraction of the total deposited energy that is available in each respective channel [37].

Channel	least Energy	collectable energy
Phonons	10 meV/phonon	100 %
Ionization	10 eV/electron	20 %
Scintillation	1 keV/gamma	few %

A big variety of experiments contribute to direct detection DM research. Liquid noble gas experiments,such as Xenon100 [38] or Xenon1T [39] utilize scintillation and ionization to explore potential DM within higher mass ranges. Other known liquid noble gas experiments are DarkSide [40], LUX [41] or Panda-X [42].

For DM masses $\leq 1\,\mathrm{GeV}/c^2$, solid state and gas detectors are ideal due to their low energy thresholds. The NEWS-G experiment [43] uses gas to search for light DM, while CRESST [44] is a representative example of a two-channel solid state detector experiment using both scintillation and phonon channels. This dual channel approach enables high-precision energy deposition measurements of DM recoil. However, other solid-state experiments are CDMSlite [45], DAMIC [46] or EDELWEISS [47].

I have to point out that except for DAMA [48], who claim to see an annual modulated signal expected by DM due to the relative motion of the earth around the Sun [49], until now no other experiment has found any indication for DM through one of the mentioned detection channels. Measurements by DAMA need to be investigated further. This will be done in the near future by COSINUS [50] which has a great advantage among other experiments testing DAMA results due to the detection technique adopted from CRESST experiment.

3 | The CRESST Experiment

For years, the CRESST [51] experiment has remained at the forefront of DM research. It is situated in Italy at the LNGS, 1400 m beneath the Gran Sasso massif, which corresponds to 3600 m of water equivalent [52]. Using cryogenic ($\sim 15\,\mathrm{mK}$) detectors with different scintillating materials as targets, it probes WIMPs with masses in the sub-GeV range ($\lesssim 1\,\mathrm{GeV}$) and an expected recoil energy in the sub-keV regime. With its current experimental setup the ROI for DM covers energies as low as 10 eV [53]. Ongoing experimental operations and data collection allow the experiment to further improve the cross section / mass limits of DM and gradually approach the neutrino fog [54].

This chapter starts with a description of CRESSTs general experimental setup (section 3.1) followed by an explanation of the employed detection principle (section 3.2) and a presentation of two specific detectors in particular: TUM40 and TUM93A (section 3.3). In addition, different surface profiles of target crystals and parameters are presented (section 3.4). Finally, a brief overview of different sources of electromagnetic background measured by the CRESST experiment is provided (section 3.5).

3.1 Experimental Setup

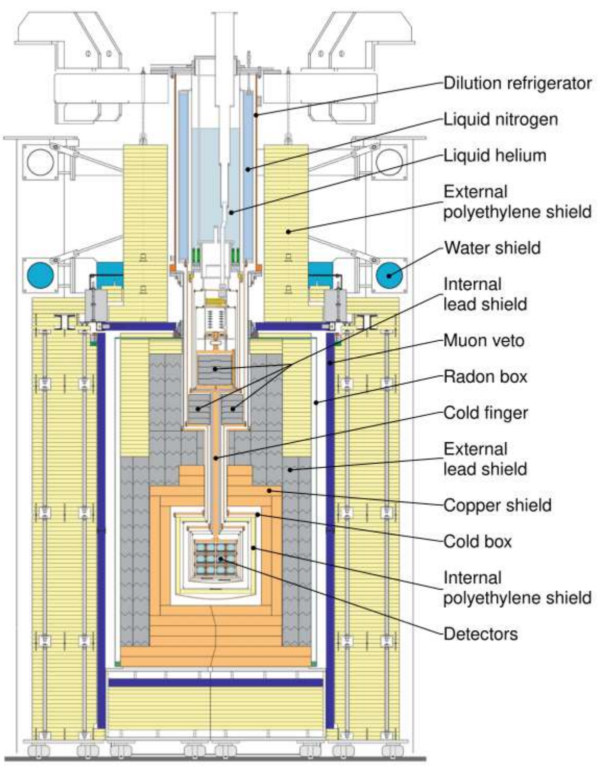

Figure 3.1: Technical drawing of the CRESST setup.

The Gran Sasso massif shields the experimental site against cosmic radiation and thereby decreases the flux of high-energetic atmospheric muons by several orders of magnitude.

A muon veto with a geometrical coverage of 98.7 % tags residual muons that successfully crossed the Grand Sasso mountains. Achieving 100 % coverage is precluded due to the space requirements of the cryostat.

Multiple layers of different materials protect the experimental volume from environmental neutrons and ambient γ-rays. The outer layer, composed of polyethylene, effectively attenuates neutrons. An intermediary layer of lead and copper mitigates the incidence of γ-rays, while an inner polyethylene layer provides additional shielding against neutrons generated within the lead shielding.

The cold finger of a ^{3}He/^{4}He-dilution refrigerator reaches through the multiple layers of protection, cooling the cold box of the setup to $\sim 15\,\mathrm{mK}$. The core of the experimental setup is the carousel that accommodates the detector modules. For a more detailed setup, see the technical drawing of the experiment (Figure 3.1) and [11].

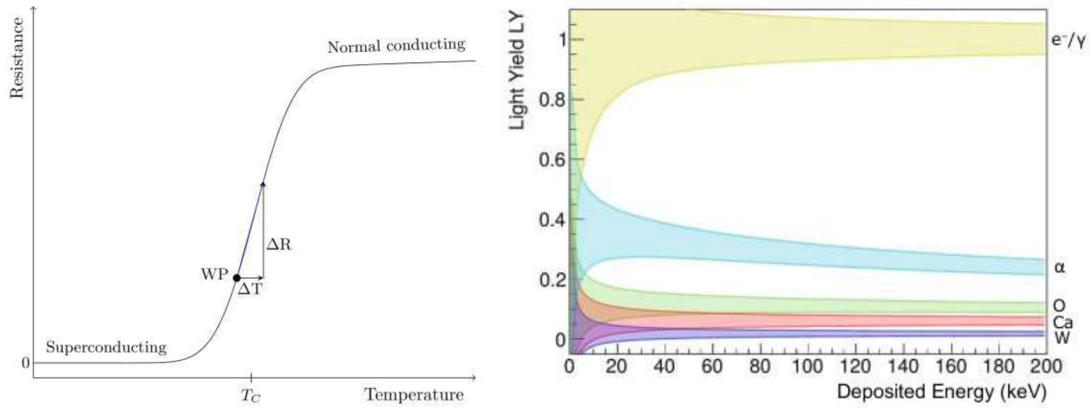

Figure 3.2: (Left) Scheme of function of resistance R dependant on temperature T of a TES. The function has a steep increase in resistance around the critical temperature T_c. Figure adapted from [55]. (Right) LY as a function of energy for different interaction partners in the target crystal [31].

3.2 Detection principle

CRESST endeavors to measure the elastic recoils of DM within cryogenic crystals maintained at $\sim 15\,\mathrm{mK}$. The recoil induced by DM within the target imparts energy, thereby generating phonons and inducing a slight increase in temperature. The resulting temperature variation in the target is measured using a Transition Edge Sensor (TES) [56].

A TES is a thin film of tungsten, which serves as a superconductive thermometer, enabling highly precise measurements of the change in temperature. It is operated at the transition between its superconducting and normal conducting phases (see Figure 3.2, left). This results in a large change in electrical resistance in response to a small change in temperature. The change in electrical resistance is then read out using Superconducting QUantum Interference Device (SQUID) amplifiers. For a detailed discussion on the measurement setup of TES, see [55]. All detectors discussed in the following are equipped with a TES.

The use of scintillating target materials in the experiment enables to utilize a two-channel approach to simultaneously measure both: phonons and scintillation light. This strategy allows for discrimination between nuclear recoil and electromagnetic interaction events within the target using the light yield (LY) (see Figure 3.2, right). The LY is defined as the ratio of the energy measured via photons and phonons, normalized relative to the ratio of e^-/γ events[1]. This ratio varies according to the nature of the interacting particle due to different quenching factors [58]. Consequently, under the assumption that DM interacts with the target solely through recoil, all measured values with a LY in the e-/γ or α band can be excluded.

3.3 Detectors

Each detector module is equipped with two separate detector crystals: one dedicated to measure phonons, called phonon detector or target, and one to measure the scintillation light, referred to as light detector.

During the course of development, different detector modules have been designed with different geometrical configurations and target sizes, as well as different target materials such as $LiAlO_2$ or Si [9, 10], however, the working principle is the same for all modules. This thesis concentrates on two specific modules, TUM40 from CRESST-II and TUM93A from CRESST-III, the latest version used now. Both detector modules are discussed in the following.

[1] To be exact, the ratio of e^- to γ events at an energy of 122 keV is set to 1 [57].

3.3.1 TUM40

The TUM40 detector module (see Figure 3.3) employs a $CaWO_4$ crystal with size 32 x 32 x 40 mm^3 and a mass of $\approx$ 240 g, as its target. The crystal was grown in the crystal laboratory of Technische Universität München (TUM) using a Czochralski crystal production facility [57]. The home production of $CaWO^4$ crystals gives CRESST the ability to improve the level of intrinsic radiopurity of the target material used as detectors. Due to this, the total internal alpha background was reduced to $\sim$ 3.080 mBq/kg [59, 60] in comparison with commercially produced crystals with and alpha background between $\sim 15 - 35$ mBq/kg [61]. The crystal is intentionally roughened to reduce positional dependency for light measurements and to increase its light output [62]. The TES is evaporated on an extra carrier crystal and then glued to the polished side. Employing a carrier crystal avoids exposure of the target crystal to the high temperatures used for evaporation, which would reduce the scintillation light output [57, 63].

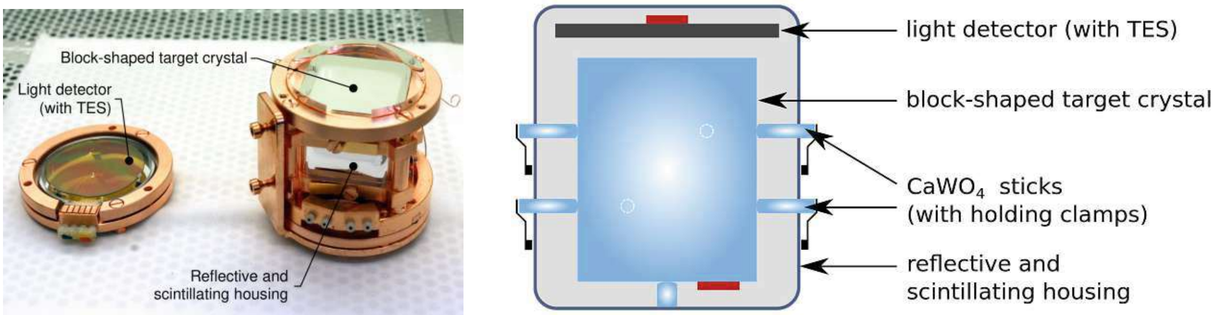

Figure 3.3: Picture (left) of the TUM40 detector crystal used in CRESST-III phase 2. The target is a $CaWO_4$ crystal with a size and mass of 32 x 32 x 40 mm^3 and $\approx$ 240 g. The TES is evaporated on a carrier crystal of $CaWO_4$ that is then glued onto the polished side of the TUM40 crystal. The rest of the crystals surface is roughened except for small patches where the $CaWO_4$ holding sticks are in contact with the crystal, there it is polished. The schematic (right) of the TUM40 module shows the arrangement of the phonon and light detector as well as the holding sticks and the TES (in red). Schematic taken from [60].

The housing of the detector module is made out of copper; inside, the target is held by eight $CaWO_4$ sticks which themselves are fixed by bronze clamps that press from outside the module against them. The inside of the module is lined with a reflective foil. This design ensures that only scintillating materials are in direct line of sight to the target, which is important for particle discrimination and, in consequence, for suppressing the electromagnetic background.

3.3.2 TUM93A

TUM93A is one of CRESSTs radiopurest crystals ever grown at TUM and whole world, currently used in the ongoing data-taking campaign. Analysis shows that the total internal alpha background is reduced to $\sim$ 516 µBq/kg [64] in comparison with TUM40 which had $\sim$ 3.080 mBq/kg [59, 60].

For the TUM93A crystal, the CRESST-III standard detector module is used [51]. The $CaWO_4$ target crystal measures approximately 20x20x10 mm^3 and a total mass of $\approx$ 24 g. The target crystal is held in place by $CaWO_4$ sticks that have scintillation properties similar to those of the target crystal. Adjacent to the target is a SOS disk that functions as a light detector. The target, one of the sticks and the light detector are each equipped with a TES. The inside of the module housing is covered with a reflective foil, to maximize the collection of scintillation light within the SOS detector, and to ensure that no non-scintillating detector component is in direct line of sight to the target. This is important for an effective particle discrimination using the LY.

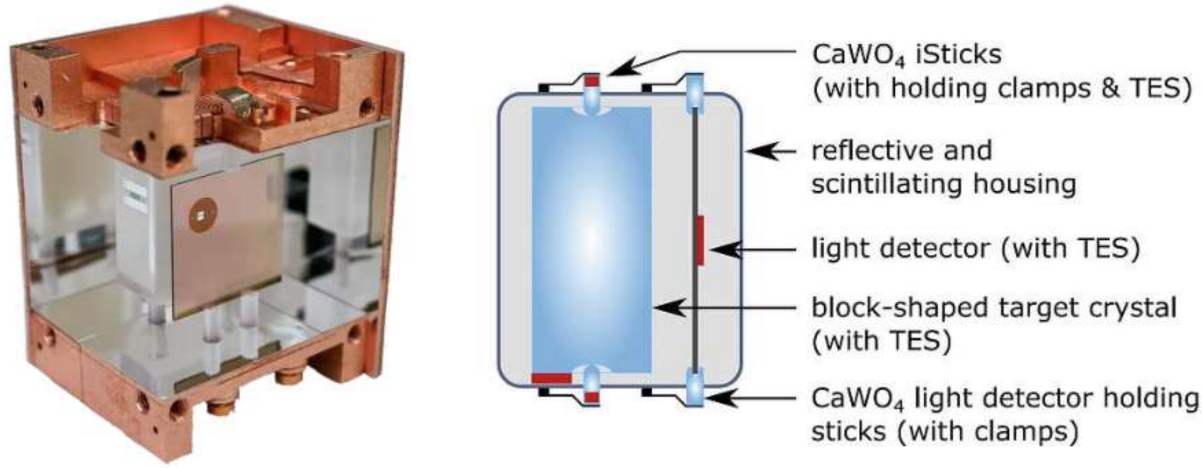

Figure 3.4: Picture of an (left) open detector module of the CRESST-III setup with a ≈ 24 g $CaWO_4$ target crystal and a silicon-on-sapphire (SOS) light detector, both equipped with a TES and (right) a schematic of the same. The TES are colored in red. The scheme is taken from [44].

3.4 Surface Measurement

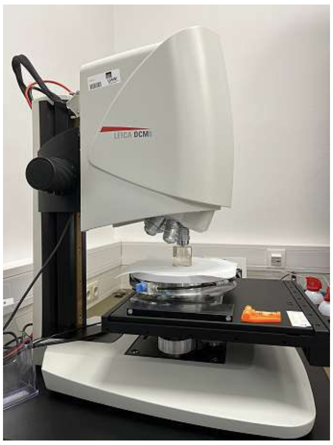

Figure 3.5: Measurements of surface profiles were done with a LEICA DCM8 microscope [65].

The surface of the target crystals used by CRESST can have different structures, depending on their treatment. They may be polished or diffused intentionally. Diffusing the surface of a target crystal serves to enhance the light output and to mitigate potential positional dependencies when measuring the scintillation light [57, 62]. The preparation of the surfaces was done manually at TUM, always by the same person.

The surface structure of eight target crystals was examined with a LEICA DCM8 microscope [65]. Parameters such as the arithmetical mean height, maximum height, kurtosis, skewness and others were evaluated. Figure 3.6 illustrates that the diffused surface of a $CaWO_4$ crystal exhibits structures within the µm scale, whereas a polished surface has single irregularities but can otherwise be regarded as planar relative to this dimensional scale.

Although no measurement is available for TUM40 or TUM93A both target crystals are diffused and it can be expected that the roughening procedure, which was carried out by the same person, creates a diffused surface similar to that seen in Figure 3.6. This is supported by the observation that the investigated surfaces from different crystals have similar surface profiles.

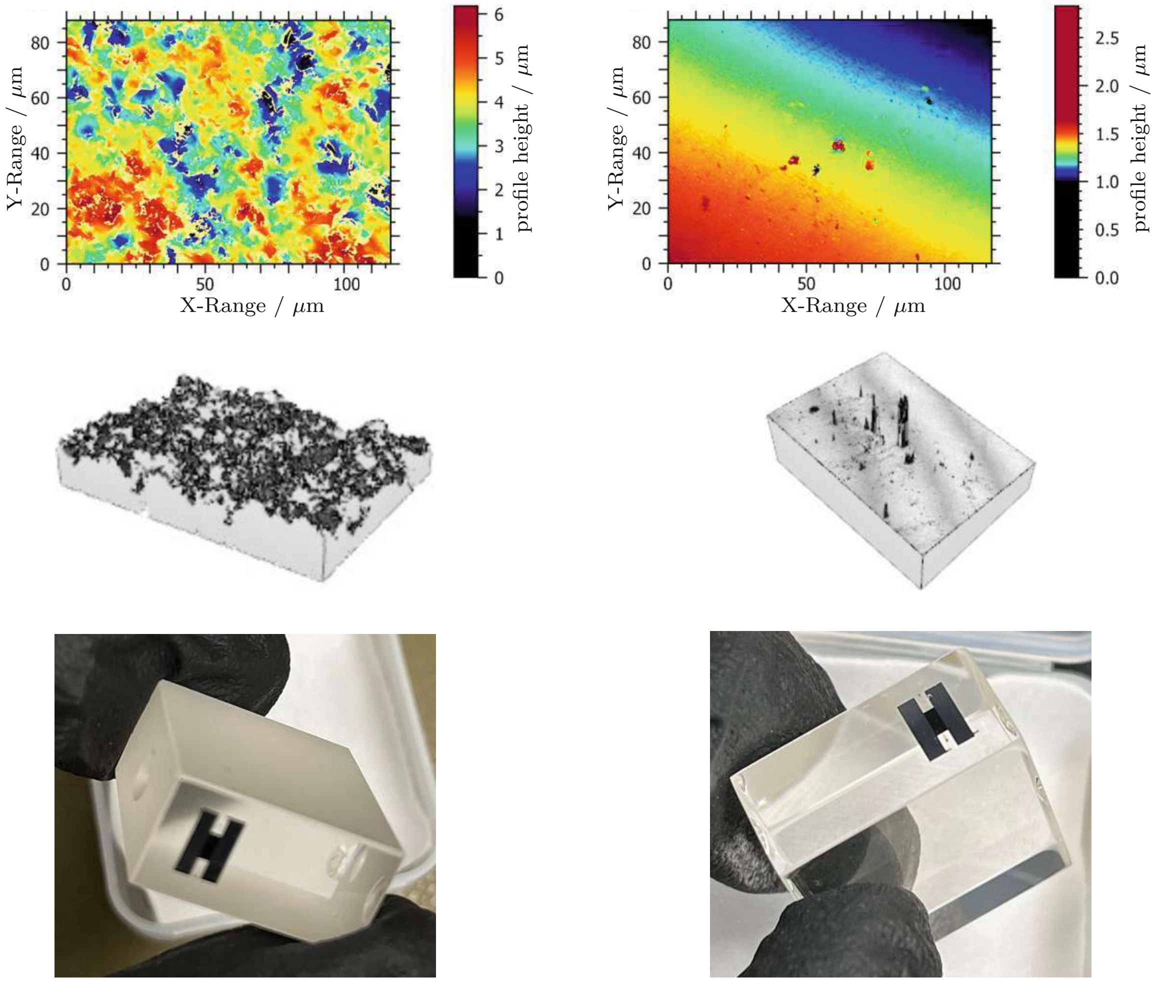

Figure 3.6: Surface roughness profiles of a diffused (left) and polished (right) $CaWO_4$ crystal, TUM73 and TUM84 respectively. The surfaces were examined by V. Mokina, using a LEICA DCM8 microscope.

3.5 Background

Despite multiple layers of shielding (see section 3.1) some particles can reach the inner experimental volume or are already present beforehand due to detector contamination with radioactive isotopes [59, 64] and must be taken into account when investigating the electromagnetic background measured by CRESST. For that, various sources like muons, ambient γ-rays, cosmic activation and internal contaminants of the target crystal are investigated utilizing simulations [66].

3.5.1 Muons

Due to the Gran Sasso mountains the high energetic muon flux at LNGS is already reduced by six orders of magnitude compared to the flux at sea level [67]. However, the residual flux at the experimental site remains at $1/(\mathrm{h\,m^2})$ and can either directly interact with the detector or produce secondaries by interacting with the surrounding material such as rock or material from the experimental setup. These muons are tagged on an event basis by the muon veto of the experimental setup with a geometrical coverage of 98.7 % and an efficiency exceeding 98 % [68].

3.5.2 Cosmogenic Activation

Due to cosmic rays radioactive impurities present in the detector and other components material or the detector material itself can get activated while the detector is not underground [69]. Multiple spectral lines can be found caused by the decay of cosmogenically activated nuclides [51, 70]. Within $CaWO_4$, tungsten is particularly susceptible to the activation. Specifiaclly, ^{182}W can be activated via proton capture which then decays to ^{179}Ta and ^{179}Hf through electron capture and ultimately emits X-rays. Or ^{183}W may be activated, again via proton capture, leading to a series of decay steps that result in the emission of γ- and X-rays.

Another radioactive nuclide that can be generated is ^{3}H (see Figure 3.7). Unfortunately, in comparison to the other activation's, ^{3}H is challenging to be observed experimentally. This difficulty arises because ^{3}H emits a β-spectrum that is obscured by other background components. Furthermore, alternative reaction paths are feasible to create ^{3}H, in addition to cosmic activation of ^{183}W. In [71] an estimate of ^{3}H can be found.

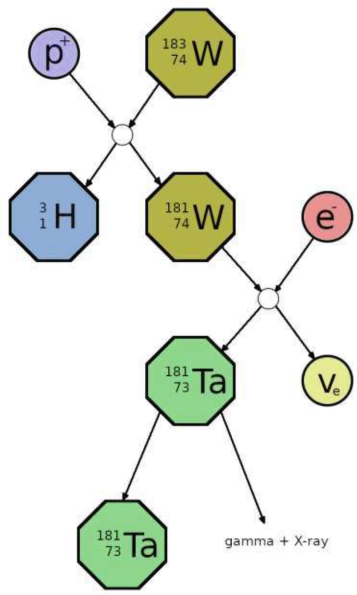

Figure 3.7: ^{183}W decay chain started by cosmic activation.

3.5.3 Ambient Gamma-Radiation

A third type of background is ambient γ-rays originating from the concrete and rock at LNGS. These rays are the result of radioactive decay chains starting from ^{232}Th, ^{234}U, ^{238}U or single nuclides such as ^{40}K. The γ-flux at LNGS near the experimental site was measured to be $\sim 0.28/(\mathrm{cm}^2\,\mathrm{s})$ for energies below 3 MeV [72]. To mitigate these radiations, the experimental volume is protected by multiple layers of different materials: a) an external lead shielding with a thickness of 20 cm. Given the presence of the naturally occurring isotope ^{210}Pb with a half-life of ~ 22.3 yrs, lead itself is inherently unstable and produces γ-rays and alphas by starting a short decay chain (see Figure 3.8). To address this, CRESST lead with reduced ^{210}Pb contamination (35 Bq/kg) was produced [73]. b) A layer of highly radiopure copper is placed between the experimental volume and the lead to protect against the residual γ-rays. Copper is advantageous as it can be produced with very low intrinsic radioactivity (< 1 mBq/kg). c) The protective layers of lead and copper have a hole used to guide the cold finger through the shielding (see Figure 3.1). This is covered by an archaeological lead shield (3.6 Bq/kg) positioned above the cold finger [73].

3.5.4 Internal Contamination

Another source of background radiation may come from contaminants within the $CaWO_4$ crystal itself, such as nuclides from natural decay chains. Possible decay chains are started by the α-emitting nuclides ^{238}U, ^{235}U or ^{232}Th. Most of the α-emission results in energy deposition within the MeV range and are easy to identify; however, subsequent decays involve the emission of β- and γ-rays, which can contribute to the deposited energy within the ROI of the experiment.

To address this issue, very pure $CaWO_4$ crystals are produced by first applying chemical purification to the raw materials $CaCO_3$ and WO_3 and to the synthesized $CaWO_4$ powder. The crystals are then grown in a Czochralski furnace [55]. The home production of crystals allows for control of each step of crystal production and ensures no additional uncontrolled contamination. This facilitates a reduction of the low energetic background attributed to decaying contaminants by a factor of 2 to 10 in the ROI compared to commercial crystals [66]. However, the remaining background induced by contaminations needs to be understood.

In addition to the bulk contamination, the crystal surface can be contaminated with ^{210}Pb originating from the ^{222}Rn decay-chain (see Figure 3.8). Radon, a naturally occurring gas [75],

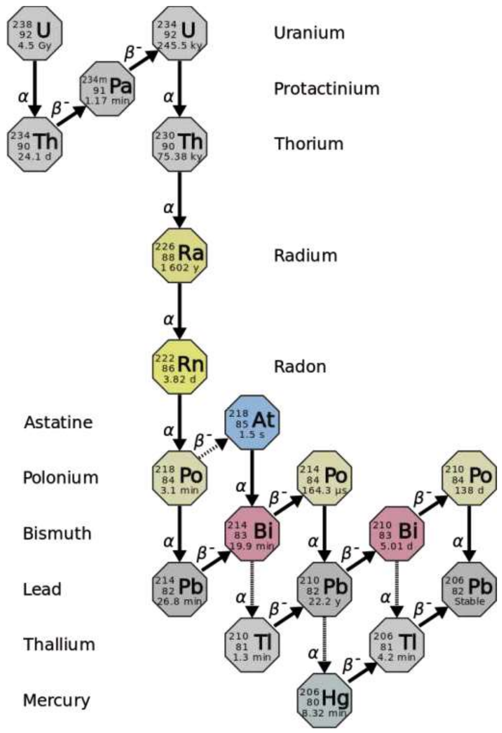

ht

Figure 3.8: Decay-chain of ^{238}U with its sub-chain ^{222}Rn [74].

can emanate from the soil and, upon decay, can contaminate the surface of the crystal with its decay products such as ^{210}Pb. ^{210}Pb in turn has the possibility to accumulate on the surface due to its half-life of $\sim 22.3\,$yrs.

4 Simulation Tools

To investigate the electromagnetic background, a background model was developed using simulations [11] and different simulation tools developed and used by the CRESST collaboration. In the following the tools necessary to simulate various sources of electromagnetic background and their interaction with the experimental setup (ImpCRESST section 4.1, Rough Surface Module (RSM) section 4.4), to apply a detector resolution to the simulated energy deposition spectra (CresstDS section 4.2), and to fit the data to real measurements (Bliss section 4.3) are introduced. As default Geant4 and, therefore, ImpCRESST neglect the explicit simulation of a surface roughness, the key element of this thesis is the development and implementation of RSM. It allows to conduct surface contamination simulations while applying an actual rough surface. The different developed parts, such as the roughness generator, the portal, the particle generator, and the shift, are discussed in more detail below.

4.1 ImpCRESST

ImpCRESST [11] is a Geant4/Root-based [76–79] simulation tool developed and used by the CRESST collaboration and designed for rare-event search experiments. It is used to model the experimental setup and simulate different sources contributing to the measured energy deposition spectrum inside the target crystal. It allows users to build complex geometries, either by tediously defining the different geometries using the classes provided by Geant4, written in C++ or by importing them from external files (simplified engineering files). For importing geometries from external files the interface CADMesh [80] is used. Moreover, the simulation framework allows the generation of primary particles anywhere within the simulated volume, allowing the user to model different sources, such as other experimental components with radioactive impurities.

Additionally, users can choose from a variety of different physics lists, which have different physics models for different simulation purposes (e.g. simulating particle interaction with tissue or very low energy electromagnetic physics interactions).

The resultant data, which includes information such as interacting particles, deposited energy within specified volumes, spatial coordinates, temporal information and more are stored in root files utilizing a developed data structure for ImpCRESST.

The simulation can be further controlled with macro files. These text files enable users to set and control different sources, select the physics list, adjust various parameters such as detector sizes, or adjust the level of details in simulation. For more information on simulations using ImpCRESST see [11].

4.2 CresstDS

ImpCRESST simulates a perfect detector, it even registers all single energy depositions from one event; however, to obtain a more realistic energy deposition spectrum, comparable to real measurements taken by CRESST, the detector response, especially a finite time and energy resolution, can be emulated with CresstDS. This splitting between simulating events and emulating the detector response enables the user to apply different detector response models without the need to redo the computationally expensive ImpCRESST simulations.

4.2.1 Applying the Detectors Time Resolution on Simulated Data

The finite time resolution of a detector is simulated by summing up all the deposited energy in a time interval Δt. The interval is started by a hit of the detector. A new hit after the time interval will immediately start a new time interval. The current interval length is set to 2 ms, however, it has to be emphasized that this value was found empirically and that the current simulation is omitting pileup events. However, a new study suggests that they can have some effect on the measured background spectrum [81] and should be considered in the future.

4.2.2 Applying the Detectors Energy Resolution on Simulated Data

The simulation of energy resolution is done by calculating the observable energy corresponding to the deposited energy of an event. This involves stochastic sampling of a Gaussian centered on the deposited energy. The Gaussian function is acquired through the fitting of cubic polynomial functions to the detector resolution, utilizing reference data sets. For details, see [11].

4.3 Bliss

Bliss [12] is a BAT-based [82] high-dimensional Bayesian likelihood normalization tool. It is used to fit multiple different energy deposition spectra for different sources to the data measured by CRESST. For fitting, no assumption of secular or partial secular equilibrium is needed; however, can still be defined. This enables the user to incorporate peakless spectra (^{3}H) or spectra with similar peaks but differences in their continuous part (^{40}K in different components of the setup). For a detailed description of the tool and its capabilities, see [12].

4.4 Surface Module

The RSM is a Geant4-based C++ library for surface roughness simulations. Its development and implementation are key elements of this thesis. With it, it is possible to implement an "actual" rough surface of any size for simulation with Geant4 and contaminate the volume in the vicinity of the surface using any self-defined depth distribution for placement. By implementing different controllable parameters, it is possible to simulate surfaces of various structures from very roughened to polished. The library is split in three parts: a) the "Roughness" for generating a Geant4 geometry representing a patch of rough surface, b) the "Portal" to extend the patch of rough surface to cover any size of area, c) the "Particle Generator" to randomly sample uniformly distributed points on the rough surface and to shift starting points below the surface following any self-defined depth distribution.

4.4.1 Roughness

A rough surface patch is represented by a G4MultiUnion that contains spikes covering a two-dimensional area, all pointing in the same direction (see Figure 4.2). A patch of up to $\sim$ 1000 x 1000 spikes can be generated, which can contain different spike forms (see Figure 4.1) and spike heights. The height, width and number of spikes can be controlled and enables the user to generate surfaces of different types from very rough to polished. These implemented geometry represent an "actual" rough surface in simulation.

The number of spikes and different forms is limited by the Random-Access Memory (RAM) available on the computer system used. This limitation arises due to the memory-intensive voxelization process of the G4MultiUnion. Voxelization is an optimization method implemented in Geant4, which involves generating a grid of boxes (voxel) and assigning individual volumes of the G4MultiUnion to them. However, assigning spikes with different heights in the patch

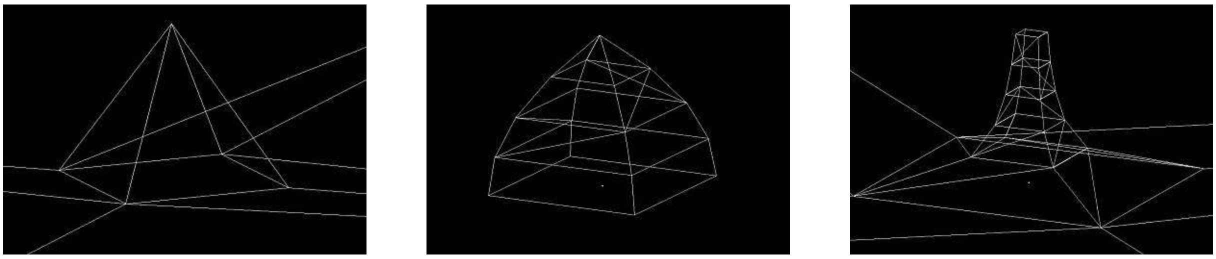

(a) **(b)** **(c)**

Figure 4.1: Visualization of different shape implementations for spikes, which can be of any size that is allowed in Geant4.: (a) simplest form of a spike, basis is a Geant4 tetrahedron. (b) multiple layers of Geant4 tetrahedrons form the spike, the outer surface approximates a squared function. (c) multiple layers of Geant4 tetrahedrons form the spike, the outer surface approximates $1/x$.

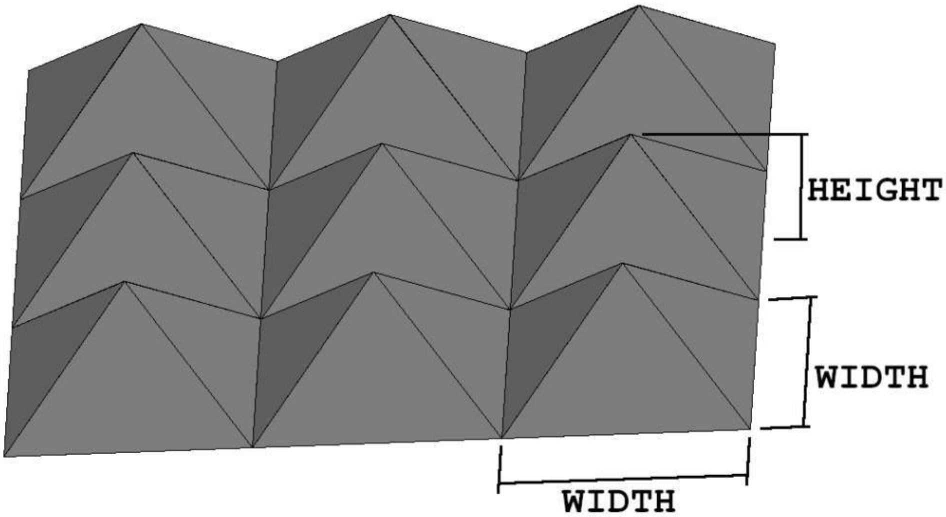

Figure 4.2: Visualization of 3x3 spikes placed at the surface of a target volume to simulate a patch of rough surface. The generated spikes can be of any size allowed in Geant4. The size is controlled via setting a width and height for the spiked.

significantly increases memory consumption, scaling with $\mathcal{O}(n^3)$. This excessive memory requirement is attributed to the voxelization algorithm, which first creates all the boxes (voxels) by defining boundaries whenever a sub-volume (a spike, or part of a spike) of the G4MultiUnion starts or ends in one single spatial direction. Subsequently, the algorithm reduces the number of boundaries in one dimension to ensure it does not exceed a predefined limit of 100,000.

However, for multiple spatial dimensions having a large number of boundaries, the maximal number of 10^5 is set to high as this could result in $\sim 10^{15}$ boxes. Unfortunately, it is not possible to manually change this number when using a G4MultiUnion. In addition, inheriting from the C++ voxelization class and adding the possibility to change the number is not possible due to the private settings of the class. The C++ voxelization class was adapted to overcome this limitation. With this "new" voxelization class it is now possible to generate more complicated surface structures;

Using the raw Roughness class needs tedious work due to many parameters to control and the external voxelization. To overcome this, a helper class was prepared. It allows for a simpler and more clean control of the roughness generation and has multiple secure checks included (e.g. sum of spike sizes are equal to basis size). One helper object per roughness patch must be used. Each instance of this class can be controlled with macro-commands (see Figure 4.3).

```
/Surface/RoughnessHelper/<HelperName>/setVerbose <0-5>

/Surface/RoughnessHelper/<HelperName>/setBasisDx <doubleAndUnit>
/Surface/RoughnessHelper/<HelperName>/setBasisDy <doubleAndUnit>
/Surface/RoughnessHelper/<HelperName>/setBasisDz <doubleAndUnit>

/Surface/RoughnessHelper/<HelperName>/setSpikeDx <doubleAndUnit>
/Surface/RoughnessHelper/<HelperName>/setSpikeDy <doubleAndUnit>
/Surface/RoughnessHelper/<HelperName>/setSpikeMeanHeight <doubleAndUnit>
/Surface/RoughnessHelper/<HelperName>/setSpikeDevHeight <doubleAndUnit>
/Surface/RoughnessHelper/<HelperName>/setSpikeform <Standard, Uniform, Bump, Peak>

/Surface/RoughnessHelper/<HelperName>/setSpikesNx <int>
/Surface/RoughnessHelper/<HelperName>/setSpikesNy <int>

/Surface/RoughnessHelper/<HelperName>/setMaterial <material>

/Surface/RoughnessHelper/<HelperName>/setBoundaryNx <int>
/Surface/RoughnessHelper/<HelperName>/setBoundaryNy <int>
/Surface/RoughnessHelper/<HelperName>/setBoundaryNz <int>
```

Figure 4.3: Macro commands of helper class for surface roughness generation controlling different surface parameters. Arguments are marked with '<...>' including the data type expected or including a hint for the expected type of argument. In one simulation multiple helpers for different roughness patches can be used. To account for this, each helper must be named by the user. This name must then be used for <HelperName> to apply the command to the correct helper.

4.4.2 Portal

Although the simulation of a patch of rough surface was optimized, simulating a rough surface with an area in the range of cm^2 and above is not feasible due to memory usage. However, this is important to simulate a realistic surface of the detector crystals used by CRESST. TUM40 has a surface area of $\sim 71.68\,\mathrm{cm}^2$ while TUM93A has an area of $\sim 16\,\mathrm{cm}^2$. This problem is addressed by the implementation of a portal, which allows the reuse of volumes without the need to replace them as actual volumes again and, in the following, thereby reduces the memory intensity of simulations. The module is used by creating a portal and one or multiple sub-worlds of same size which are reused. The portal covers the volume that is represented by the sub-worlds and thereby acts as a placeholder. A sub-world is made of two volumes: a) the trigger, which when entered by a particle during simulation activates a transportation process, and b) the simulation volume which is placed inside the trigger and represents the actual volume that should be reused multiple times. Inside this simulation volume, anything can be placed. A sub-world should never be entered from the outside, just by a transportation process activated by the portal. Therefore, it is important to place it at a location in the simulation such that it cannot be entered from the outside, otherwise it comes to undefined behavior.

The portals size in each dimension is a multiple of the size of the simulation volumes. This permits the partitioning of the portal into a grid, where each cell of the grid corresponds to a single simulation volume of a sub-world. A surjective map from this grid to the sub-worlds establishes a connection between the portal and the sub-worlds, different cells of the grid can link to the same sub-world and thereby permits reutilization of sub-worlds. Concurrently, the map tracks the position of particles of simulated events through the grid by storing and updating grid coordinates. This permits simulation of the movement of a particle inside the portal volume, while the actual simulation happens inside the inner volume of the sub-worlds.

If a particle enters the portal volume from the outside, the corresponding grid coordinate is calculated and the particle is placed at the correct position withing the associated sub-world. Each time the particle leaves a sub-words inner volume it enters the trigger which activates a transportation in between the sub-worlds or sub-world and portal. Depending on the direction

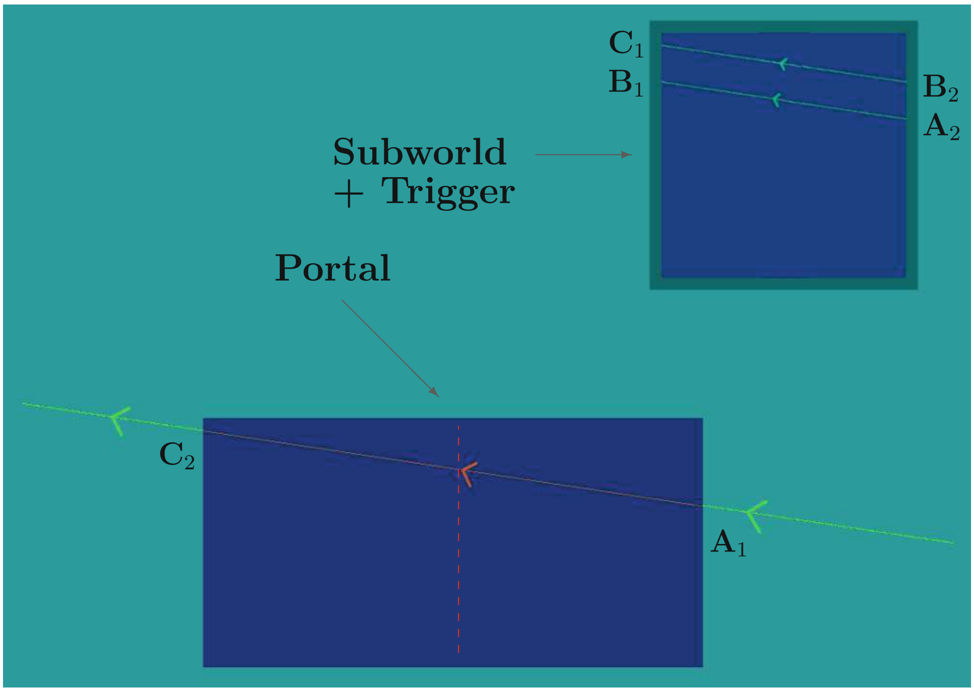

Figure 4.4: 2D sketch of the function of the implemented Portal representing two subworlds. The green dotted line is the trajectory of the particles entering the portal and the subworld on the right side and leaving them on the left. The orange dotted line is the imagined trajectory of the particle crossing the portal. The red dashed line divides the portal into two subworlds.
The simulated particle undergoes the following steps: A) it enters the portal on the right side at A_1 and is ported to point A_2 of the subworld without a change in momentum. B) after crossing the subworld it leaves the volume at B_1 and enters the trigger. This activates the periodic teleportation and the particle is set to point B_2 without a change in momentum. C) after crossing the subworld for the second time it leaves the subworld's volume at C_1 and enters the trigger again. The particle is teleported to C_2 where it leaves the portal, without a change in momentum. The dimension of the subworlds and the portal can be of any size allowed by Geant4. The trigger volume ensures, a correct activation of particle portation.

the particle exits the volume, the grid position is updated and the particle is set to the calculated location in the corresponding sub-world. Should the next grid coordinate fall beyound the bound of the current grid, the particle is relocated to the appropriate position on the surface of the portal volume.

By employing the portal mechanism, a rough surface patch within a sub-world facilitates the simulation of arbitrarily large rough surfaces without augmenting memory consumption. Furthermore, heterogeneous rough surface patches may be amalgamated through the utilization of multiple sub-worlds. Subsequently, specific surface configurations can be engineered by manually delineating the mapping between the portal and the sub-worlds. In the absence of manual definition, this mapping may be synthesized randomly.

By employing the portal, a patch of rough surface placed within a sub-world facilitates the simulation of arbitrarily large rough surfaces without the extensive memory consumption. Furthermore, different rough patches can be combined by using multiple sub-worlds. In the following, special surface configuration, like a partially polished surface, can be created by defining a map between the portal and sub-worlds by hand. If not defined by hand, the map can be generated randomly, while the share of each sub-world in the map can be defined.

Setting up a portal can be tedious work due to various parameters that must be managed, the multiple volumes required, and the linking between the portal and sub-worlds. To simplify this, a portal generation helper class was implemented. It abstracts the configuration of the Geant4 volumes, the linking processes and the preparation of the map between the portal and sub-worlds as well as the registering of the volumes to the correct store, and permits a simpler and less error-prone usage. Moreover, some safety checks are included (e.g. portal size is a

```
/Surface/MultiportalHelper/<HelperName>/setVerbose <0-5>

/Surface/MultiportalHelper/<HelperName>/setDxPortal <doubleAndUnit>
/Surface/MultiportalHelper/<HelperName>/setDyPortal <doubleAndUnit>
/Surface/MultiportalHelper/<HelperName>/setDzPortal <doubleAndUnit>

/Surface/MultiportalHelper/<HelperName>/setDxSubworld <doubleAndUnit>
/Surface/MultiportalHelper/<HelperName>/setDySubworld <doubleAndUnit>
/Surface/MultiportalHelper/<HelperName>/setDzSubworld <doubleAndUnit>

/Surface/MultiportalHelper/<HelperName>/setNxSubworld <int>
/Surface/MultiportalHelper/<HelperName>/setNySubworld <int>

/Surface/MultiportalHelper/<HelperName>/setMaterial <material>
```

Figure 4.5: Macro commands of helper class for portal generation controlling different parameters. Arguments are marked with '<...>' and include either the data type or a hint on the expected type of argument. In one simulation multiple helpers for different portals can be used. To address this, each helper must be named by the user. This name must then be used for <HelperName> to apply the command to the correct helper.

multiple of sub-world size) to the helper class. For convenience, the portal generation helper class can be controlled via macro commands (see Figure 4.5).

4.4.3 Particle Generator

Geant4 provides different particle generators to place particles or isotopes, as starting points for simulating an event. They can be placed at a single defined position, or sampled from within or the surface of a simple volume like a cube, cylinder or sphere. However, because of the more complex structure of a rough surface and the use of portals/sub-worlds Geant4s provided particle generators are not sufficient. To address this, a new one was defined and customized for rough surfaces. It allows users to sample points uniformly distributed on the rough surface.

When simulations employ multiple sub-worlds with varying rough patches, it is imperative to sample grid coordinates not uniformly but in accordance with the surface area pertinent to the rough surface patch within each sub-world. To facilitate this, a bespoke C++ sampler class has been developed. This class aggregates all the sub-worlds along with their respective rough surface patches, evaluates their surface areas, and calculates the probability for coordinate selection. This ensuing class is utilized to sample grid coordinates and their associated sub-worlds and rough surface patches. Subsequently, a random point is sampled from the respective rough surface patch.

This procedure ensures the points are uniformly distributed over the entirety of the surface.

Placing different nuclei on the rough surface may serve as a contamination of the same. To achieve a uniform distribution, two aspects must be addressed: a) generating uniformly distributed points on a single patch of rough surface. This involves collecting all G4TriangularFacets, which are triangular elements that exactly represent the surface of the spikes. Then sampling from them with respect to the area the single G4TriangularFacet represents in comparison to the total area (sum of all G4TriangularFacets). Subsequent to facet selection, a random point within the selected facet can be sampled using the implementation of Geant4. A comprehensive discussion for sampling uniformly distributed points on a surface is available in [83]. b) Sampling sub-worlds and the corresponding grid coordinates. When simulations employ multiple sub-worlds with different rough patches, it is important to sample grid coordinates not uniformly but in accordance with the surface area represented by the patch of the rough surface in the corresponding sub-world. To facilitate this, an extra C++ sampler class was developed. This class aggregates all the sub-worlds of the grid coordinates with their respective patch of rough surface, evaluates their surface areas, and calculates the probability for coordinate selection. Subsequently, a random point is sampled from the respective patch of rough surface.

This procedure permits to sample points uniformly distributed over the surface.

```
/shift/verbose <0-5>
/shift/printShiftTable

/shift/loadShiftTable <filePath>
/shift/setMinShift <doubleAndUnit>
/shift/setMaxShift <doubeAndUnit>
/shift/confineToMaterial <material>
```

Figure 4.6: Macro commands controlling the shift class via macro files. Arguments are marked with '<...>' and give a hint on or include the expected data type.

Extension of Particle Generator by a Shift

Using the module's built-in particle generator allows for uniform sampling of points across a rough surface that simulates surface contamination. However, surface contamination is likely not to be found precisely on the surface but beneath the surface following some density distribution. This is addressed by the shift, which is an additional step that can be added to the particle generator previously discussed. This add-on shifts a point along a user-defined direction by a value that is sampled from a distribution. The distribution itself can also be defined by the user. This process enables the user to simulate more realistic contamination of a rough surface by implanting the contaminants inside the roughness, discussed in (see subsection 4.4.1).

The density distribution can be defined by a histogram via a text file, which can be loaded by the shift class. The file contains an ordered list of depths accompanied by the corresponding value that denotes the height of the distribution at each depth. The magnitude of the distributions heights is arbitrary, since only the relative heights are important for sampling. When processing the file, the sum of the heights get normalized to one anyway. Furthermore, because a histogram is not continuous, when sampling from this distribution, the values will undergo linear interpolation, enabling the generation of any intermediate depth value within the defined values.

When applying the shift in combination with the particle generator on a rough surface, the particle generator samples a point from the surface and passes it including the corresponding surface normal vector to the shift class. The shift class samples a value from the distribution and shifts the point along the normal vector by the sampled value.

Furthermore, the shift class is equipped with special options: a) the minimal shift defines a minimal return value from the sample algorithm, b) the maximal shift defines a maximal return value from the sample algorithm, and c) to confine values to materials to only return sample points that are in a Geant4 volume with the selected material. All functions and the path of the distribution file can be controlled via Geant4 macro files (see Figure 4.6). Figure 4.7 depicts an example usage of the shift class, including the usage of a defined distribution and the application of all three mentioned special functions (minimal-, maximal shift and confine to material).

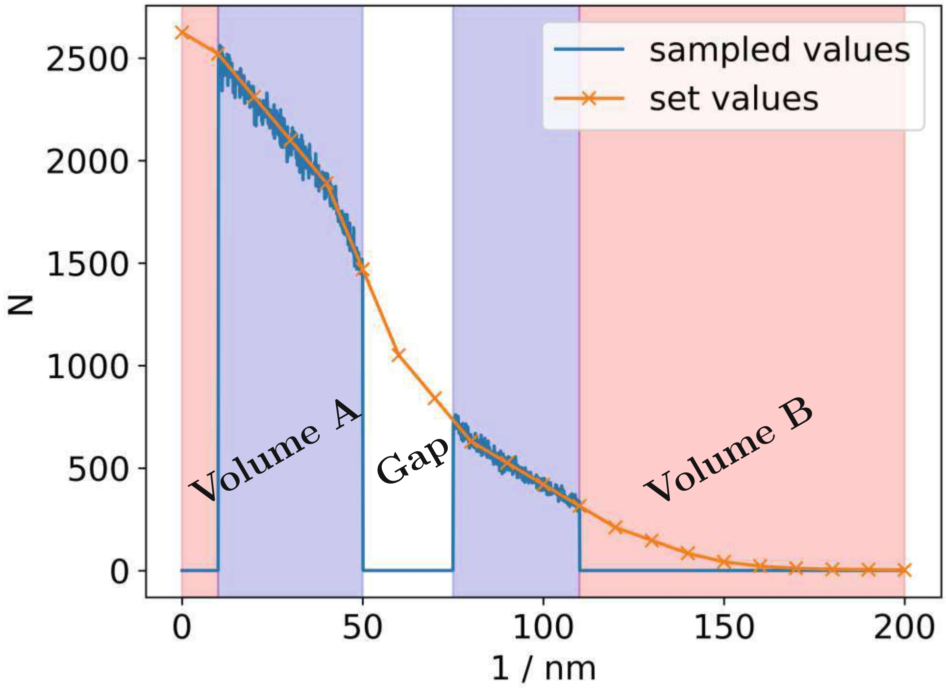

Figure 4.7: Example of sampled values for a shift (blue) based on a defined distribution (orange, the x marker are the set values in the distribution file, the line represents the linear interpolation between them) in the range of nm. In the example, two Geant4 volumes out of $CaWO_4$ (marked as red and blue areas) are placed in line with a gap (50 to 75 nm) between them. Although the distribution is non zero in the areas marked as red (0 to 10 nm, 110 to 200 nm) and white (50 to 75 nm) no points are sampled in this ranges due to special options set for shifting: a) a minimal shift of 10 nm is set, therefore no values are sampled in the first red marked area. b) a maximal shift of 110 nm is set, therefor no values are sampled in the second red marked area. c) the shift is confined to the material $CaWO_4$ but the white area is a gap between the two volumes, therefore not points are sampled from (50 to 75 nm).

5 | Background Model

Although various measures are taken to reduce the rate of various background sources, as elaborated in section 3.5, some background is still inevitable.

To distinguish DM from background noise, it is important to fully understand each source that contributes to the measured data. This can be achieved through the use of MC-based simulations. The used simulation tools are introduced in chapter 4. The simulation is divided into three phases: initially, the various sources and their interaction with the experimental setup are simulated using ImpCRESST. The simulated events, including hit information, the trajectories and additional data, are archived in root files specific to ImpCRESST. Subsequently, with CresstDS finite time and energy resolution of the detector are applied to the simulated data. Through this procedure, energy deposition templates for each source and nuclide are generated; this encompasses bulk contamination of the target material, as well as from the holders, foil, shielding and potential cosmogenic activation. Finally, these templates are fitted to the actual measured data using a Bayesian likelihood fit normalization method with Bliss [12].

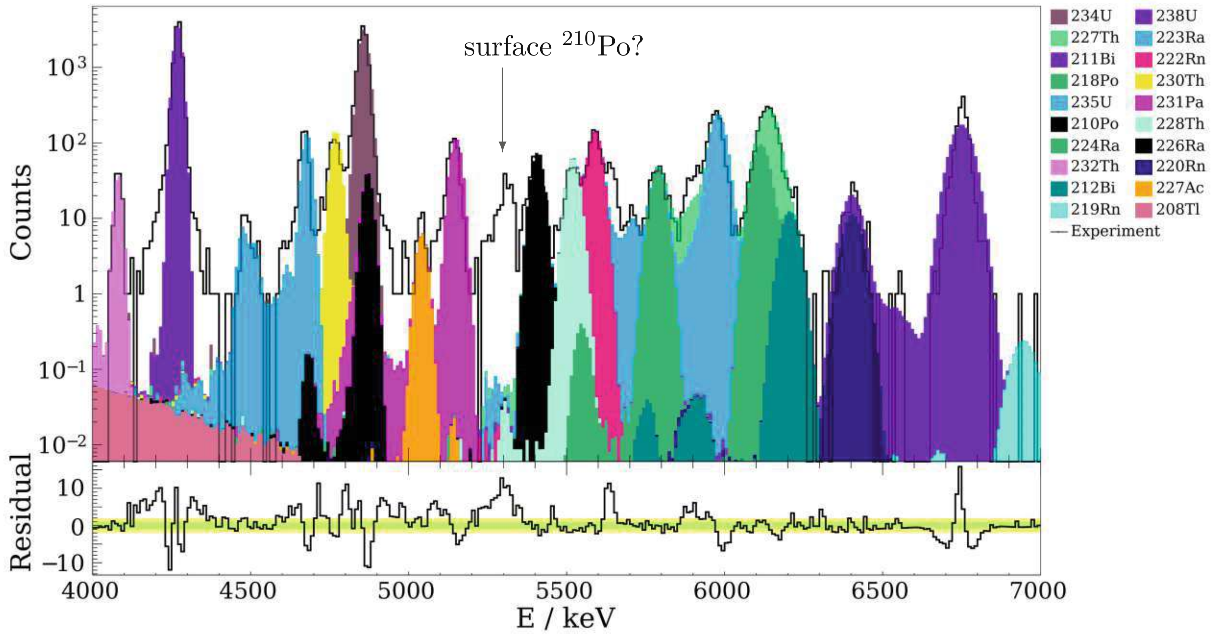

Figure 5.1: Simulated spectra caused by α-decaying bulk- contaminants (colored, filled histograms) fitted [12, 66] to experimental data (black, open histogram) of CRESST's TUM40 detector [84]. For convenience of the reader this and the fits for the energy ranges $500 - 2800$ keV, $50 - 600$ keV and $1 - 50$ keV are in a bigger format added to appendix: Figure A.1, Figure A.2, Figure A.3, Figure A.4.

The result provides a detailed overview of the different sources and activities of the individual component groups of the experimental setup (e.g. holders, foil) and helps to gain a better understanding of their contributions to the spectrum obtained by CRESST. In Figure 5.1) the fit results for TUM40 data are presented.

The simulation encompasses a comprehensive range of effects (e.g. cosmic activation, geometry of the setup) and sources (e.g. bulk contamination, ambient γ-rays) that contribute to the observed energy deposition spectrum [11]. However, discrepancies between the simulated and experimental data suggest that either certain effects may be underestimated or that some additional sources are not considered in the simulation. In response, a recent study conducted by me [13], has for the first time added the effects of surface roughness and its contamination of the target crystal as a proof of concept, effectively addressing some of these discrepancies seen in the TUM40 data (see Figure 5.1).

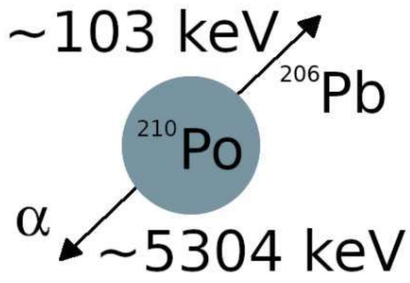

Figure 5.2: ^{210}Po decays via α-decay. The kinetic energies of its decay products are: the α-particle has 5304.38 keV, the ^{206}Pb nuclide has 103.08 keV.

The rough surface of the detector crystal TUM40 was emulated by placing approximately 800×800 spikes with dimensions in the range of µm. Surface contamination was simulated by placing ^{234}U, ^{238}U, ^{210}Po and ^{231}Pa precisely onto the rough surface of a $CaWO_4$ crystal. Here, ^{210}Po is of particular interest due to the uncovered and clear peak at $\sim$ 5304 keV in the α energy range of Figure 5.1. Moreover, surface ^{210}Po was already measured by CRESST [55] and identified as a non-negligible source by other rare event search experiments such as CUORE [14].

The nuclide ^{210}Po is a progeny within the ^{222}Rn decay chain. ^{222}Rn is a naturally occurring radiogenic gas that emanates from the soil. Depending on the region, its activity near the ground can exceed 150 kBq/m^3 [75]. Within the decay sequence of ^{222}Rn, a notable constriction occurs at ^{210}Pb, which has a half-life of approximately 22.2 yrs. A detector crystal that is exposed to normal air, which is likely to include some ^{222}Rn, can be contaminated by decay products of ^{222}Rn and eventually with ^{210}Pb.

The detector's surface will consequently be contaminated with ^{210}Pb, which itself initiates a decay chain and continuously contributes to the measured data. The predominant decay path involves a β-decay of ^{210}Pb resulting in ^{210}Bi (Q = 63.5 keV), followed by a subsequent β-decay yielding ^{210}Po (Q = 1162.1 keV) and ultimately an α-decay producing ^{206}Pb (Q = 5407.5 keV). The latter nuclide is stable.

Because ^{210}Po undergoes α-decay, the resulting decay products possess a fixed kinetic energy (see Figure 5.2). This characteristic helps to identify the energy deposited within the spectrum; Due to this and missing entries in the high alpha energy range at the energy of the α particle from ^{210}Po decay, this nuclide is of special interest. In Figure 5.3, the energy deposition spectrum of ^{210}Po decay on a rough $CaWO_4$ crystal surface is illustrated. The height of the spikes, which is correlated with the roughness level, evidently affects the energy deposition spectrum. A comprehensive discussion is available in [13].

Nevertheless, I want to highlight the most salient characteristics of the spectrum: two distinct peaks are observable in the high energy domain. One peak corresponds to the kinetic energy of the α-particle (5304.38 keV), henceforth referred to as the α peak. The other peak aligns with the cumulative kinetic energies of both decay products, the α-particle and the ^{206}Pb nuclide (5407.46 keV) and will be designated as the mixed peak. As the spike height increases, representing an increase in roughness, the α peak decreases, while the mixed peak increases. The reallocation of counts from the α peak to the mixed peak is likely due to an increased probability of interaction between the decay products and the rough surface in the presence of higher spikes. In the event of ^{210}Po decays, due to momentum conservation, the resultant products travel in opposite directions. Consequently, when placed on a planar surface, one product impacts the detector while the other escapes it. The impacting α-particle or ^{206}Pb nuclei can deposit a share of their energy in the crystal, whereas the escaping product does not deposit any energy at all. With an increase in spike height, the likelihood that both decay products interact with the detector and deposit some energy correspondingly increases. This, when applied to the data, suggests that the observed reallocation of counts from the α to the mixed peak occurs because now both decay products are depositing all or at least almost all of their energy within the crystal.

In contrast, in the lower energy range of the spectrum, there is an additional peak corresponding to the kinetic energy of the ^{206}Pb nuclide (103.08 keV), refereed to as the ^{206}Pb peak. It is clearly visible that, with increasing spike height, this peak decreases, whereas the spectrum adjacent to the peak at higher energies increases.

A notable increase in the spectrum adjacent to the ^{206}Pb peak can occur if both decay products interact with the detector, yet the α-particle still escapes depositing just a share of its energy. Alternatively, some energy could be dissipated subsequently as a result of deexcitations. It should be noted that at least the full energy equivalent of the ^{206}Pb is deposited, leading to a conspicuously sharp drop in counts towards lower energies at the ^{206}Pb peak.

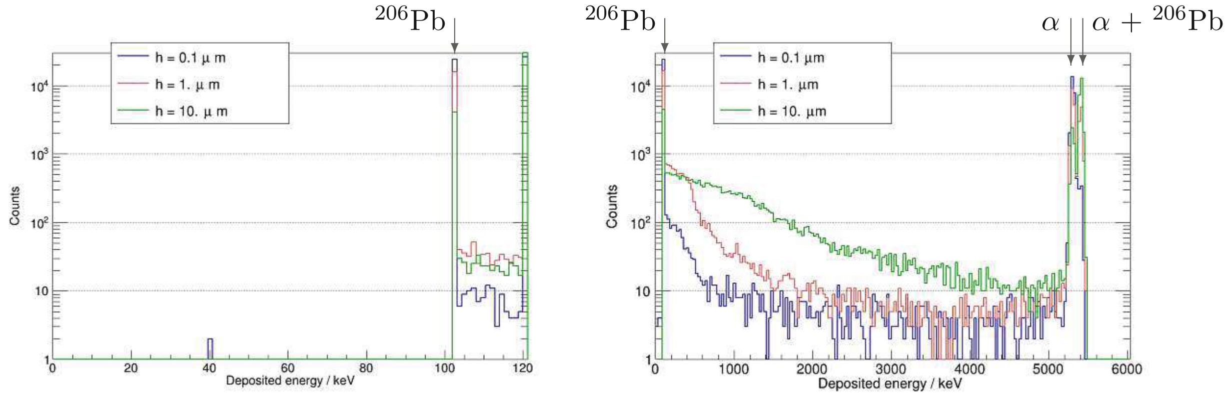

Figure 5.3: Energy deposition spectra from simulations of a rough detector surface with ^{210}Po placed on the surface. The height h of the spikes is varied in the µm range. The plot (left) shows the low energy range including the ^{206}Pb peak at $\sim 103\,\mathrm{keV}$. The plot (right) shows the full energy range that includes a ^{206}Pb-, the α- ($\sim 5300\,\mathrm{keV}$) and a mixed (α+^{206}Pb)-peak ($\sim 5400\,\mathrm{keV}$). The detector resolution is applied to the data of the right plot. Figures are taken from [83].

Although this simulation served as a proof of concept, this simple model already demonstrates that surface roughness and contamination can have a significant non-negligible effect on the measured background. Spectra with similar characteristics to those of ^{210}Po (see Figure 5.3) can be simulated for ^{234}U, ^{238}U and ^{231}Pa [13]. In Figure 5.4, it is evident that the simulated nuclides conform well within the high energy spectrum. Particular emphasis is placed on the simulations involving ^{238}U and ^{210}Po. ^{238}U effectively addresses the missing left tail of the ^{238}U peak observed from bulk simulations, while ^{210}Po compensates for the peak around $\sim 5300\,\mathrm{keV}$. The integration of surface contributions enhances the coverage of high energy data by 0.02 %.

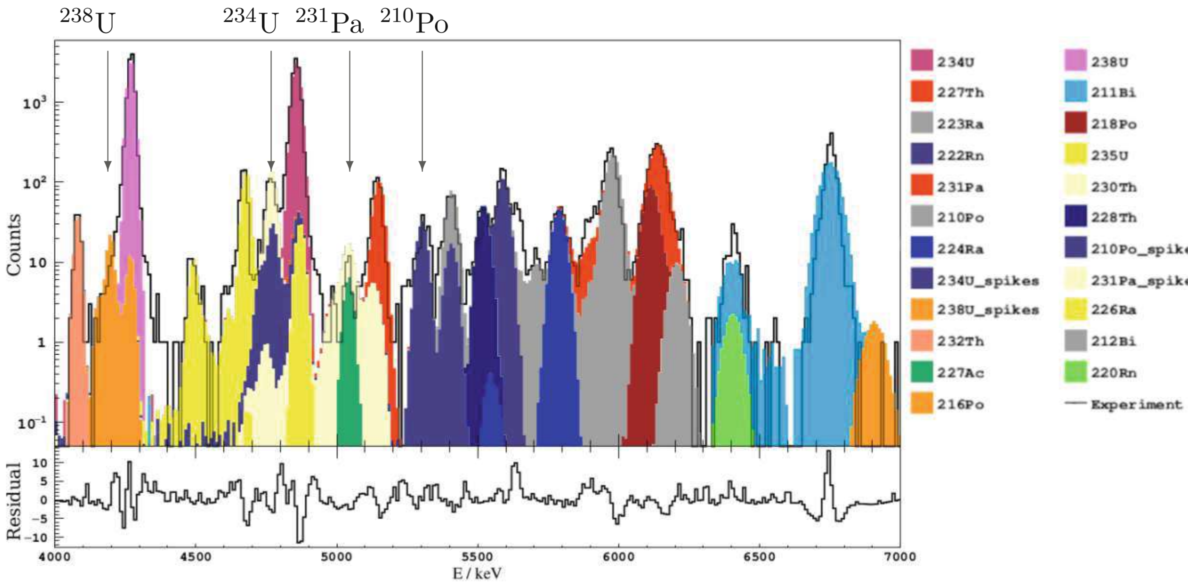

Figure 5.4: Simulated spectra caused by α-decaying bulk- and surface-contaminants (colored, filled histograms) fitted [12, 66] to experimental data (black, open histogram) of CRESST's TUM40 detector [84]. The surface contaminants ^{210}Po, ^{231}Pa, ^{234}U and ^{238}U are placed on a rough, spiked surface. Figure taken from [13].

Despite these promising first results of the study conducted as a proof of concept [13], some details of the spectrum are not explained by the simulation. For example, the extreme left segment of the peak at $\sim 5300\,\mathrm{keV}$ remains uncovered by the simulated energy deposition spectrum. I must emphasize that this uncovered area is small compared to the covered peak area and might not address a problem in the simulation. However, it could be an indication that additional surfaces of components of the experimental setup might contribute to the measured spectrum. Furthermore, the abrupt drop in counts for energies lower than that of the ^{206}Pb peak of the spectrum in Figure 5.3 is conspicuous. It is plausible that following the decay of ^{210}Po, the α-particle escapes and the ^{206}Pb nuclide undergoes backscattering from the surface, depositing only a fraction of its energy. These observations raise questions about the adequacy of the physical models employed in surface simulations.

A possible source of these observations can be the positioning of contamination. In the simulations conducted, the nuclei are positioned exactly on the surface of the spikes. However, in practical scenarios, contamination is anticipated to occur within a subsurface layer, likely to follow some distribution depending on the depth below the surface. As discussed in [13], this will also influence the deposition of energy, because the decay products below the surface must traverse some detector material before escaping, subsequently depositing a portion of their energy. All of these possible problems and their solutions are addressed in the following chapter of this thesis.

6 | Surface Simulation

Using the suite of simulation tools discussed in chapter 4, numerous surface simulations are perfomred to scrutinize the effects of surface roughness and its contamination on the measured energy deposition spectra of TUM40 and TUM93A. Here, the nuclide ^{210}Po is of particular interest due to its anticipated increased concentration on the surface of the target crystal as a consequence of contamination through the ^{222}Rn decay chain and its classification as an α-decaying nuclide. As a consequence of α decay, the emitted products exhibit a well-defined kinetic energy: approximately 5304 keV for the α particle and 103 keV for the ^{206}Pb nuclei.

Before simulating the effects of rough surfaces, the Geant4 physics-models for simulating nuclear scattering is examined. Based on this analysis, an appropriate physics model is selected. This investigation is triggered by previous findings [13] concerning surface simulations of ^{210}Po nuclei on rough surfaces. See chapter 5 for a brief discussion of the findings and possible problems. This ensures that the chosen physics model is optimal for the intended simulations of surface near ^{210}Po.

Subsequently, the influences of various surface and contamination parameters, such as the height of the target crystals roughness (height of simulated spikes representing the roughness) or the contamination implantation depth beneath the surface are scrutinized. Furthermore, the impact of an external contaminated, rough surface facing the target crystal is evaluated. The findings of these simulations are utilized to generate more sophisticated energy deposition templates for ^{210}Po and fit them to the measured spectra by CRESST using Bliss and a likelihood normalization fit method [12].

Next, a potential contribution from surface ^{238}U is investigated due to the difference in the deposition spectrum adjacent to the ^{238}U peak in the fit of the high energy domain in Figure 5.1. The findings are then used to simulate surface templates for TUM93A too.

6.1 Testing the Nuclear Recoil Physics Model for Simulations

In [13] a preliminary test was performed to model the contamination of a rough surface of a $CaWO_4$ crystal characterized by similar-looking spikes with a height and width in the order of µm. ^{210}Po nuclei were positioned exactly on the surface of these spikes, simulating surface contamination. The energy deposition spectrum resulting from the decay of ^{210}Po indicates that surface roughness and its contamination significantly influence the measured spectrum. Although some promising results are achieved, as described in chapter 5, the simulated spectrum also raises several questions. The ^{210}Po exhibits a sharp cut-off to lower energies at approximately 103 keV , which aligns with the energy of the ^{206}Pb peak. Below this threshold, the counts of deposited energy are negligible. This observed phenomenon is rather peculiar. After the decay of ^{210}Po it is anticipated that the α-particle may escape, while the ^{206}Pb nucleus is backscattered, thus depositing only a fraction of its energy. This event should result in entries below 103 keV. The absence of these events suggests that the electromagnetic physics model employed in the simulation may be inadequate for surface simulations.

ImpCRESST employs the provided physics list EMStandardPhysicsOption_4 (EMOption4) as its default option. EMOption4 is a widely used physics list that incorporates multiple different models applicable to various particles and nuclei over a broad energy range from sub-keV to TeV [76]. However, in this thesis, a limitation in EMOption4 was identified arising from the interaction model G4Mulitscattering, it employs at energies around ~ 100 keV. This was tested using a small experimental simulation setup: A current of 5×10^4 ^{206}Pb nuclei was impelled with an energy of 103.08 keV on a $CaWO^4$ crystal normal to its flat surface. This energy is chosen to mimic the kinetic energy of ^{206}Pb after the decay of ^{210}Po. The dimension of the $CaWO_4$ crystal is in the range of cm such that the scattered ^{206}Pb nuclei will not escape the crystal except for the case of backscattering when the nuclei exit the crystal through the same surface through which they entered the crystal. Different penetration depths with different variations of physics configurations in EMOption4 are studied and results are compared with those obtained from an alternative simulation tool, Stopping and Range of Ions in Matter (SRIM).

The simulation is repeated for three different physics configurations: a) using the standard physics list EMOption4 in its default state without additional modifications. b) using EMOption4 again, but with a prescribed step limit of 1 nm. This constrains the maximum step length computed per calculation cycle and can be applied to volumes and/or materials. Setting such a limit is particularly crucial for small geometries to ensure the execution of multiple iterations of physics computations within its spatial confines. c) using EMOption4 but with an adapted model for low energetic ions. The multi scattering process is deactivated and replaced by an implementation known as Screened Nuclear Recoil (SNR) for energies less than 1 MeV. Multi scattering, which is a component of the Geant4 core library, allows the simulation of multiple scattering events of a tracked particle within a single simulation step by approximating a lateral displacement and change in momentum direction. This approach enhances computational efficiency by not simulating all individual scattering events. SNR is a physics process developed for Geant4 for the efficient computation of screened Coulomb interatomic scattering [85].

In Figure 6.1 the positional histograms for different configurations are compared with the simulation result of the software SRIM. SRIM is a widely used tool for simulating the stopping of ions in matter, particularly in the context of ion implantation, sputtering or transmission [86]. Since 1985, it has been updated multiple times, and more stopping values have been added to enhance its accuracy. Due to its good reputation, the simulation outputs generated by SRIM are currently considered reliable.

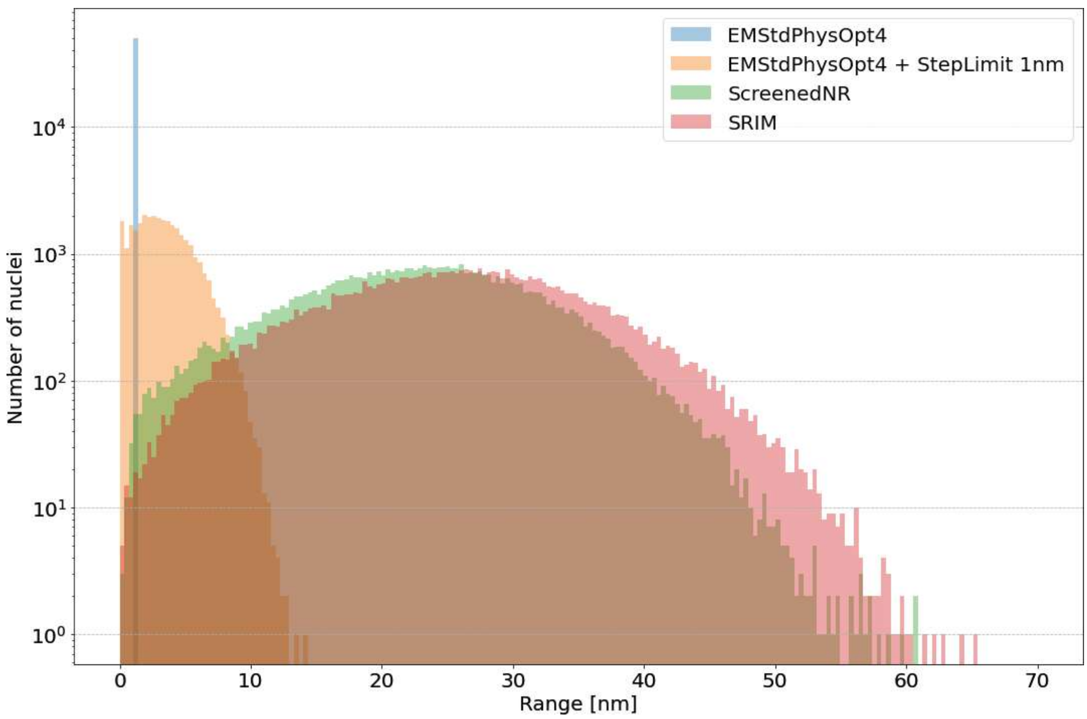

Figure 6.1: Comparison of penetration depth of 5×10^4 ^{206}Pb nuclei shot normal to the surface of a $CaWO_4$ crystal with a kinetic energy of 103.08 keV for different physics simulation configuration and SRIM. The histogram shows the number of nuclei stopped at that depth below the surface of the crystal.

The simulations performed with EMOption4 exhibit a clear discrepancy compared to SRIM. Using the default EMOption4 version, all ^{206}Pb nuclei were stopped exactly at the same depth, producing a single distinct peak as illustrated in Figure 6.1. Further analysis indicates the absence of scattered nuclei, with each nucleus being stopped after one simulation step. This observation suggests a fundamental flaw, probably indicating the necessity for the implementation of a step limit. Refer to Table 6.1 for detailed penetration depths and the number of nuclei counted within the crystal after simulation.

Implementing a step limit does not alter the simulated physics; however, it enhances the accuracy of the simulation by performing more computations. Consequently, the integration of a step limit does not compromise the validity of the physics simulation. However, it increases computational time as a greater number of simulation steps must be performed. Now, the simulation executes multiple computation steps per nuclide, yet the perceived penetration depth appears insufficient. The positional spectrum remains dissimilar to the spectrum calculated by SRIM. Additionally, approximately 36.6 % of all nuclei are backscattered and do not end up in the crystal.

By replacing the multiscattering model with SNR, it is feasible to generate a position spectrum similar to the spectrum produced by SRIM. Despite the existence of some discrepancies, they are deemed acceptable. This is justified because SNR was compared with SRIM in an other study [85] too, there the differences were seen as acceptable; however, this other study simulated boron and argon nuclei with a silicon target and was only assessing energies as low as 10 keV. Furthermore, given the insufficiency of data on the stopping power of ^{206}Pb in $CaWO_4$, even SRIM is subject to some margin of error. Especially for kinetic energies $\lesssim 1$ keV the simulation diverges compared to SRIM. Only real measurements investigating the stopping of ions with a kinetic energy less than 10 keV in $CaWO_4$ can finally confirm and help fine-tune the simulation model to its lowest energies.

Table 6.1: Table contains the number of counted ^{206}Pb that are deposited inside a $CaWO_4$ crystal after shot at its surface with a fixed energy of 103.08 keV, the mean penetration depth and its standard deviation in nm.

	Counts	**Mean** [nm]	**Std** [nm]
EMStdPhysOpt4	50000	1.35	0.00
EMStdPhysOpt4 + StepLimit 1 nm	31695	3.41	2.16
ScreenedNR	49994	22.93	8.87
SRIM	49960	25.95	9.50

6.1.1 Effect of Opt4 and SNR on Surface Roughness Simulations

In Figure 6.1, it has been observed that the physics model and selected paramters can significantly influence the simulations of low energetic (< 1 MeV) nuclei moving only some nm. When employing default physics list EMOption4, simulations of the nuclei terminated after a single step with all nuclei traversing an identical spatial distance. In contrast, using the model SNR, replacing multi scattering, multiple computational steps per nucleus were performed, resulting in a more physical movement. The investigation indicates that SNR is more appropriate for surface simulations compared to the default and widely used EMOption4.

Next, we investigate how the energy deposition spectrum of ^{210}Po on a rough surface will change when using SNR compared to the default physics list. For Figure 6.2 2×10^4 ^{210}Po nuclei are placed exactly at a rough surface with 5 µm high and wide spikes of a $CaWO_4$ crystal. The study uses two different physics implementations: the default EMOption4, which was used in a previous study [13] and SNR replacing multi scattering. Comparing both simulations, we can see that the overall shape of the spectrum is the same. Three peaks are visible in each simulation: the ^{206}Pb peak at $\sim$ 100 keV, the α peak at $\sim$ 5300 keV and the mixed (α + ^{206}Pb) peak at $\sim$ 5400 keV. However, some discrepancies are observed: when comparing the mixed peaks, the application of the SNR model results in a tail to the left of the peak. This may happen because ^{206}Pb can now interact with the rough surface multiple times and its mean travel path in one

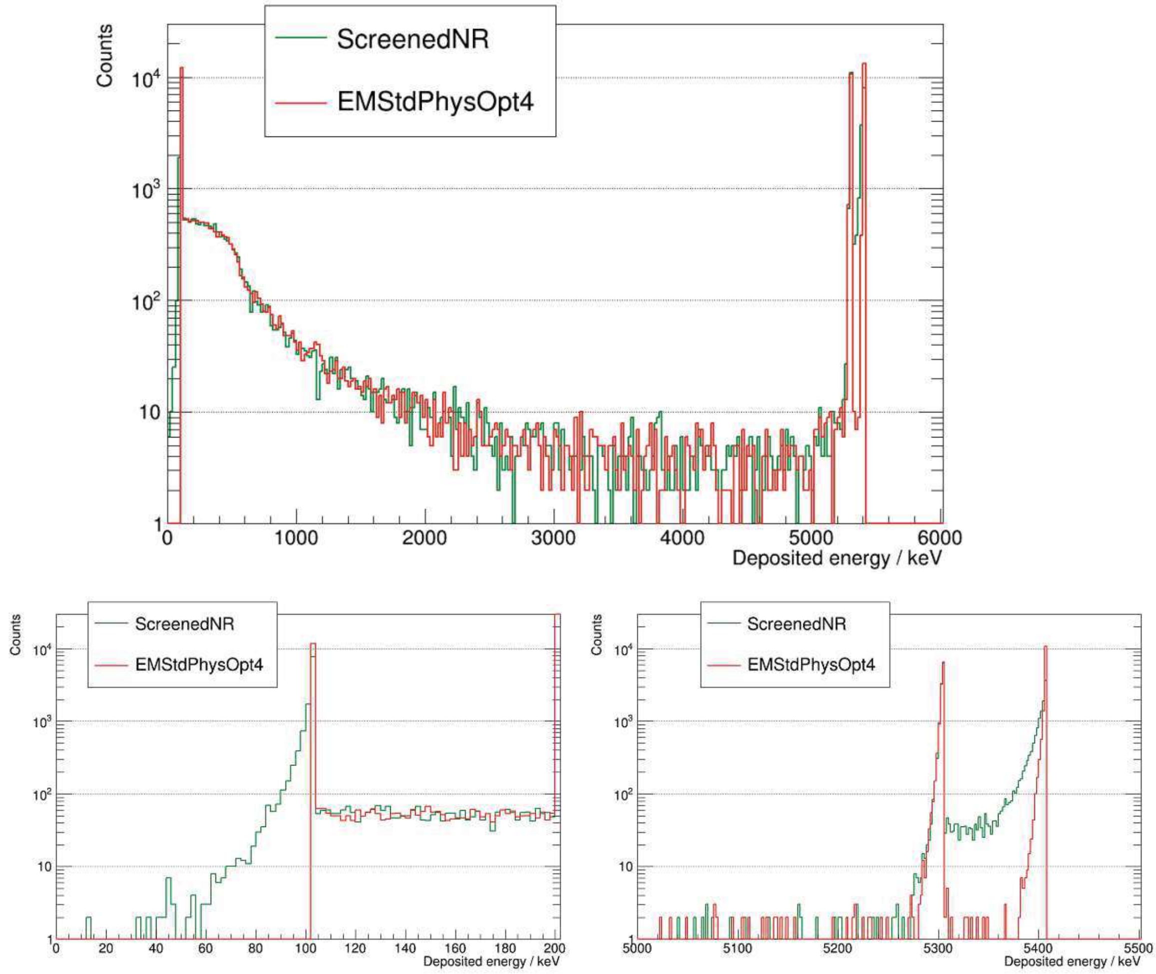

Figure 6.2: Energy deposition spectrum of 2×10^4 ^{210}Po decaying exactly at the surface of 5 µm high and wide spikes of a $CaWO_4$ crystal. Two different physics implementations are used: ScreenedNuclearRecoil and EmStandardPhysicsOption_4.

direction is longer by a factor of ~ 17. Therefore, it is more likely that it penetrates some spikes and deposits a portion of its energy before escaping the detector. With default EMOption4, it was more likely that the nuclide was stopped inside the detector material or escaped without any trace, due to the short mean distance traveled and the fact that it was stopped just in one simulation step.

The same argument holds for the ^{206} Pb peak, which now has a tail on its left side, indicating that it could be possible that the ROI could be affected.

6.1.2 Simulation of ^{210}Po Implantation Depth Resulting from ^{222}Rn Decay

RSM is used along with ImpCRESST (see chapter 4) for simulating energy depositions from surface contamination. RSM requires the distribution of contaminants as input, which can be obtained either from surface measurements, such as those performed with SIMS [87], or from a prior simulation. Due to the lack of available measurements at the time of writing this thesis, we rely on simulations for the contaminant distribution.

It is assumed that contamination occurs mainly via the decay chain of airborne ^{222}Rn which accumulates on the surface of the crystals due to adsorption. In this simulation, the decay of 5×10^5 ^{222}Rn nuclei down to ^{206} Pb is simulated, including ^{210}Po. As the lateral displacement of the nuclei is not of interest for a depth distribution, all nuclei are placed at the same point

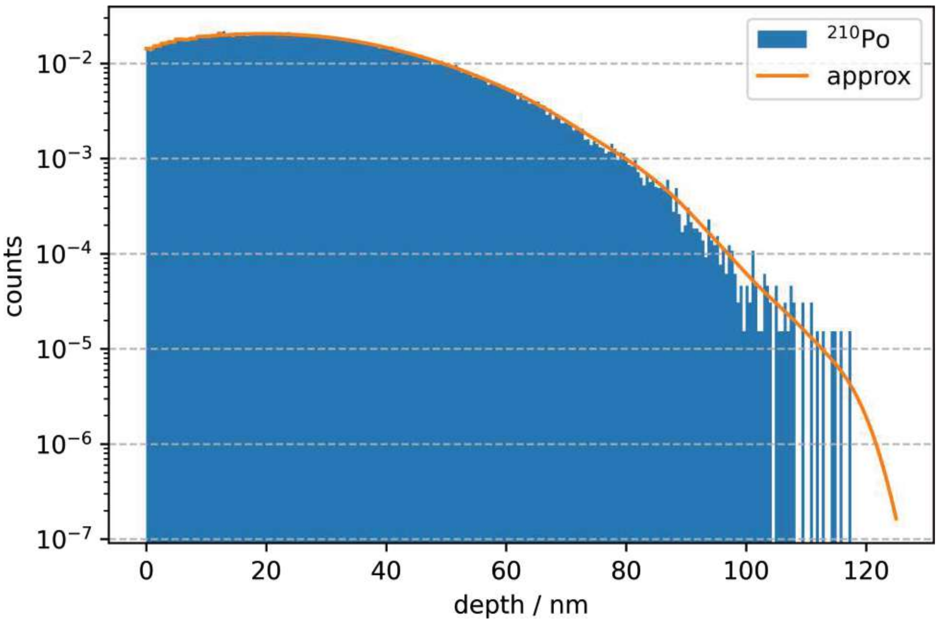

Figure 6.3: Implantation depth of ^{210}Po when ^{222}Rn nuclei are placed at the surface of a $CaWO_4$ crystal and all decays of the decay chain until ^{210}Po are simulated. For simulation the SNR physics implementation is used. The bin width is 0.5 nm. A probability density function is fitted to the position histogram using SciPys pdf-function for the first 10 % of depth and its gaussian kernel density estimation (gaussian_kde) for the rest. The split was done to fit a smooth approximation of the histogram.

in the middle of the surface of a flat $CaWO^4$ crystal. The dimension of the simulated $CaWO^4$ is large enough that no nuclei escape through the sides of the crystal. Finally, the depth of the nuclei normal to the surface was extracted.

In Table 6.2, the nuclei involved in the main decay chain are listed with their number of counts compared to the number of simulated ^{222}Rn, the number of counts compared to the number of their mother nuclei, their average implantation depth in nm, and their main decay channel. It should be noted that mainly α decays influence the depth of implantation. For Figure 6.3, a histogram of the ^{210}Po positions was generated. To smooth the ^{210}Po distribution, a probability density function (pdf) was fitted to the simulation data. This makes the distribution applicable for further simulations to sample a starting position for ^{210}Po nuclei from the distribution. The final position of ^{210}Po is in the range ~ 100 nm below the surface with an average position of 28.53 nm.

Table 6.2: Table of nuclei from the ^{222}Rn decay chain. 5×10^5 ^{222}Rn nuclei are placed at the surface of a plain CaWO^4 crystal and the whole decay chain until ^{206}Pb is simulated. Table represents the number of nuclei in relation to the total number of simulated ^{222}Rn, the number of nuclei compared to the number of its mother nuclei, the mean depth below the surface and the nuclides main decay channel. Only nuclei of the main decay chain are listed. [1]The number of ^{214}Bi nuclei can be bigger than ^{214}Pb nuclei because of different decay paths leading to the same nuclide. There is a probability of $\sim 0.02\,\%$ that ^{218}Po decays to ^{218}At and then to ^{214}Bi

	Counts %	Δ %	**Mean** [nm]	**decay channel**
^{222}Rn	-	-	0.000	α
^{218}Po	44.05	44.05	12.125	α
^{214}Pb	33.16	75.28	20.603	β^-
^{214}Bi	33.17	100.02[1]	20.604	β^-
^{214}Po	33.16	99.97	20.604	α
^{210}Pb	26.67	80.41	28.529	β^-
^{210}Bi	26.67	100.00	28.529	β^-
^{210}Po	26.67	100.00	28.530	α
^{206}Pb	23.67	88.76	33.156	β^-

6.2 Simulations of surface roughness contaminated by ^{210}Po

The contribution of surface ^{210}Po to the energy deposition spectrum measured by CRESST is of special interest. This interest arises due to events found at an energy of ~ 5300 keV [60] likely coming from ^{210}Po decays. However, when the simulation data are fitted to the measured TUM40 data [12, 44], none of the simulation templates based only on bulk contamination account for this peak. The observed energy indicates that for some events only the α particle (~ 5304 keV) resulting from the decay of ^{210}Po contributes to the spectrum. This scenario is only feasible if ^{210}Po is an external source or if the decay occurs near the surface, allowing ^{206}Pb to escape without depositing some relevant energy. In the following, different scenarios are tested using TUM40 data as a test case.

6.2.1 Different Spike Heights

To deduce a clearer picture regarding the influence of a rough surface in combination with surface ^{210}Po on the energy deposition spectrum, we probe different spike heights representing different roughened surfaces. Previous simulations have shown that ^{206}Pb can move only a maximum of ~ 60 nm in a single direction within a CaWO$_4$ (see Figure 6.1). At depths greater than this limit, ^{206}Pb will always deposit its kinetic energy inside the crystal. To emphasize the effects of a rough surface and minimize simulations in which the entire kinetic energy of ^{206}Pb is always detected, ^{210}Po is exactly placed on the rough surface.

For generation of Figure 6.4 5×10^4 ^{210}Po nuclei are placed exactly on a rough surface of a CaWO$_4$ crystal. The width of the spikes is fixed at 5 µm, while the height h is varied. The dimension of the spike is chosen based on surface measurements (see section 3.4), which show that rough surfaces have spikes in the dimension of µm.

Clear differences are noticeable for different heights of spikes, even though the rudimentary shape of the distribution of energy deposition remains unchanged across all values. In the low energy region, left of the ^{206}Pb peak at ~ 100 keV a tail can be observed. For $h = 1$ µm, it can even extend to the ROI. This deposited energy is likely due to ^{206}Pb being either backscattered from the surface or traversing through a small part of the roughness, like an edge, while the α particle escapes as well. This reasoning is supported by a decomposition of the energy deposition spectrum in Figure 6.5. The spectrum counts the distribution of both ^{210}Po decay remnants contributing to the measured deposited energy. It is clearly visible that the aforementioned tail is mainly induced only by ^{206}Pb depositing its energy. However, as the height of the spikes

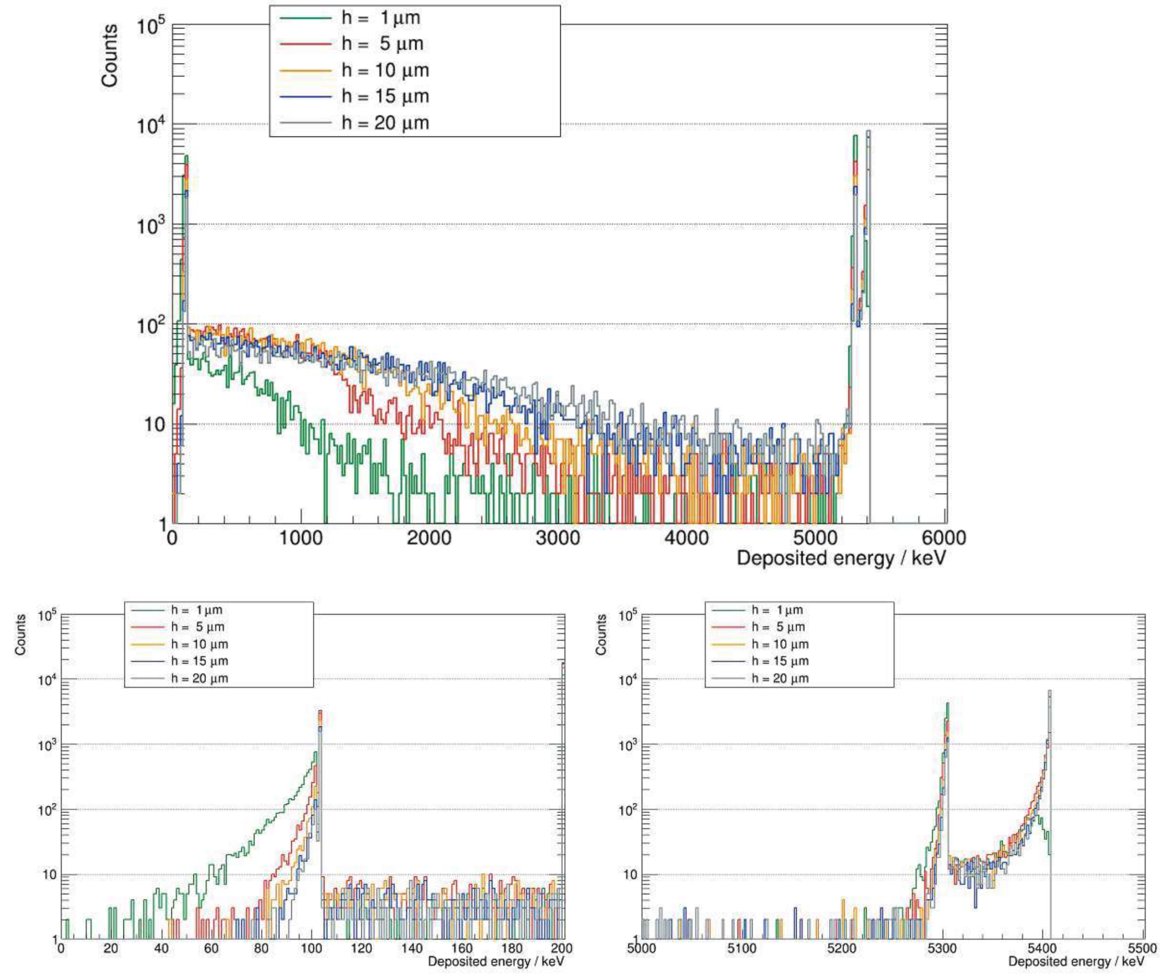

Figure 6.4: Energy deposition spectrum of the decay of 5×10^4 ^{210}Po placed exactly at the rough surface of a $CaWO_4$ crystal. Five different spike heights h are simulated. Their width is fixed at 5 µm. Three different energy ranges are presented: 0-6000 keV (top), 0-200 keV (bottom, left) and 5000-5500 keV (bottom, right).

increases, the tail is suppressed. This happens because with greater height, the likelihood of ^{206}Pb nuclei interacting with the crystal increases, leading to more or all of its energy being deposited in the crystal.

Investigating the medium energy range, we see that the ^{206}Pb peak exhibits a right tail, although it is less prominent than the left one. This tail is likely from α particles that escape the detector after depositing just a share of their energy, whereas the complete energy of ^{206}Pb is deposited within the crystal. With increasing height of spikes the tail becomes more prominent. This is due to the increasing possibility that α particles interact with the rough detector surface.

The impact of surface roughness is also observable in the high energy range, including the α peak at ~ 5300 keV and the mixed (α + ^{206}Pb) peak at ~ 5400 keV. Despite a minor tail on the left side of the α peak, the key characteristic is the ratio between the two peaks. With increasing height, counts tend to shift from the α peak to the mixed peak. To explain the behavior of the tail and the ratio between the peaks, we can apply the same reasoning as for the tail on the left of the ^{206}Pb peak. In the right figure of Figure 6.5 we can see that the left tail is mainly due to the contributions of the particles α. However, energies higher than the peak α can only be reached if both ^{210}Po remnants interact with the crystal.

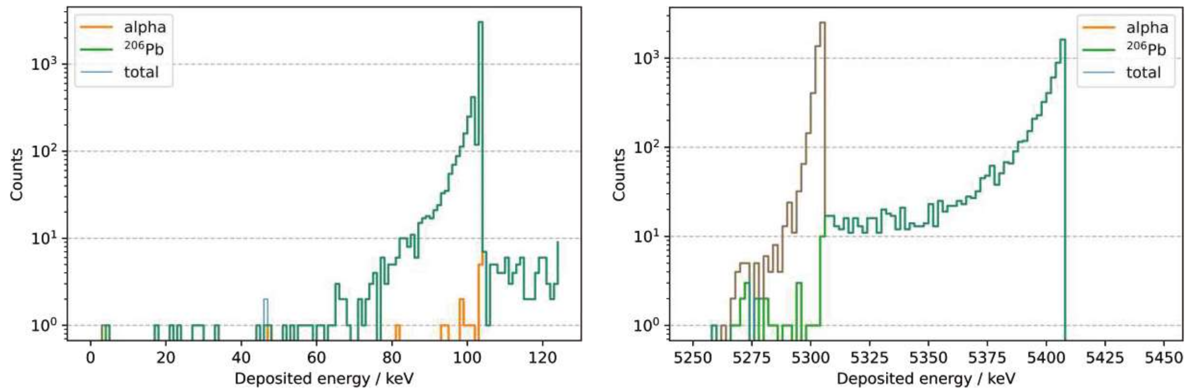

Figure 6.5: Energy deposition spectrum produced by the decay of ^{210}Po on the surface of a rough $CaWO_4$ crystal. The height and width of the spikes is set to 5 µm. The recorded hits are decomposed into the two decay products: the α particle and the ^{206}Pb nucleus. The sum of both hits per energy can exceed the total number of hits due to events where both products interact with the crystal. Depicted is the low energy range (left) including the ^{206}Pb peak and the high energy range (right) including the α and α + ^{206}Pb (mixed) peak.

6.2.2 Different Spike Forms

In the previous simulation, every spike had the same pyramid-like shape. This does not hold true in reality (see section 3.4). Different spike shapes can lead to different possibilities of interaction. To test the influence of spike shapes on the energy deposition spectrum, 5×10^4 ^{210}Po nuclei are placed on the surface of a rough patch with different spike forms (see also Figure 4.1): pyramid) the pyramid-shaped spike is the basic form and was used for the previous simulations. peak) The widths of the peak-shaped spikes follow $f(x;h) \propto 1/x$ where x represents the current height position. bump) The widths of the bump-shaped spikes follow $f(x;h) \propto x^2$ where x represents the current height position. The flat configuration has no rough surface and ^{210}Po nuclei are placed on the plain surface of the crystal. This is similar to a polished surface.

It can be seen that the bump and pyramid implementations are nearly indistinguishable. However, the peak shows some minor differences compared to the other two. The right tail of the ^{206}Pb peak shows a slightly different distribution of energy deposition. Compared to the pyramid and the bump implementation, the number of counts in the energy range between the ^{206}Pb and α peak is shifted towards lower energies. Based on the experience that this energy is deposited by the interaction of the α particles with the crystal, this implies a higher likelihood for α particles to escape the crystal, depositing only a small share of their energy. At the same time, the peak α increased. This does not contradict the aforementioned observation; rather, it suggests that the energy of the α particles is more likely to be measured as a total or that the particle escapes and does not deposit some energy.

The increase of the ^{206}Pb peak and the decrease of the mixed peak give the picture that a rough surface of peaks increases the probability that at least one of the decay remnants escapes the crystal.

As already seen in a previous study [13], a polished surface supports the generation of tails left of the ^{206}Pb and α peak. Furthermore, no mixed peak is observable because at least one of the decay products is escaping the surface immediately after the decay of ^{210}Po due to momentum conservation.

We examined various spike shapes and found that effects are noticeable; however, compared to the effect of the different spike heights previously discussed in subsection 6.2.1, the impact on the energy deposition spectrum is small. Moreover, three different spike shapes are tested; this leaves a large number of untested forms that might contribute in a different way. Exploring this would significantly expand the parameter space and would substantially increase the workload without a guaranteed significant effect on the energy deposition spectrum. However, it would be

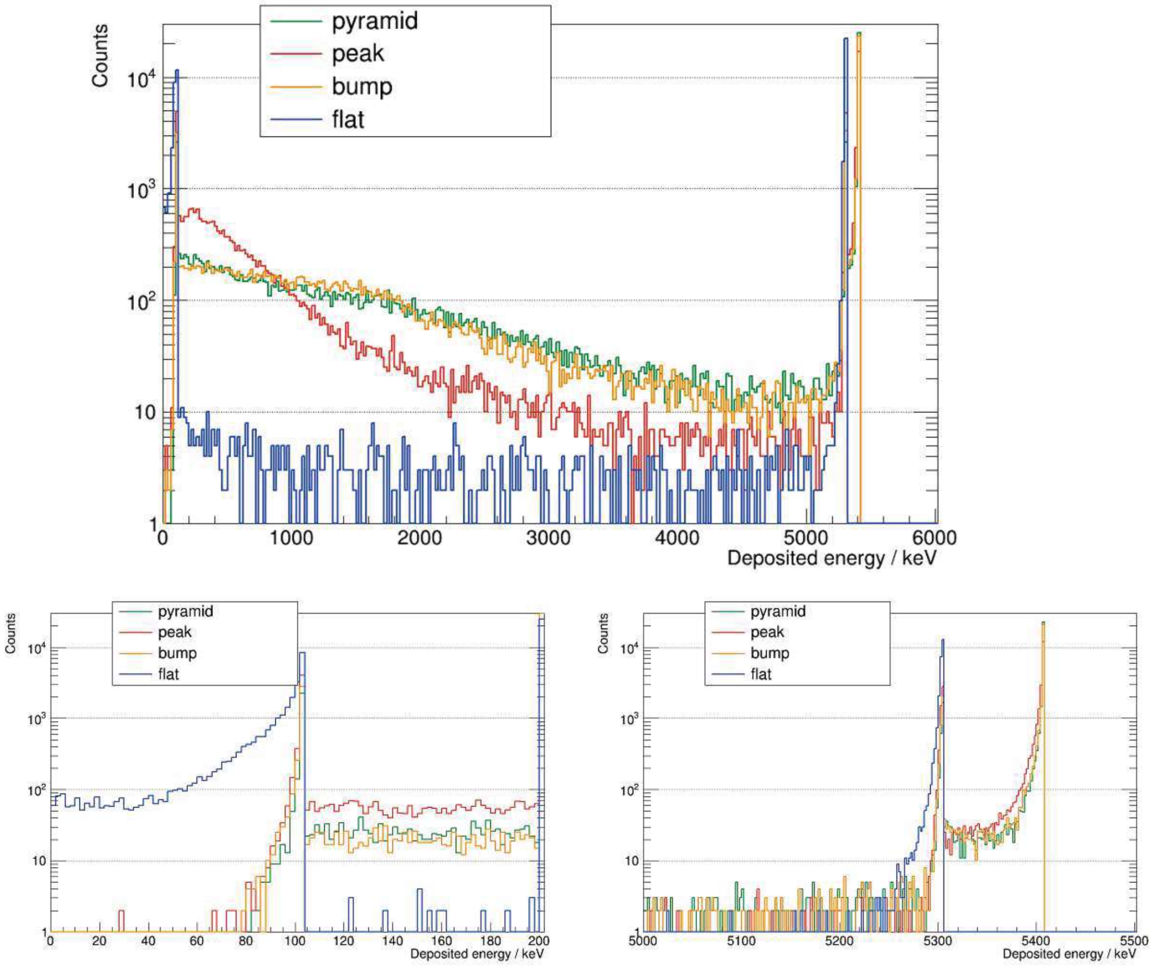

Figure 6.6: Energy deposition spectrum of 5×10^4 decaying ^{210}Po nuclei placed on a rough surface with different spike forms of 10 µm height and width and a flat surface of a $CaWO_4$ crystal. Three different energy ranges are presented: 0-6000 keV (top), 0-200 keV (bottom, left) and 5000-5500 keV (bottom, right).

interesting to test for effects automatically by setting up a testing suit using machine learning.

6.2.3 Simulation of a Rough Surface with ^{210}Po Contamination Using a Simulated Positioning Distribution

In subsection 6.1.2, a distribution of near-surface ^{210}Po due to exposure of a $CaWO_4$ crystal to ^{222}Rn is simulated and discussed. The simulation shows that ^{210}Po can become implanted more than 100 nm deep below the surface due to the multiple decays of the ^{222}Rn decay chain. This simulated distribution is now used to place ^{210}Po beneath a rough surface, yielding a more realistic model for simulation. The rough surface is simulated by spikes of 5 µm height and width.

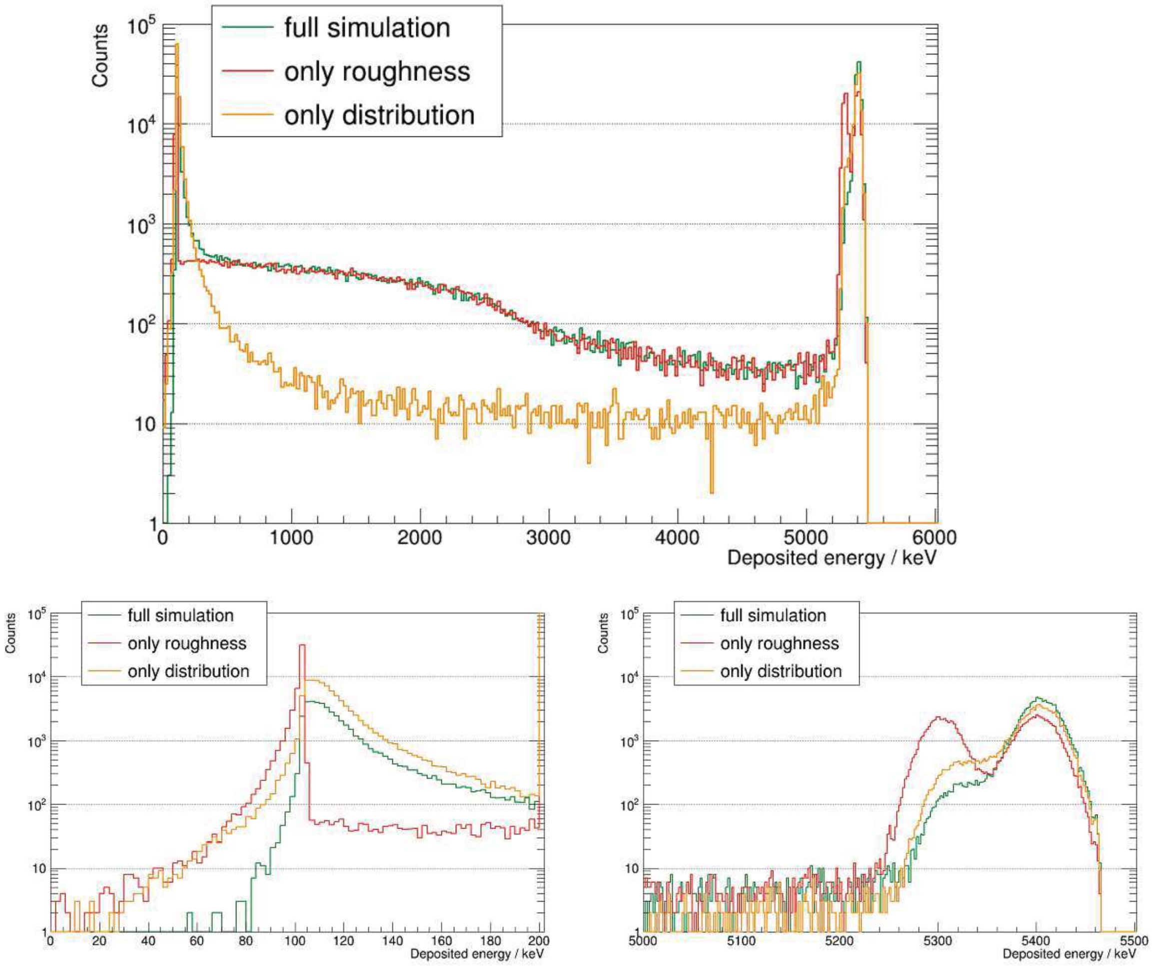

Figure 6.7: Energy deposition spectrum of the decay of 2×10^5 ^{210}Po placed below the rough surface of a $CaWO_4$ crystal. For the placement of ^{210}Po a distribution was used. The distribution represents a simulated distribution of ^{210}Po below the surface from exposure to ^{222}Rn. The spikes have a height and width of 5 µm. With CresstDS the detector resolution of TUM40 was applied to the data. Three different energy ranges are presented: 0-6000 keV (top), 0-200 keV (bottom, left) and 5000-5500 keV (bottom, right).

Figure Figure 6.7 shows three different energy deposition distributions: the histogram labeled "only roughness" represents the deposition spectrum due to the exact placement of the nuclei on the rough surface. The dataset "only distribution" depicts the energy deposition spectrum based solely on the distribution of ^{210}Po below a flat surface. The "full simulation" dataset combines both effects, showing the energy deposition spectrum influenced by the roughness and the distributed placement of ^{210}Po below the surface.

Interesting to see is that both the distribution and the roughness contribute distinct details to the spectrum. One significant difference is the ratio between the two high energy (α and mixed) peaks. While the roughness supports the generation of two peaks (see subsection 6.2.1), the distribution strongly increases the mixed peak with a tail that overlaps with part of the α peak. This occurs because ^{206}Pb can only travel a maximum of 60 nm, while the mean of the ^{210}Po distributions is at 28.53 nm, causing most of the ^{206}Pb nuclei to deposit all their energy within the crystal.

Another difference is the right tail of the ^{206}Pb peak caused by α particles that deposit only a small share of their kinetic energy. The ^{210}Po nuclei are placed in a layer from 0 to 100 nm, while alphas can move many µm in $CaWO_4$ before being stopped. Therefore, if they are placed in the vicinity of a flat surface, it is likely that they either escape, depositing nearly no energy, or are stopped inside the crystal and deposit all of their energy. This is different from the rough surface, where it is more likely that they deposit a larger share of their energy before escaping (see subsection 6.2.1 for a more detailed discussion on energy deposition due to a rough surface). However, the picture is slightly different for the right tails very close (energy range of $\sim 100 - 200$ keV) to the ^{206}Pb peak. Here, the counts for "only distribution" are much higher than for "only roughness". This is because of the minimal distance α particles have to travel through the crystal before they can escape. With the ^{210}Po distribution, the placement of the nuclei determines the minimum distance, whereas the rough surface alone always has a minimum distance of zero, which results in an abrupt decline right of the ^{206}Pb peak. In particular, neither effect alone is sufficient to suppress the left tail of the ^{206}Pb peak, which can extend to the ROI. However, both effects combined suppress the tail so that the counts in the ROI are not noticeable in the simulation.

Fit of Templates to Measurement Data

The "full simulation" of the energy deposition spectrum relies on two main assumptions: the actual rough surface can be approximated sufficiently well by the introduced spikes, which have heights and widths comparable to the crystal's roughness; and the distribution of the surface near ^{210}Po originated from the decay of ^{222}Rn on the surface, leading to the implantation of ^{210}Po into the crystal. Consequently, this is the first surface roughness template with ^{210}Po surface contamination that simulates a real-world scenario. This template has been fitted to the measured data of TUM40 using Bliss [12].

The fit results in Figure 6.8 show two phenomena: in the high energy range, the mixed (α + ^{206}Pb) peak is entirely covered by the surface template, while the template for ^{210}Po bulk contamination is suppressed. Additionally, the α peak is only slightly covered and the structure of two peaks adjacent peaks is not replicated. This finding implies that this surface template is either not correct or that important contributions are missing. It is possible that the ^{210}Po distribution beneath the surface is incorrect, potentially due to diffusion effects in the crystal, a more complex contamination source, or that small errors when simulating the whole decay chain add up and invalidate the distribution in the end.

However, in the low energy range the ^{206}Pb peak and its tails contribute to the spectrum and do not show any sign of contradiction, but also no recognizable feature.

As observed in this section and a previous study [13], in addition to surface roughness, the depth of contamination below the surface definitely has a non-negligible influence on the energy deposition spectrum. Hence, examining the contributions of the different layers below the surface to the energy deposition spectrum is essential and can give some insight into the correctness of the simulated template in this chapter.

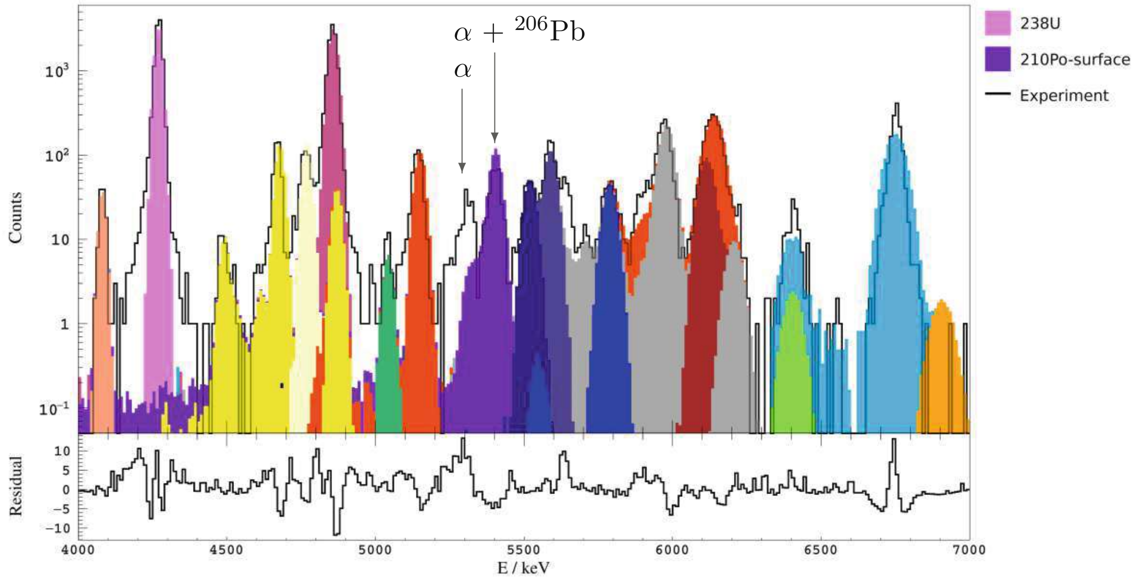

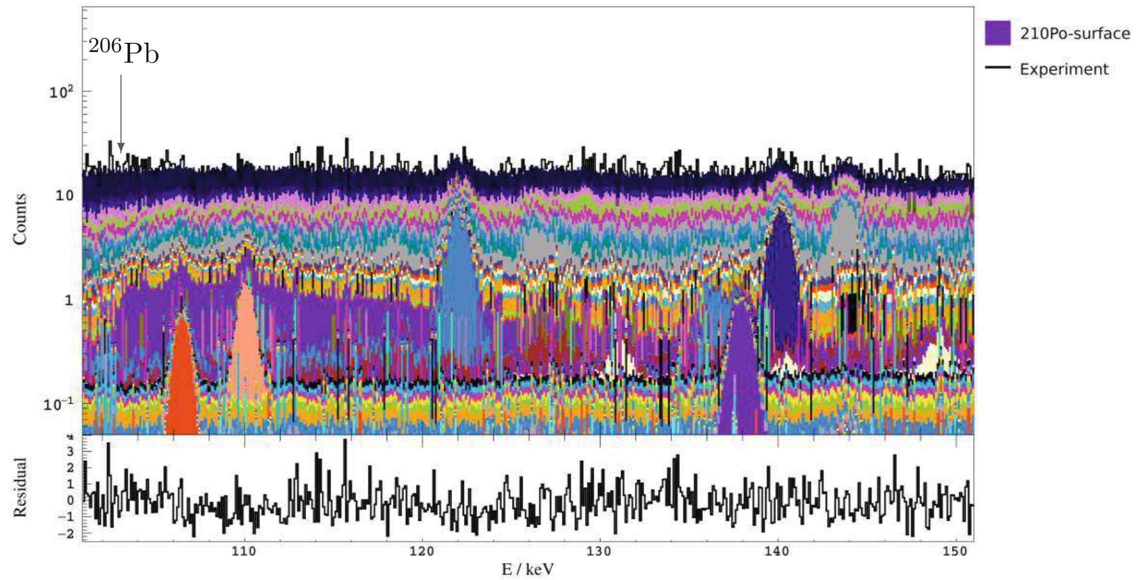

Figure 6.8: Fit of simulated energy deposition templates (colored, filled histograms) including a template for surface roughness and contamination by ^{210}Po, following a distribution, to the measured data (black, open histogram) of TUM40, done with Bliss [12, 60]. In the high energy range (top) the α and the α + ^{206}Pb peak can be seen. In the energy range from 100 to 150 keV (bottom) the energy of the ^{206}Pb peak ($\sim$ 103 keV) is marked and its energy deposition is colored in purple. For the comfort of the reader, those figures, including the full legend, are added in a bigger format to appendix: Figure A.5, Figure A.6.

6.2.4 Contribution of Contaminated Layers

In the previous section, surface templates were generated based on a rough surface by simulating spikes in the range of µm, along with a simulated distribution of ^{210}Po below the surface to represent realistic surface contamination. Now, a new approach is used to investigate the effect of the depth of contamination implantation in a rough surface on the energy deposition spectrum. Five layers of contamination are modelled at different depths, each having a thickness of 1 nm. A total of 5×10^4 ^{210}Po nuclei are evenly distributed within the layer and their subsequent decay is simulated. The spikes of the rough surface have a height and width of 5 µm.

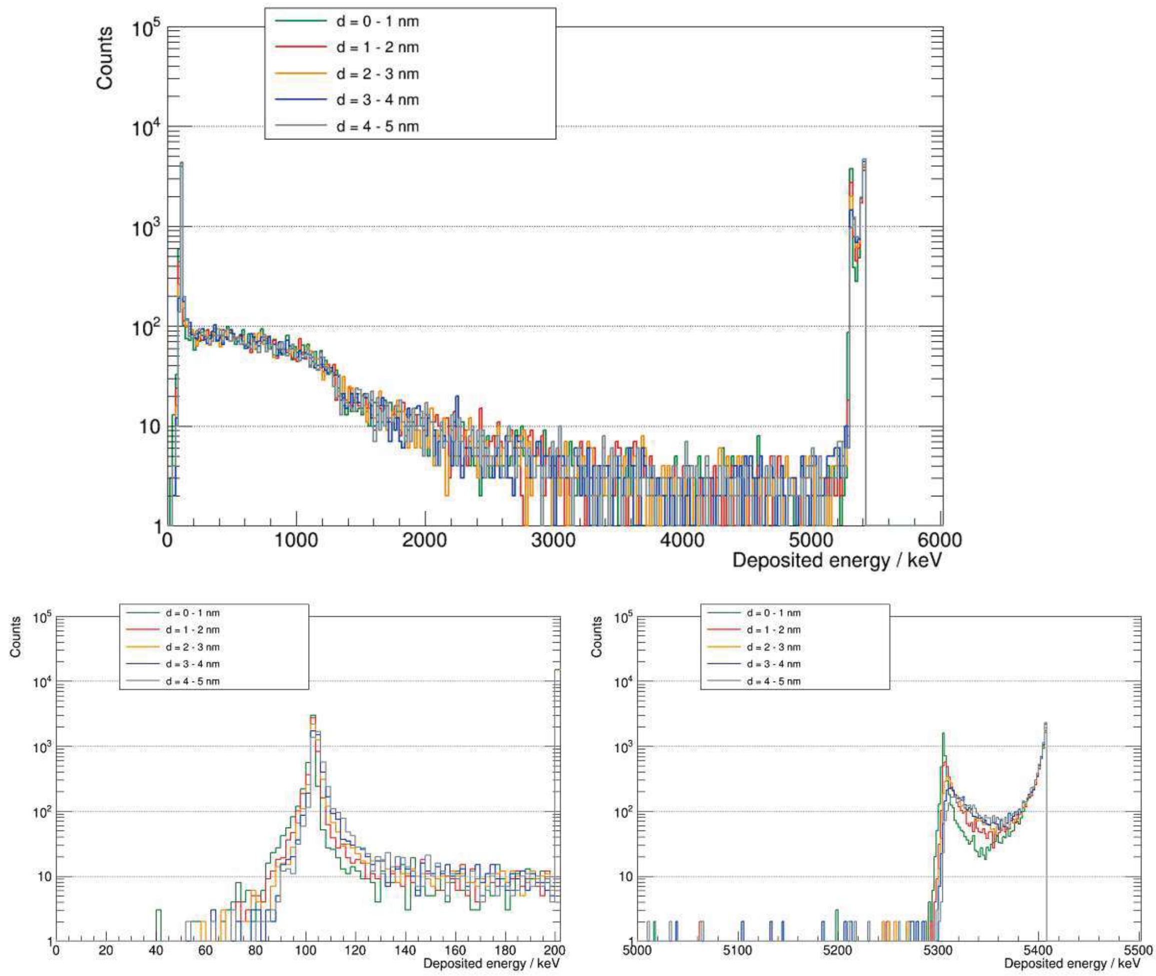

Figure 6.9: Energy deposition spectrum of the decay of 5×10^4 ^{210}Po placed in different layers withing the depth d below the rough surface of a $CaWO_4$ crystal. Inside the layers the ^{210}Po are uniformly distributed. The spikes have a height and width of 5 µm. Five different layers are simulated. Three different energy ranges are presented: 0-6000 keV (top), 0-200 keV (bottom, left) and 5000-5500 keV (bottom, right).

Only the first few nm are simulated because they show to have the most influence on the energy deposition spectrum. Figure 6.9 shows that as the layer depth increases, the counts from the α peak are shifted to the mixed (α + ^{206}Pb) peak while the rest of the energy deposition spectrum remains mostly unchanged across all five simulations. This is because the ^{206}Pb nuclei are stopped within the range of nm while the α particles can travel µm, therefore, the small shift of ^{210}Po below the surface affects the ^{206}Pb nuclei a lot compared to the α particles. Already a change in depth by 5 nm results in approximately a seven-fold change in the maximal height of the α peak. To reconstruct the α peak in the measured data from the decay of ^{210}Po, only the top layers can contribute.

Fit of Templates to Measurement Data

To obtain a precise fit, all five simulated surface templates discussed in subsection 6.2.4 are fitted to the measured energy deposition spectrum of TUM40 using Bliss. This introduces more free parameters that the fitting procedure can use to get the most accurate coverage of the peak at $\sim 5300\,\mathrm{keV}$.

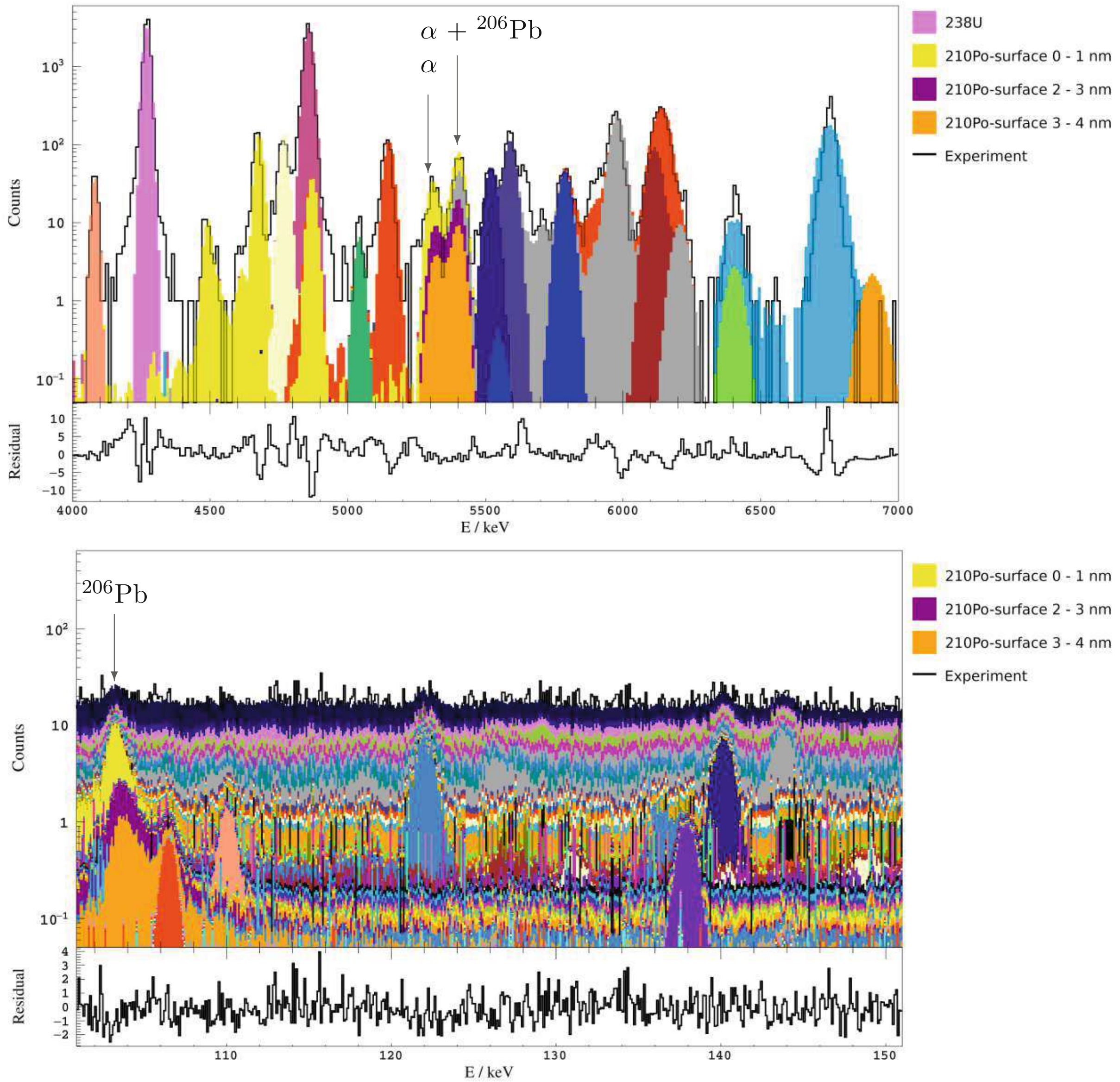

Figure 6.10: Simulated spectra caused by α-decaying bulk- and surface-contaminants (colored, filled histograms) fitted [12, 66] to experimental data (black, open histogram) of CRESST's TUM40 detector [84] using Bliss. Several templates for surface roughness contamination are modelled by uniformly placing ^{210}Po nuclei in different 1 nm thick layers shifted to different depths in the range of nm below the rough crystal surface. Three layers from 0 to 1 nm, 2 to 3 nm and 3 to 4 nm are visible.
Two different energy ranges, one from 4000 to 7000 keV (top) and one from 100 to 150 keV (bottom) are shown. For the comfort of the reader, those figures, including the full legend, are added in a bigger format to appendix: Figure A.7, Figure A.8.

The results of the fit in Figure 6.10 show that only three of the surface layer templates provided are used to fit the α and the mixed (α + ^{206}Pb) peak. This successfully recreates the feature of two adjacent but distinct peaks. However, some notable features are observed: For fitting both peaks, the layers $d = 0 - 1\,\mathrm{nm}, 2 - 3\,\mathrm{nm}$ and $3 - 4\,\mathrm{nm}$ were used, omitting $d = 1 - 2\,\mathrm{nm}$. It is possible that the differences between neighbouring layers were so marginal that the contributions of the excluded layer were compensated for by the others. Another observation is that the gap between the two peaks is not as deep as in the actual measured data. This could be due to several reasons, including the low statistics of the measurement data or the fact that the simulated templates are based on an approximation of the real surface of the crystal. A third observation is the missing coverage of the leftmost part of the α peak. Again, this may be because the simulation is just an approximation. The most significant feature is found in the lower energy region when examining the energy range of the expected ^{206}Pb peak. At approximately 103 keV, the energy deposited just by the ^{206}Pb nuclei is evident. A small peak can be seen in the stacked deposition spectrum of all contributions. This bump is in contradiction to the background measured by CRESST.

This fitting result indicates that a contribution mainly from surface near (< 5 nm) ^{210}Po is expected to show as a minor bump at approximately 103 keV in the measurement data. However, it is important to note that the number of counts contributed by the surface near ^{210}Po at this energy level is low and that the peak could potentially be hidden due to low statistics.

6.2.5 Simulation of Contaminated External Rough Surface Facing the Detector

In the previous part, two different internal surface contamination distributions of ^{210}Po were studied and associated energy deposition templates were fitted to the TUM40 data with Bliss. The fits can either not cover the α peak at ~ 5300 keV sufficiently accurate or cover it but introduce a contradiction to the measured background data. This raises the idea that other external surface sources can contribute to the spectrum. To test this hypothesis, a new simulation set-up is built.

The new simulation setup includes two $CaWO_4$ crystals facing each other with a distance of ~ 0.5 cm. Both can have a rough or flat surface. One is the target, representing the phonon detector, and one is the source, representing an other object, for instance the holding sticks (see section 3.3) which are out of $CaWO_4$ too [60]. 2×10^5 ^{210}Po nuclei are placed below the rough surface of the source facing the target, following the simulated distribution discussed in subsection 6.1.2. The roughness of the target and the source are represented by spikes with height and width of 5 µm.

In Figure 6.11 the new simulated energy deposition spectrum, from now on called "external contribution", is compared with the previously simulated spectrum, now called "internal contribution" of ^{210}Po placed below the rough surface of the target crystal following the previously simulated ^{210}Po spectrum. Clear differences can be seen.

The internal contribution has two visible peaks in the high energy range, the α and mixed ($\alpha +$ ^{206}Pb) peak, but the external contribution only has the α peak. This is because it is highly unlikely that both decay remnants, the ^{206}Pb nuclei and the α particle, escape the surface of the external source and reach the detector without depositing some energy, and therefore the mixed peak is not present. Actually, the sharp drop in counts for higher energies indicates that it is unlikely that both decay products escape and hit the detector. Furthermore, the external contribution has a tail left of the α peak. This comes mainly from α particles that escape the source while depositing a small share of their energy and depositing the rest within the target.

However, from $\sim 110 - 4000$ keV almost no energy was deposited. This is surprising because this suggests that α particles that deposit at least ~ 1300 keV of their energy inside the source when escaping do not deposit the rest of their energy inside the target volume. It could be that when entering the target volume, surface near atoms get excited, which later radiate most of their energy away. Then these α particles would contribute to the increase in counts near the lower end of the energy spectrum. This must be further investigated.

At the lowest energy range, the internal contribution shows the ^{206}Pb peak at approximately 103 keV, while the external contribution has a Compton-like spectrum with a drop in counts to zero at the energy according to the ^{206}Pb peak. This sharp edge at ~ 103 keV indicates that

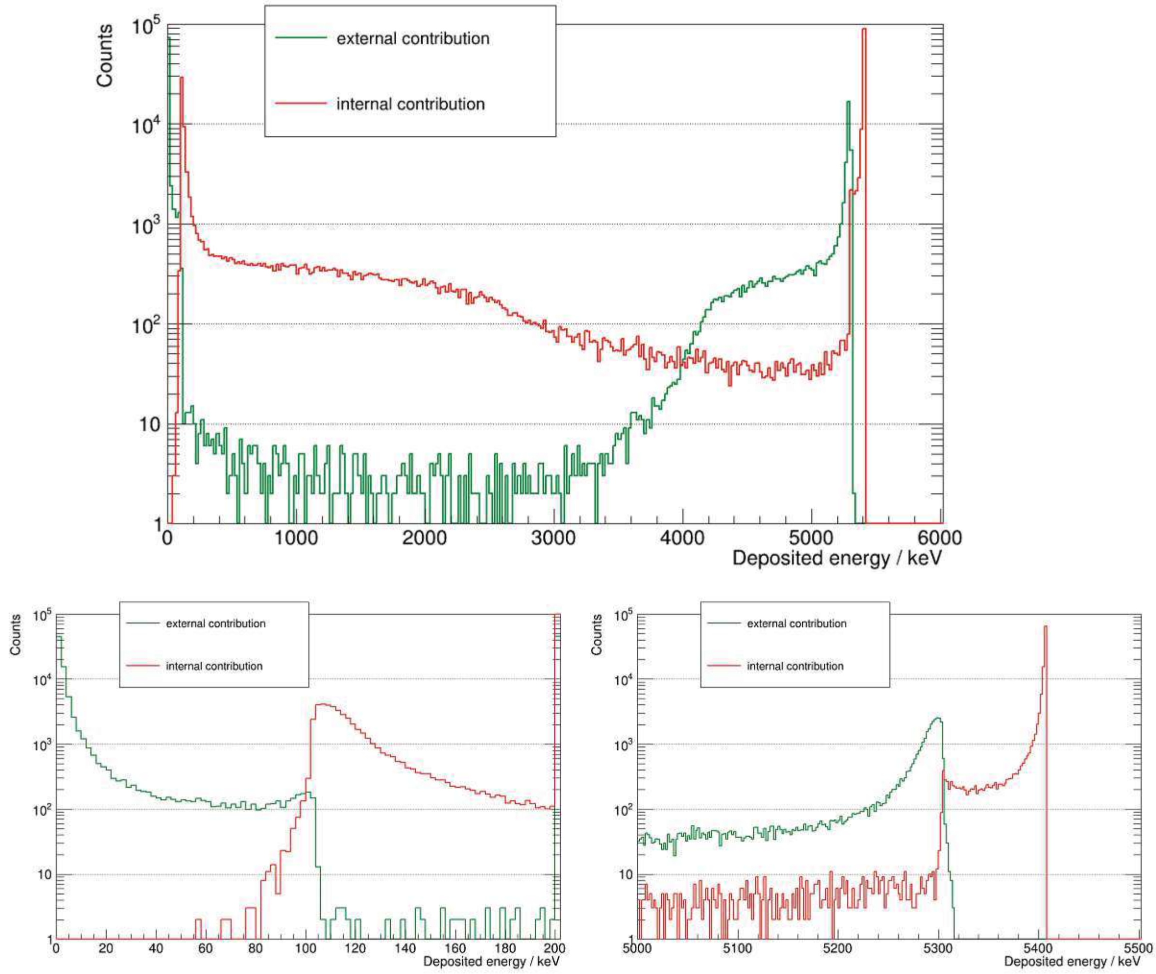

Figure 6.11: Comparison of the energy deposition spectra of ^{210}Po placed below the surface of an external source (labeled external contribution) and the target crystal (labeled internal contribution) separately, following a simulated distribution based on the ^{222}Rn decay chain. Both, the external source and the target crystal are out of $CaWO_4$ and have a roughness represented by 5 µm high and wide spikes. The contaminated and roughened surface of the source and the target are facing each other with a distance of approximately 0.5 cm. Three different energy ranges are presented: 0-6000 keV (top), 0-200 keV (bottom, left) and 5000-5500 keV (bottom, right).

^{206}Pb significantly contributes to this part of the spectrum. Lower energies than 103 keV can be achieved by ^{206}Pb depositing a share of their energy inside the source before escaping and hitting the target. In addition, some energy can be radiated away by excited atoms near the surface.

To investigate the steep increase in counts as the deposited energy decreases, the simulated energy deposition spectrum is decomposed into the two contributing remnants of the ^{210}Po decay (see Figure 6.12). It can be observed that in the energy range from $\sim 10 - 105$ keV, ^{206}Pb is the main type of contributory hits. However, below $\sim$ 10 keV α particles become the leading type of contribution and their counts further increase toward lower deposited energies. The last bin shows a drop in the contributions counts of ^{206}Pb; however, this may be a feature of the simulation, as we are in an energy range where the physical model could fail. The full energy range shows that for energies higher than $\sim$ 103 keV the contribution is dominated by α particles alone.

We have seen that an external source can result in a different energy deposition distribution in the target than an internal one. This simulation was done for two rough surfaces. Now, using the same simulation setup but different combinations of surfaces, the influence of surface

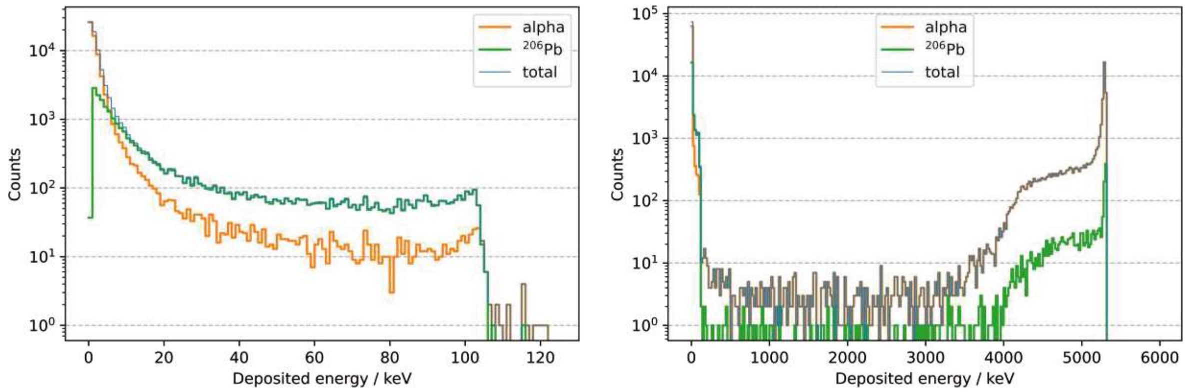

Figure 6.12: Energy deposition spectrum produced by the decay of ^{210}Po below the rough surface of an external source facing a rough detector crystal. Both volumes are $CaWO_4$ crystals. The placement of ^{210}Po follows a simulated distribution below the surface based on the ^{222}Rn decay chain. The height and width of the spikes is set to 5 µm. The recorded hits are decomposed into the two decay products: the α particle and the ^{206}Pb nucleus. The sum of both hits per energy can exceed the total number of hits due to events where both products interact with the crystal. Depicted is the low energy range (left) including the ^{206}Pb peak and the high energy range (right) including the α and mixed peak. The height of the first bin of the ^{206}Pb data (green, left) is likely to be a characteristic of the simulation and to be incorrect. The sharp drop in counts indicates a change of physics model.

roughness on the energy deposition spectrum is tested. The following different combinations are simulated, while "rough" is linked to a rough surface with spikes of height and width of 5 µm and "flat" represents a polished surface: 1) rough source, rough target; 2) rough source, flat target; 3) flat source, rough target; 4) flat source, flat target.

Figure 6.13 shows that the surface of the target crystal plays a subordinated role, no clear differences are observable. In contrast, the surface of the source significantly influences the energy deposition spectrum measured in the target. The most prominent characteristic is the left tail of the α peak. A source with a flat surface shows a single distinct peak; however , the energy deposition spectrum of a rough surface exhibits a tail left of the α peak, extending approximately to 4000 keV. Additionally, the counts of the spectrum in the low energy range are slightly shifted downward to lower energies, resulting in a reduction of counts above ~ 5 keV and an increase below this threshold. It appears that an external rough surface can contribute slightly more to the low energy background including the ROI than a polished one.

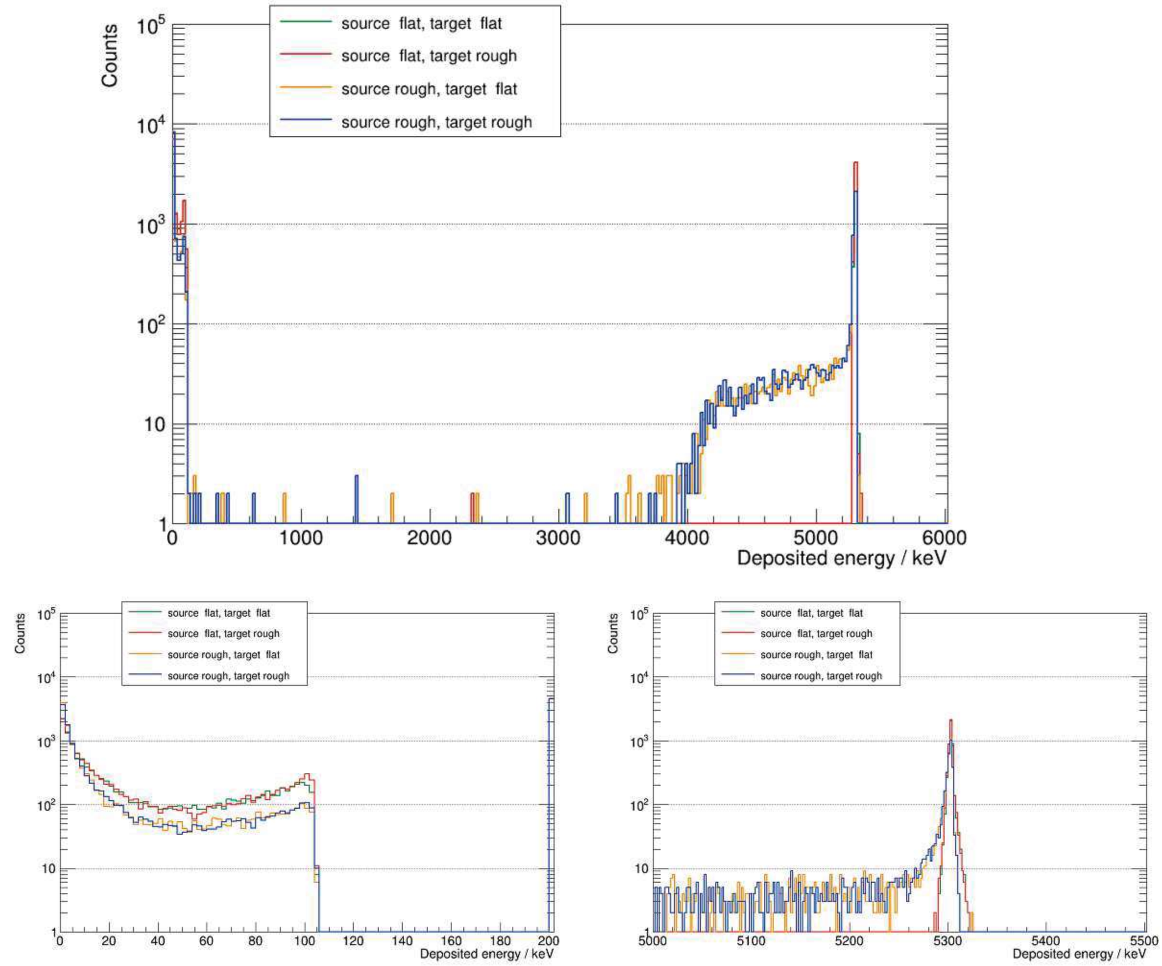

Figure 6.13: Energy deposition spectra of ^{210}Po uniformly placed in a 10 nm thick layer below the surface of an external rough surface facing the target crystal with a distance of ~ 0.5 cm. Both, the external source and the target crystal are out of $CaWO_4$ and are either polished or have a roughness represented by 5 µm high and wide spikes. Three different energy ranges are presented: 0-6000 keV (top), 0-200 keV (bottom, left) and 5000-5500 keV (bottom, right).

Fit of Templates to Measurement Data

The surface model is generated by simulating a ^{210}Po contamination and the roughness of an external $CaWO_4$ crystal, positioned at approximately 1 cm from the TUM40 photon detector. In the actual detector setup, although no other crystal faces the phonon detector as in the simulation, the crystal holders do have a direct line of sight to the detector crystal. This simulation configuration serves as an initial test to determine the relevance of external contamination, including surface roughness. The resulting template from the simulation is then matched to the TUM40 measurement data using Bliss [12].

The surface template is created by simulating a ^{210}Po contamination and roughness of an external crystal of $CaWO_4$ facing the TUM40 photon detector with a distance of ~ 0.5 cm. Although in the TUM40 module no other crystal is facing the phonon detector as in simulation, there are crystal holders within a direct line of sight to the detector crystal. The simulation setup used is a first test if an external contamination of a rough surface is of interest. The simulated template is fitted to the TUM40 measurement data using Bliss [12].

Three different energy ranges seen in Figure 6.14 are noteworthy. In the upper figure, both the α peak and the mixed peak can be observed. However, the mixed peak is only covered by the simulation of bulk contamination of ^{210}Po inside the target crystal while the α peak is only covered by the template representing the external contribution from a contaminated, rough surface. Between these peaks, a well-defined gap can be observed. Furthermore, the α peak is nearly entirely covered, including also its leftmost side. It should be noted that this surface template contributes to the entire spectrum of $\sim 4000 - 5300\,\mathrm{keV}$. All these observations are consistent with data and suggest that the peak at $\sim 5300\,\mathrm{keV}$ can partially originate from an external rough surface.

The figure in the middle illustrates the energy range from 100 to 150 keV, which includes the energy of ^{206}Pb after the decay of ^{210}Po. Within this energy range, the surface template contributes marginally; unlike the previous fit (see Figure 6.10) no peak at $\sim 103\,\mathrm{keV}$ can be observed.

Compared to the previous fits, this surface template significantly contributes to lower energies, as seen in the lower figure. This causes a general increase in the fitted spectrum; however, the low energetic increase is small enough to not conflict with the measurement data.

In this section, we demonstrated that a rough surface with external contamination produces an energy deposition spectrum with distinct characteristics compared to a polished surface. Additionally, the generated spectrum aligns well with the measured data of TUM40. It should be noted that external roughness significantly contributes to the lower energy range and can heavily influence the background data within the ROI. Even though surface contamination of the phonon detector is anticipated, external surface contamination alone can explain the α peak without contradicting the data. This indicates that an external contribution is significant and cannot be overlooked.

This section demonstrated that an external contaminated rough surface produces an energy deposition spectrum within the target crystal that fits well to the measured data of TUM40. I want to point out that an external roughness significantly contributes to the lowest energy range and can heavily influence the background data within the ROI. Although surface contamination of the phonon detector is expected, already external surface contamination alone can explain the observed α peak without contradicting the data. This indicates that an external contribution is significant and should not be neglected.

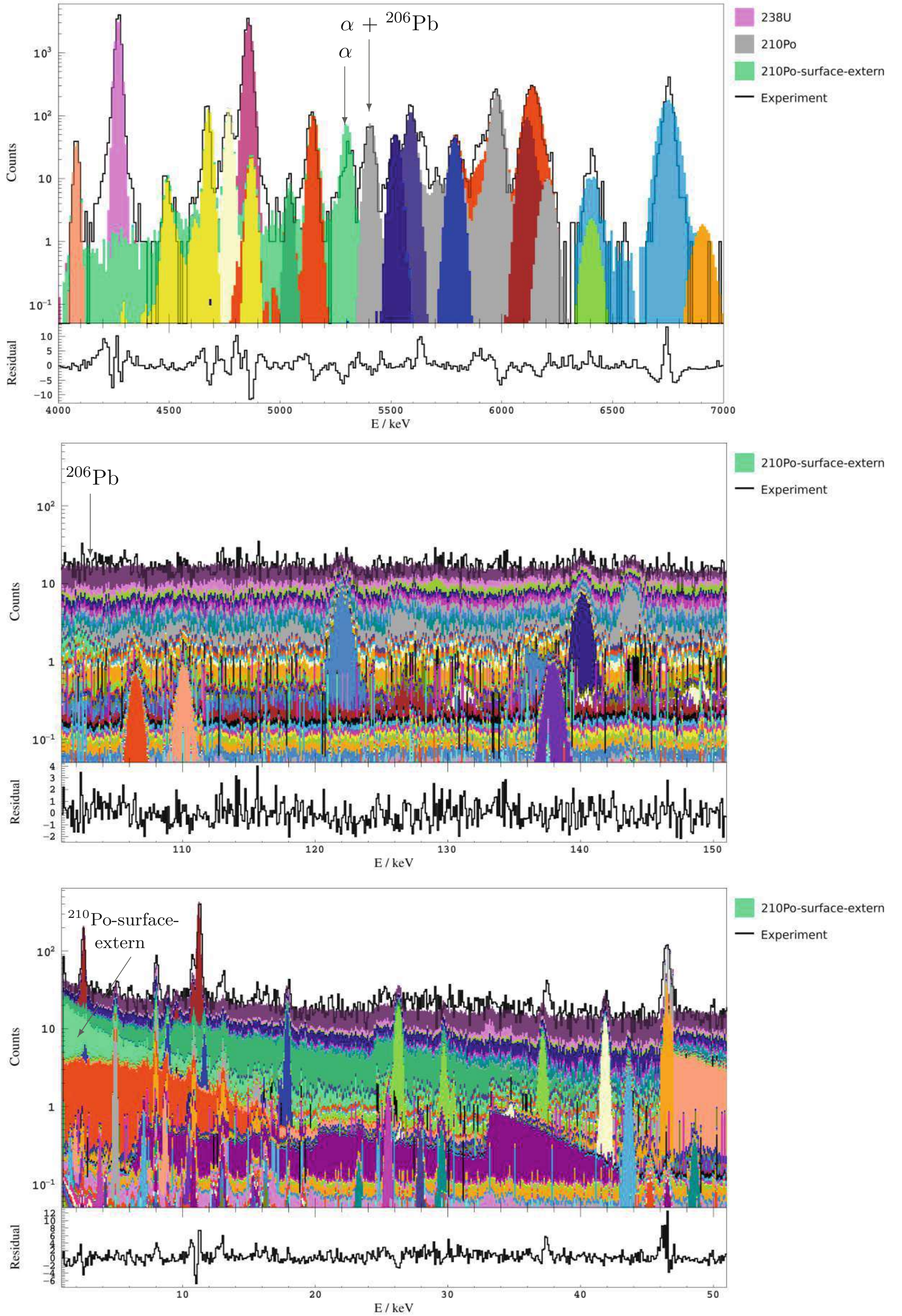

Figure 6.14: Simulated spectra caused by α-decaying bulk- and surface contamination (colored, filled histograms) fitted [12, 66] to experimental data (black, open histogram) of CRESST's TUM40 detector [84]. The surface contamination of ^{210}Po is placed below the rough surface of an external crystal, following a distribution based on the ^{212}Rn decay chain. The rough, contaminated surface is facing the detector with a distance of ~ 1 cm. Three different energy ranges, one from 4000 - 7000 keV (top) showing different peaks from α particles, one from 100 to 150 keV (mid) including the ^{206}Pb edge from the surface template and one from 1 to 50 keV (bottom) including part of the ROI are presented. For the comfort of the reader, those figures, including the full legend, are added in a bigger format to appendix: Figure A.9, Figure A.10, Figure A.11.

6.3 Simulation of a Potential Surface Contamination by ^{238}U

So far, only the issue of ^{210}Po surface contamination is addressed; nonetheless, ^{238}U is of interest too. As described in subsection 4.4.1, the surface of the TUM40 crystal is diffused. The surface may become contaminated with radionuclides such as ^{238}U or ^{234}U during the diffusion procedure. Another indication of a potential surface contamination on the crystal is the remaining uncovered tail next to the ^{238}U peak observed in the high-energy fit in Figure 5.1. This potential contamination, and a potential contribution of an external contaminated surface is investigated in the following.

6.3.1 Simulation of Internal and External Contribution of ^{238}U to the Energy Deposition Spectrum

For generating a ^{238}U distribution the same approach as for ^{210}Po can not be used due to the limited understanding of the dynamics of ^{238}U implantation into the crystal. Thus, a simplified distribution was generated by simulating three contaminated layers with a thickness of 5 nm for each below the surface of the $CaWO_4$ target crystal. Figure 6.15 shows the energy deposition spectrum of these contaminated layers. The rough surface is simulated by spikes with a height and width of 5 µm. For each spectrum, 5×10^4 ^{238}U nuclei are uniformly placed within the corresponding layer.

^{238}U is an α decaying nuclide with a Q-value of $Q = 4269.7\,\text{keV}$ and a half-life of $t_{1/2} = 4.4681 \times 10^9$ yrs. The kinetic energy of its decay products can vary due to various excitation states that the ^{234}Th nucleus can have afterward (see Figure B.2). The general picture of the energy deposition spectrum in Figure 6.15 (top) reflects the same observed phenomena as previously discussed for ^{210}Po. Two distinct peak areas are observed: one at low energies, corresponding to the energy deposition of ^{234} Th, and another at high energies, corresponding to the energy deposition of the α particle, or both combined. The intermediate distribution shows the step-like decline right next to the low-energy peak. Upon closer examination of the low energy peak, sub-peaks become apparent. This is due to the aforementioned different excitation states that the ^{234}Th nucleus can have after the ^{238}U decay. Multiple sub-peaks are also visible at the high energy range induced by the same effect also influencing the kinetic energy of the α particle; however, the peak at highest energy is a mixed peak, with contributions from both the α particle and the ^{234}Th nuclide.

These three layers are chosen because any ^{238}U contamination cause by the diffusing procedure is expected to be very close to the surface. Furthermore, the first nm below the surface have the most influence on the shape of the energy deposition distribution.

In Figure 6.16, two energy deposition spectra from ^{238}U placed as surface contamination in an external crystal and in the detector crystal are compared. Each spectrum involves a uniform distribution of 2×10^5 ^{238}U nuclei within a 15 nm thick layer below the rough surface of the corresponding $CaWO_4$ crystal. The roughness is represented by spikes of 5 µm height and width. The rough surfaces are facing each other with a distance of $\sim 0.5\,\text{cm}$. The spectrum corresponding to the external contribution shows similar features as discussed as already discussed for ^{210}Po. Yet again multiple peaks can be observed due to the different possible excitation states of ^{234}Th.

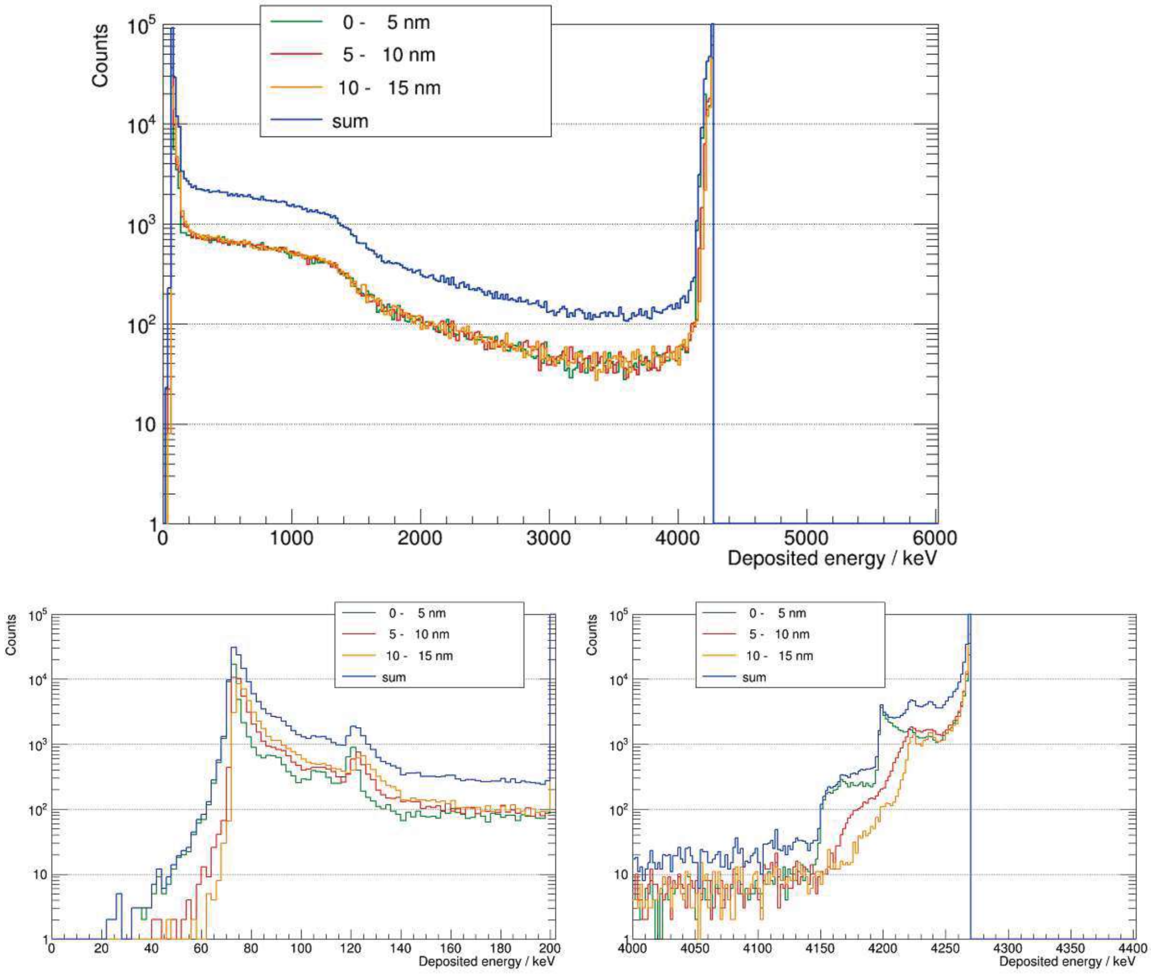

Figure 6.15: Energy deposition spectra of ^{238}U uniformly placed in three 5 nm thick layers below the rough surface of the detector crystal out of $CaWO_4$. The roughness is represented by 5 µm high and wide spikes. Three different energy ranges are presented: 0-6000 keV (top), 0-200 keV (bottom, left) and 4000-4400 keV (bottom, right).

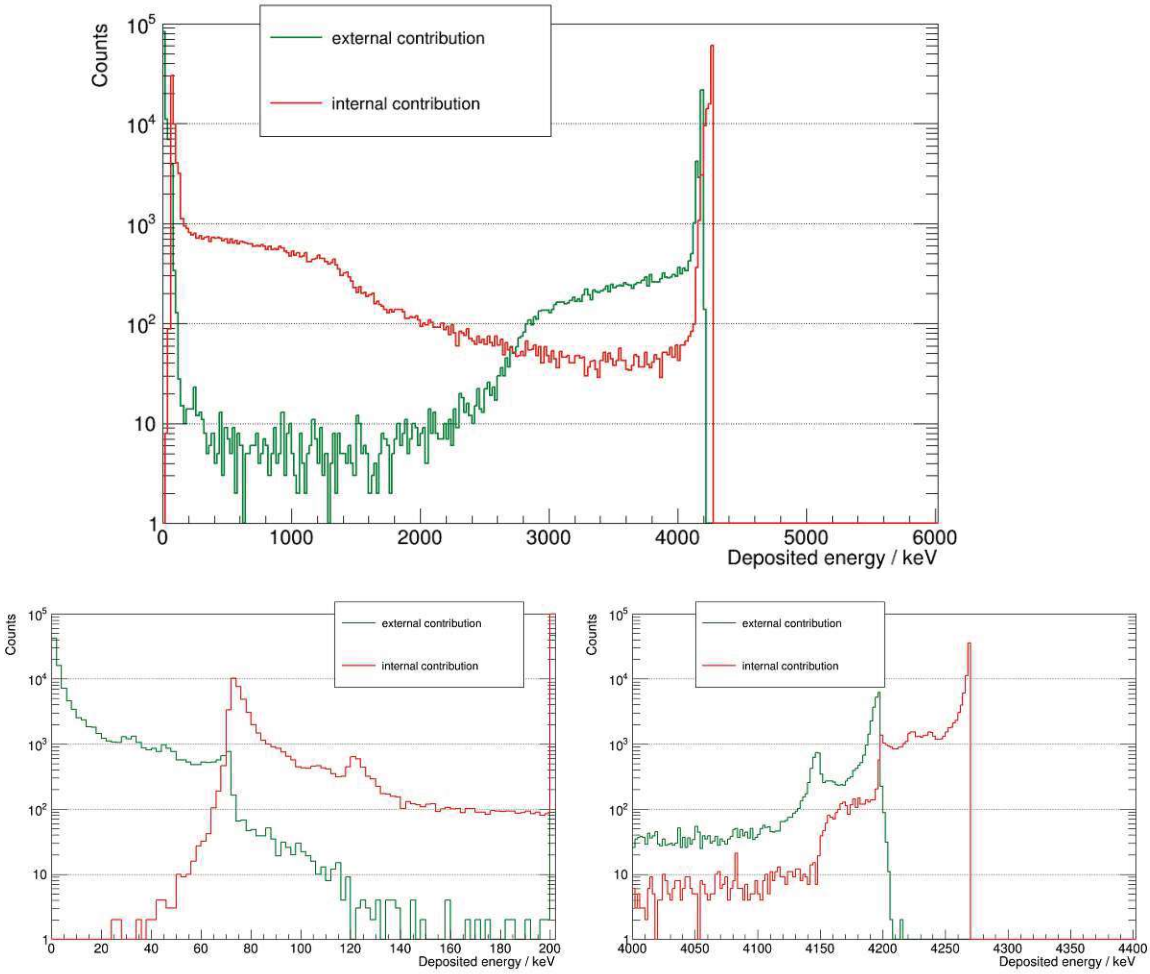

Figure 6.16: Energy deposition spectra from ^{238}U uniformly placed in 15 nm thick layers below the rough surface of an external and the target crystal. The contaminated surface of the external crystal is facing the target crystal with a distance of ~ 0.5 cm. The rough surfaces are represented by spikes with 5 µm height and width. Three different energy ranges are presented: 0-6000 keV (top), 0-200 keV (bottom, left) and 4000-4400 keV (bottom, right).

Fit of Templates to Measured Data

The in subsection 6.3.1 discussed four simulated templates, one for an external surface contribution from ^{238}U and three representing internal surface contributions each induced by a one layer of a certain depth below the surface, 0-5 nm, 5-10 nm and 10-15 nm, are fitted to the measurement data with Bliss. Using several templates for the internal surface contribution adds some free parameters the fit can adjust and get a better result. However, the final result must be consistent with real physics.

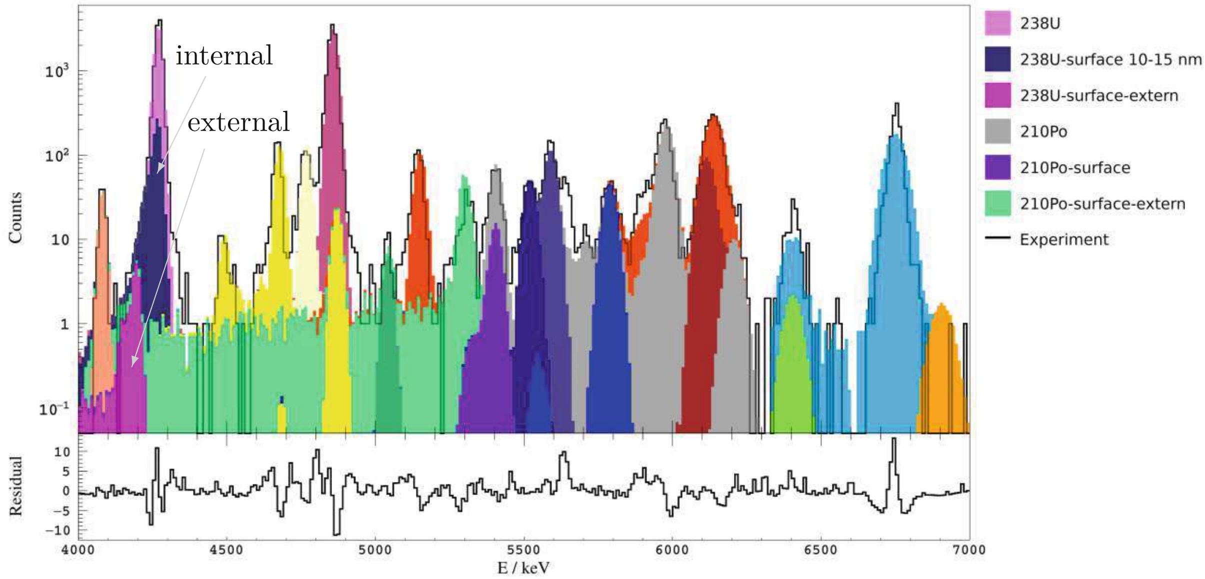

Figure 6.17: Simulated spectra caused by α-decaying bulk- and surface contamination (colored, filled histograms) fitted [12, 66] to experimental data (black, open histogram) of CRESST's TUM40 detector [84]. Surface contamination of ^{238}U is uniformly placed in a layer of 15 nm below the rough surface of the external crystal and in three layers from 0-5 nm, 5-10 nm and 10-15 nm below the rough surface of the detector crystal. All rough surfaces are represented by 5 µm high and wide spikes. For the comfort of the reader, the figure, including the full legend, is added in a bigger format to appendix: Figure A.12.

In Figure 6.17 we can observe that two of the four templates added were used to successfully cover the left tail of the ^{238}U peak: the contribution from an external contaminated surface and the contribution from the layer with ^{238} placed within a depth of $d = 10 - 15$ nm were used. Contamination confined to a layer starting at a depth of 10 nm but not closer to the surface should be considered non-physical. It is probable that the template generated by the external surface contribution is overfitting and thereby suppressing the outer two layers within 0-10 nm. An evaluation of the other energy ranges reveal no further discrepancies between the fitted templates and the measured data.

6.3.2 TUM40 Final Fit

Based on the findings outlined in this chapter, four templates of energy deposition induced by contamination of a rough surface are fitted to the data measured with the TUM40 crystal. The four templates are based on: 1) ^{210}Po nuclei placed below the rough surface of a $CaWO_4$ crystal facing the target crystal with a distance of ~ 0.5 cm. The placement of nuclei follows the simulated ^{210}Po distribution induced by the ^{222}Rn decay chain (see subsection 6.2.5). 2) ^{210}Po placed below the rough surface of a $CaWO_4$ detector crystal, also following the simulated ^{210}Po distribution (see subsection 6.2.3). 3) ^{238}U uniformly placed in a 15 nm thick layer below the rough surface of an external $CaWO_4$ crystal facing the target crystal with a distance of ~ 0.5 cm (see section 6.3). 4) ^{238}U uniformly distributed in a 15 nm thick layer below the rough surface of the $CaWO_4$ detector crystal (see section 6.3). The surface roughness of all templates is emulated by spikes of 5 µm height and width.

The top figure of Figure 6.18 shows, in comparison to Figure **??**, different contributions of simulated templates to the ^{238}U and α peak from ^{210}Po decay. The left tail of the ^{238}U peak from bulk contamination is covered only by a surface contamination of the target crystal. The energy deposition template of an external contaminated, rough surface by ^{238}U is suppressed. This results in two scenarios: either there is only a minimal contribution from an external rough surface contaminated by ^{238}U, or the differences of both surface ^{238}U nuclei templates are too negligible in this region, causing the external ^{238}U template to be suppressed and its actual contribution covered by other ^{238}U template.

However, both simulated ^{210}Po templates, accounting for the contribution of the internal and external surface, are fitted to the spectrum without adding any inconsistencies. Moreover, in the low energy region (middle figure) the external ^{210}Po contribution increases the counts towards lower energies. The figure in the bottom shows the combination of all simulated surface-induced contributions. It is evident that approximately below 100 keV, surface contamination, especially of a roughened surface facing the detector, is significant.

Including surface templates influences the scaling of the other templates in the fit. Some are directly affected, such as ^{226}Ra which is suppressed by $\sim 50\,\%$ when surface templates are included because of its overlap of the region of energy deposition with the one from surface templates. Others are indirectly influenced because of a secular equilibrium subchain. It can be seen that ^{220}Rn is reduced by $\sim 77\,\%$ although its energy deposition does not overlap in any way with the energy deposition from the surface templates. However, it is reduced because the whole secular equilibrium subchain ^{220}Rn decaying to ^{216}Po decaying to ^{212}Pb decaying to ^{208}Tl is suppressed by $\sim 77\%$. This can be because ^{212}Pb and ^{208}Tl overlap with surface templates in the energy range from $\sim 1 - 2000$ keV. However, most of the templates change less then 5 %. This direct and indirect influences make it hard to investigate the dependency between templates. To get a clear picture, the influence of the different templates should be further investigated.

Table 6.3: Comparison of reproduction values for TUM40 and TUM40 including surface contamination templates for the the energy ranges low (1-495 keV), medium (511-2800 keV) and high (4000-7000 keV) calculated with Bliss [12].

	low	**medium**	**high**
TUM40	99.03 %	85.61 %	97.24 %
TUM40 + surface	99.15 %	85.34 %	98.10 %

Table 6.4: Comparison of explainable percentage values for TUM40 and TUM40 including surface contamination templates for the the energy ranges low (1-495 keV), medium (511-2800 keV) and high (4000-7000 keV) calculated with Bliss [12].

	low	**medium**	**high**
TUM40	90.94 %	86.86 %	32.92 %
TUM40 + surface	91.08 %	87.16 %	33.49 %

Visually incorporating surface contamination in combination with surface roughness into the simulation improves the fit and therefore the understanding of the measurement. To quantify the fit's quality, two intuitive metrics are used. One, the covering percentage is the ratio of expected events as yielded from the fit to the events from the dataset. The second measure is the explainable percentage, which also takes into account the shape of the templates. For a detailed discussion of the measures used, see [12].

In Table 6.3 we can observe that the coverage slightly increases for the low energy range and decreases for the medium energy range, however in the high energy range the coverage increases by 0.86 %. Furthermore, all explainable percentage values in Table 6.4 are improving.

Again, the change for the highest energy range is the largest. These values support the visual impression that the addition of these templates improves the fit.

Table 6.5: Comparison of Surface activity based on simulated and fitted templates for TUM40 (see chapter 6), with bulk contamination projected on the surface. For transformation of bulk to surface activity the bulk activity was used to calculate the activity for a small layer. Two different thickness calculations are used: Bulk,Layer) accounts for the thickness of the placement layer of nuclei used in simulation. This results in the layer thickness values of 55 nm for ^{210}Po (this rounded value marks the 0.9-Quantile of the simulated ^{210}Po distribution) and 15 nm for ^{238}U. Bulk,Roughness) accounts for the height of the spikes and the layer thickness. The sum of the mean height of spikes (1.67 µm) and the layer thickness aforementioned in the previous point was used.

	^{210}**Po** [Bq/cm^2]	^{238}**U**[Bq/cm^2]
TUM40	$5.29 \pm 2.01 * 10^{-8}$	$4.08 \pm 0.31 * 10^{-7}$
$\mathrm{TUM40}_{\mathrm{Bulk,Layer}}$	$2.83 \pm 0.32 * 10^{-12}$	$2.69 \pm 0.02 * 10^{-11}$
$\mathrm{TUM40}_{\mathrm{Bulk,Roughness}}$	$8.83 \pm 0.99 * 10^{-11}$	$3.02 \pm 0.02 * 10^{-9}$

Table 6.6: Comparison of observed counts from ^{210}Po bulk contamination, ^{210}Po surface contamination, ^{210}Po surface contamination of an external surface, ^{238}U bulk contamination, ^{238}U surface contamination and ^{238}U surface contamination of an external surface from simulated and fitted templates for TUM40 after an exposure of 2792.51 kg d. Three different energy ranges are shown.

Energy Range	$^{210}\mathrm{Po}_{\mathrm{bulk}}$	$^{210}\mathrm{Po}_{\mathrm{surface}}$	$^{210}\mathrm{Po}_{\mathrm{extern}}$	$^{238}\mathrm{U}_{\mathrm{bulk}}$	$^{238}\mathrm{U}_{\mathrm{surface}}$	$^{238}\mathrm{U}_{\mathrm{extern}}$
4000 - 7000 keV	272	82	392	9513	598	-
501 - 2800 keV	-	27	-	-	205	-
1 - 500 keV	-	39	654	-	336	-

Finally, the scaling of the surface contamination templates fitted to the data can give surface activity values for the TUM40 crystal (see Table 6.6). To validate that these values indicate an accumulation of ^{210}Po and ^{238}U at the surface, the corresponding bulk activities are projected onto the surface. This is done by defining the thickness of the active surface layer. For that, two measures are used: One takes into account only the used placement of nuclei below the surface. For ^{210}Po this is 55 nm, which corresponds to the 0.9-quantile of the distribution ^{210}Po used for placing this nuclei below the surface. For ^{238}U 15 nm is chosen, which is the thickness of the placement layer used for the surface simulations of ^{238}U. A second one adds the mean height of the spikes used to simulate the rough surface to the placement layer thickness from point one. The mean height of the used roughness is 1.667 µm. The surface activity derived from the fit of the templates is clearly significantly higher than the bulk activity projected on the surface, suggesting a notable accumulation of ^{210}Po and ^{238}U on the surface of the TUM40 crystal.

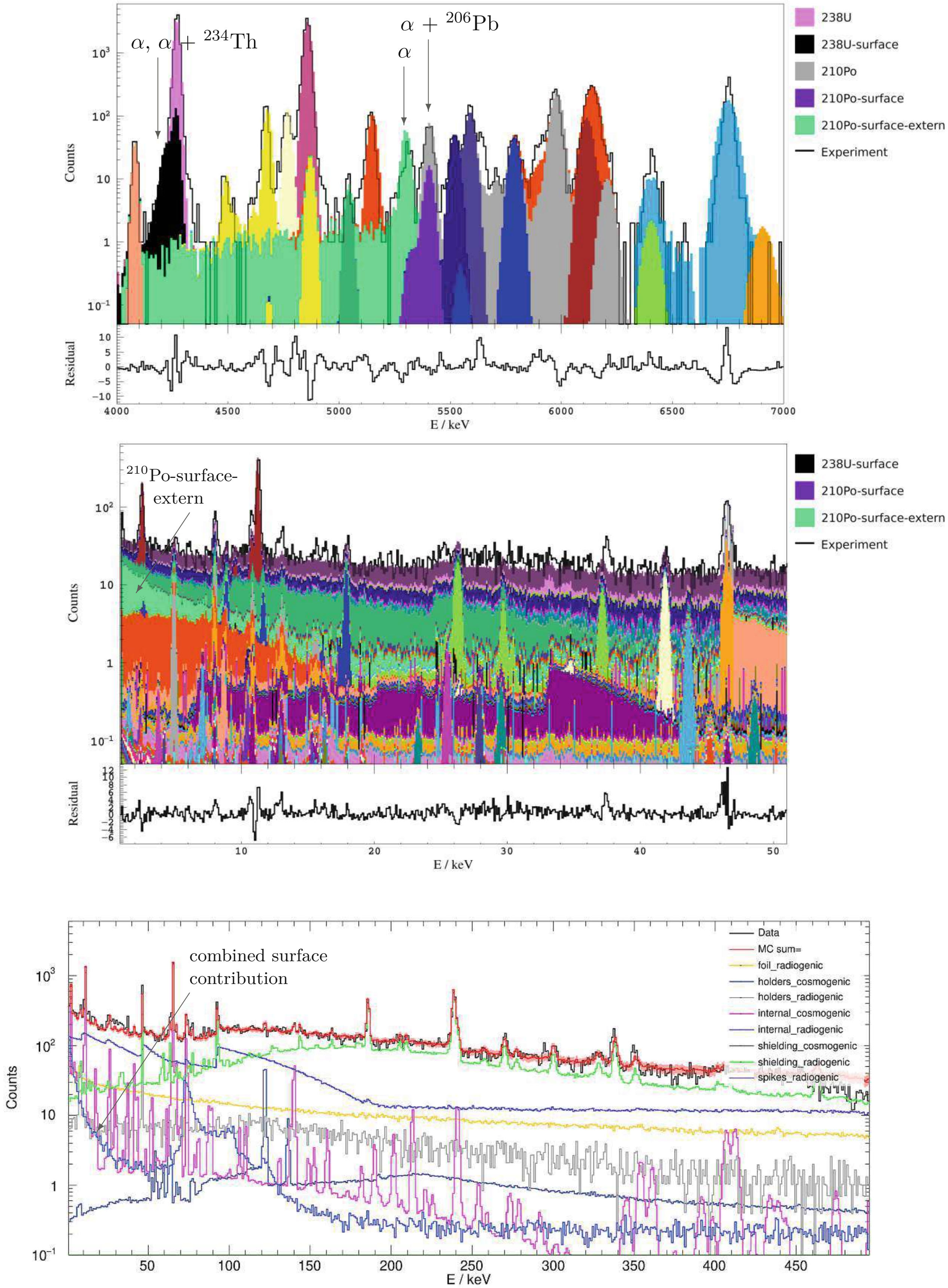

Figure 6.18: Simulated spectra caused by α-decaying bulk- and surface contamination (colored, filled histograms) fitted [12, 66] to experimental data (black, open histogram) of CRESST's TUM40 detector [84]. Four surface contamination energy deposition templates are added. Two for the nuclei ^{210}Po and ^{238}U. Each adding a surface contamination from an external rough surface facing the target detector with a distance of 0.5 cm and a surface contamination of the target crystal itself. ^{210}Po is placed below the rough surface following a simulated ^{210}Po distribution from the ^{222}Rn decay chain. ^{238}U is uniformly placed in a 15 nm thick layer below the rough surface. The rough surfaces are emulated by spikes of 5 µm height and width. The top and middle figure show the contribution of the single templates to the fitted spectrum. The bottom figure shows the contributions grouped to different sources for the lower energy range. For the comfort of the reader, those figures, including the full legend, are added in a bigger format to appendix : Figure A.13, Figure A.14 Figure A.15.

6.4 TUM93A

The previous section covered the development of surface contamination templates that include surface roughness and its contamination by ^{210}Po and ^{238}U nuclei. The same findings are now used to generate templates for the new TUM93A detector crystal, which is one of CRESSTs radiopurest crystals. As before, four templates are produced using the same parameters as those used for the final fit of TUM40 subsection 6.3.2. However, the resolution of DetectorA was applied to the simulated data with CresstDS, as the detector model of TUM93A is still under development. The four individual templates used to fit TUM93A are shown in Appendix B. The fit results without the four templates can be found in the Appendix: Figure A.19, Figure A.20 and Figure A.21.

Figure 6.19 shows the fit of the simulated templates to the measured spectrum of the detector crystal TUM93A by CRESST. In the high energy range (top figure), both external and internal ^{210}Po contaminated rough surfaces contribute. Internal surface contamination covers a large part of the peak induced by the combined α + ^{206}Pb energy deposition, as well as a part of the peak mainly induced by α particles from the decay of ^{210}Po alone. The energy deposition spectrum from an external ^{210}Po contaminated rough surface covers the rest of the aforementioned α peak and induces a tail that covers a large area. I want to point out that the visual discrepancy between this template covering a large area but the data showing nearly no counts may be due to the very low statistics. In the lower energy ranges (middle, bottom) an influence of external ^{210}Po surface contamination from $\sim 0.4 - 100\,\mathrm{keV}$ is also observable. Within the range from $\sim 0.4 - 10\,\mathrm{keV}$, its contribution to the spectrum increases significantly and becomes a crucial factor towards lower energies. Definitely this increase must be studied further.

Interestingly, both ^{238}U surface templates are suppressed by the fit; however, this can be due to low statistics. The total number of counts in the energy region $\sim 4200 - 4300\,\mathrm{keV}$ correlated with the ^{238}U is five, which is too low to draw any conclusions regarding surface contributions.

The final fitting result leaves some of the measured data uncovered. This arises because the TUM93A model is still under development, becoming more precise as more templates can be simulated and added. As a consequence, not all fitted templates are correctly scaled. For instance, ^{40}K shows a substantial contribution including one peak at $\sim 3.7\,\mathrm{keV}$, which is not observed in the data. This mismatch is due to the fitting process, which attempts to cover other contributions using this template. To prevent the fit from scaling the external ^{210}Po rough surface contamination template to unreasonable levels, a maximum limit was imposed, based on the previous TUM40 fit. Although the detector crystal and the detector module are different for TUM40 and TUM93A, they still share similarities like the holding sticks, the foil, etc. (see section 3.3). However, missing contributions to the TUM93A background model and the set of a maximum limit do not reduce the significance of the ^{210}Po surface contamination templates. The correctness of the fit is supported by the covering of the α peak from ^{210}Po decay at $\sim 5300\,\mathrm{keV}$.

Again, like for TUM40 the included surface templates influence the scaling of the other templates. However, no template in particular seems to be of particular interest. To get a clear picture, the dependency between the templates should be further investigated.

Table 6.7: Comparison of explainable percentage values for TUM93A and TUM93A including surface contamination templates for the the energy ranges low (0.9-9.9 keV), medium (0.4-900 keV) and high (4000-7000 keV) calculated with Bliss [12].

	low	**medium**	**high**
TUM93A	2.69 %	28.95 %	48.67 %
TUM93A + surface	4.38 %	29.82 %	93.67 %

Moreover, the calculated explainable percentage supports the improvement of the TUM93A background model by adding these surface templates (see Table 6.7). Especially in the high energy region this value is improved by 45 %.

Table 6.8: Comparison of Surface activity based on simulated and fitted templates for TUM93A (see chapter 6), with bulk contamination projected on the surface. For transformation of bulk to surface activity the bulk activity was used to calculate the activity for a small layer. Two different thickness calculations are used: Bulk,Layer) accounts for the thickness of the placement layer of nuclei used in simulation. This results in the layer thickness values of 55 nm for ^{210}Po. This rounded value marks the 0.9-quantile of the simulated ^{210}Po distribution. Bulk,Roughness) accounts for the height of the spikes and the layer thickness. The sum of the mean height of spikes (1.67 µm) and the layer thickness aforementioned in the previous point was used.

	^{210}Po [Bq/cm^2]	**^{238}U**[Bq/cm^2]
TUM93A	$2.21 \pm 0.69 * 10^{-7}$	-
TUM93A$_{\text{Bulk,Layer}}$	$1.46 \pm 0.21 * 10^{-11}$	$4.19 \pm 3.04 * 10^{-13}$
TUM93A$_{\text{Bulk,Roughness}}$	$4.57 \pm 0.67 * 10^{-10}$	$4.70 \pm 3.41 * 10^{-11}$

Table 6.9: Comparison of observed counts from ^{210}Po bulk contamination, ^{210}Po surface contamination, ^{210}Po surface contamination of an external surface, ^{238}U bulk contamination, ^{238}U surface contamination and ^{238}U surface contamination of an external surface from simulated and fitted templates for TUM93A after an exposure of 8.793 kg d. Two different energy ranges are shown.

Energy Range	^{210}Po$_{\text{bulk}}$	^{210}Po$_{\text{surface}}$	^{210}Po$_{\text{extern}}$	^{238}U$_{\text{bulk}}$	^{238}U$_{\text{surface}}$	^{238}U$_{\text{extern}}$
4000 - 7000 keV	89	46	311	9	-	-
0.4 - 900 keV	-	11	172	-	-	-

Based on the fit, the surface activity of ^{210}Po of TUM93A can be calculated. Again, the activity is compared with the fitted bulk activity projected to the surface using the same approach as discussed in the previous section. Table 6.9 shows that the fitted surface activity is many orders larger than the projected bulk surface activity. This is a clear indication of an accumulation of ^{210}Po on the surface of the TUM93A crystal. A surface activity of ^{238}U can not be calculated because the corresponding template was suppressed, probably due to low statistics.

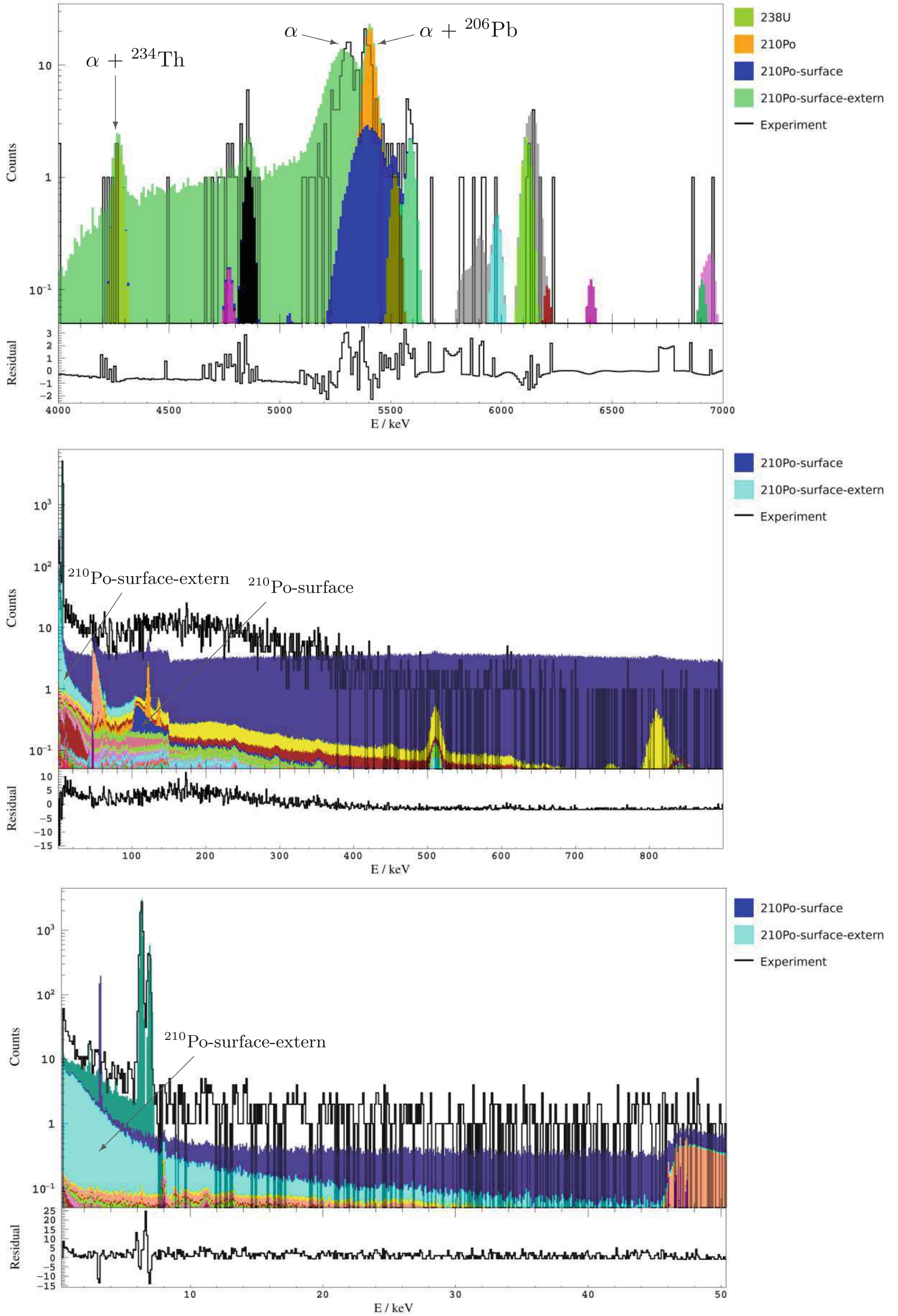

Figure 6.19: Simulated spectra caused by bulk- and surface contamination (colored, filled histograms) fitted [12, 66] to experimental data (black, open histogram) of CRESST's TUM93A detector. Four surface contamination energy deposition templates are added. Two for the nuclei ^{210}Po and ^{238}U. Each adding a surface contamination from an external rough surface facing the target detector with a distance of 0.5 cm and a surface contamination of the target crystal itself. ^{210}Po is placed below the rough surface following a simulated ^{210}Po distribution from the ^{222}Rn decay chain. ^{238}U is uniformly placed in a 15 nm thick layer below the rough surface. The rough surfaces are emulated by spikes of 5 µm height and width. Three different energy ranges are presented: 4000-7000 keV (top), 1-900 keV (middle), 0.4-50.0 keV (bottom). For the comfort of the reader, those figures, including the full legend, are added in a bigger format to appendix: Figure A.16, Figure A.17, Figure A.18.

7 Conclusion

In this thesis, I evaluated the influence of a diffused and polished surface contaminated with radiogenic nuclei on the energy spectrum measured by CRESST. I developed a surface simulation library, simulated different energy deposition spectra and thereby showed an improvement of CRESSTs electromagnetic background model for TUM40 and TUM93A detector modules. The geometries of those two modules together with the general experimental setup of CRESST and its detection principle are described in chapter 3. In addition, I gave an overview about several different sources that contribute to the measured data, as well as show the measured surface structure of a diffused and polished $CaWO_4$ crystal.

In chapter 4 I presented the simulation tools developed by the CRESST collaboration: ImpCRESST, CresstDS and Bliss. This is followed by a description and explanation of the Geant4 C++ based library I developed for surface simulations which allows to simulate an actual rough surface and place contaminants on and below the simulated surface in Geant4, meaning inside of the material to be simulated. This novel approach successfully addresses the problem of memory consumption when simulating many volumes and allows one to simulate a rough surface of any size and can be used not only by CRESST, but by any other rare event search experiment.

In chapter 5 I introduce the state of CRESSTs electromagnetic background model for TUM40 before adding surface simulations based on this thesis, then I show simplified surface simulations done by me as a proof of concept in a previous work [13] and point out its problems, which are later addressed by developments and simulations done as a part of this work.

chapter 6 shows the development of simulated surface templates for ^{210}Po and ^{238}U nuclei. To generate physical templates, the used by default in Geant4 physics model for nuclear scattering was inspected, its behaviour was compared to SRIM, a widely used tool for simulating the stopping of ions in matter, and the model SNR was selected for further simulations due to its accurate replication of SRIM simulations. Based on this model, I was able to simulate a ^{210}Po surface distribution from the decay of ^{222}Rn that is later used as a starting point for surface contamination simulations. I investigated the influence of contaminants in the rough surface of the detector crystal as well as in rough surface of an external volume facing the detector. This enabled me to generate final energy deposition templates for ^{210}Po and ^{238}U which are fitted to the data measured with TUM40 and TUM93A detector modules from different Runs of CRESST. Thereby it was found that a contribution from an external rough surface contaminated with ^{210}Po is of significant importance, because it contributes not only in the high energy range to a peak at $\sim 5300\,$keV but also in the lowest energy range, including the ROI by adding an increasing spectrum to lower energies. Adding these templates increased the explainable percentage for the high energy range of TUM40 by 0.57 % (see Table 6.4) and for TUM93A even by 45 % Table 6.7. Furthermore, based on the fitting of templates a surface activity was calculated which is significantly higher than the bulk contamination projected onto the surface, indicating an accumulation of ^{210}Po and ^{238}U on the crystals surface Table 6.6 and Table 6.9.

Table 7.1: Comparison of Surface activity based on simulated and fitted templates for TUM40 (see chapter 6) with surface activity simulated and fitted by CUORE [14]. *For CUORE only a value for ^{210}Pb was available; however, I use this value for ^{210}Po due to assumed secular equilibrium.

	^{210}**Po** [Bq/cm^2]	^{238}**U**[Bq/cm^2]
CUORE	$6.02(8) * 10^{-8*}$	$2.07(11) * 10^{-9}$
TUM40	$5.29 \pm 2.01 * 10^{-8}$	$4.08 \pm 0.31 * 10^{-7}$
TUM93A	$2.21 \pm 0.69 * 10^{-7}$	-

I want to emphasize that with this new developed approach, I was able to simulate surface activity values for ^{210}Po that are comparable to surface activities published by CUORE [14] (see Table 7.1). This is especially promising because ^{210}Po likely originates from ^{210}Pb surface contamination which is implanted in the surface by exposure to ^{222}Rn and does not depend strongly on the initial radiopurity of the crystal.

The developed and tested approach gives promising results and allows for the recognition of rough contaminated surfaces in simulation. However, next steps should be taken to further test the reliability of the simulation and fine-tune it to the variety of CRESSTs detector models.

The biggest challenge in developing the library is the lack of energy deposition data and contamination data to verify the implementations and the correctness of the used physics models in the low energy ($\lesssim 100\,\mathrm{keV}$) regime. The verification of the physics model was partially done by testing it against SRIM; however, for a final confirmation, real measurements with high statistics and extended energy range are essential.

Furthermore, multiple different measurements can be done to improve or confirm the simulation: In chapter 6 a distribution of ^{210}Po below the surface was simulated (see Figure 6.3); however, especially for lower energies the reliability of the physics models used decreases, which can influence the distribution. The model and later the surface contamination simulation can benefit from measuring the depth-dependent composition of different materials such as $CaWO_4$ (detector crystal), copper (module housing), etc., for example, with Secondary Ion Mass Spectrometry (SIMS) as in [88]. With these data, not only can the distribution of surface contamination be improved, but also the physics model used to stop low energetic nuclei. This is important to further investigate the increasing contribution of low energy in the ROI.

The second measurement relates to the influence of a roughened surface on the energy deposition spectrum. It is of interest to test the designed surface model against data with more statistics to confirm its correctness and fine-tune it. This can be done by placing a detector next to sources with differently prepared surfaces (polished, diffused, etc.). Although this measurement could be performed with one of CRESSTs detector crystals, however, with the predicted surface activity, this would result only in $\sim 2\,\mathrm{counts/(yr\,cm^2)}$. To get better statistics, a more active source should be used. Getting a better understanding of the effects induced by the small-scale surface structure and improving the surface simulations allows to probe how to prepare the experimental setup to get less background in the ROI. Furthermore, such an investigation is independent of the explicit experiment and can be an interesting contribution to the field of rare event search.

Another option is to explicitly test the simulation against data related to events coming from surfaces facing the detector. Some of these data, especially surface events within the $CaWO_4$ holding sticks, which then interact with the detector, can potentially be extracted from the measured TUM40 data. This was discussed with Florian Reindl, who did the analysis of the TUM40 data [89]. The holding sticks are in direct contact with the detector crystal; therefore, an event inside the sticks also affect the detector crystal and can be seen as a pulse measured with the TES. However, the pulse is ~ 50 times smaller as a direct hit in the detector would produce and in- and decreases slower. However, if ^{210}Po decays in the surface of the stick, the α particle can deposit its energy inside the stick while the ^{206}Pb nuclei can escape the stick and hit the surface of the target crystal. On the one hand, the accumulated energy should be visible, as well as a slower decrease of the TES pulse. Extracting these data can give an insight of the activity of the holding sticks, as well as give explicit low energy data to test against it. The benefit of this approach would be that the measurement is already done; however, before following this approach a short analysis should be performed to estimate the expected amount of surface data.

Apart from doing measurements, the ImpCRESST simulation itself can be further improved by using the developed library to cover the surfaces of the already existing ImpCRESST detector module and simulate more surface contributions, especially from beta decaying nuclei like ^{210}Pb or ^{210}Bi, from different parts with different materials using the detector's actual geometry. This allows a more detailed background model to be created and can be used to test future module configurations and to suggest actions to reduce the background in the ROI.

Improving surface contamination simulations and gaining more insight into the effects of a contaminated and roughened surface can be crucial to further suppress the remaining electromagnetic background. This is not a problem specific to CRESST, but many rare event search experiments must address [14, 15]. With this thesis, a first big step was taken to include surface roughness and its contamination in Geant4 simulations and improve electromagnetic background models.

Bibliography

[1] P. A. R. Ade *et al.*, "Planck 2015 results: XIII. Cosmological parameters," *Astronomy & Astrophysics*, vol. 594, A13, Sep. 2016, ISSN: 1432-0746. DOI: 10.1051/0004-6361/201525830. [Online]. Available: http://dx.doi.org/10.1051/0004-6361/201525830.

[2] G. Jungman, M. Kamionkowski, and K. Griest, "Supersymmetric dark matter," *Physics Reports*, vol. 267, no. 5, pp. 195–373, 1996, ISSN: 0370-1573. DOI: https://doi.org/10.1016/0370-1573(95)00058-5. [Online]. Available: https://www.sciencedirect.com/science/article/pii/0370157395000585.

[3] M. Milgrom, "A modification of the Newtonian dynamics - Implications for galaxies.," *Astrophysical Journal*, vol. 270, pp. 371–383, Jul. 1983. DOI: 10.1086/161131.

[4] M. DREWES, "The phenomenology of right handed neutrinos," *International Journal of Modern Physics E*, vol. 22, no. 08, p. 1 330 019, 2013. DOI: 10.1142/S0218301313300191. eprint: https://doi.org/10.1142/S0218301313300191. [Online]. Available: https://doi.org/10.1142/S0218301313300191.

[5] C. Alcock *et al.*, "The MACHO Project: Microlensing Results from 5.7 Years of Large Magellanic Cloud Observations," *The Astrophysical Journal*, vol. 542, no. 1, p. 281, Oct. 2000. DOI: 10.1086/309512. [Online]. Available: https://dx.doi.org/10.1086/309512.

[6] I. Irastorza, "An introduction to axions and their detection," *SciPost Physics Lecture Notes*, Mar. 2022. DOI: 10.21468/SciPostPhysLectNotes.45.

[7] L. Roszkowski, E. M. Sessolo, and S. Trojanowski, "WIMP dark matter candidates and searches—current status and future prospects," *Reports on Progress in Physics*, vol. 81, no. 6, p. 066 201, May 2018. DOI: 10.1088/1361-6633/aab913. [Online]. Available: https://dx.doi.org/10.1088/1361-6633/aab913.

[8] A. Münster, "High-purity $CaWO_4$ single crystals for direct dark matter search with the CRESST experiment," Ph.D. dissertation, TU München, 2017. [Online]. Available: https://nbn-resolving.de/urn/resolver.pl?urn:nbn:de:bvb:91-diss-20171117-1393806-1-5.

[9] G. Angloher *et al.*, "Probing spin-dependent dark matter interactions with ^{6}Li," *The European Physical Journal C*, vol. 82, no. 3, Mar. 2022. DOI: 10.1140/epjc/s10052-022-10140-3. [Online]. Available: https://doi.org/10.1140%2Fepjc%2Fs10052-022-10140-3.

[10] G. Angloher *et al.*, "Results on sub-GeV dark matter from a 10 eV threshold CRESST-III silicon detector," *Physical Review D*, vol. 107, no. 12, Jun. 2023. DOI: 10.1103/physrevd.107.122003. [Online]. Available: https://doi.org/10.1103%2Fphysrevd.107.122003.

[11] A. H. Abdelhameed *et al.*, "Geant4-based electromagnetic background model for the CRESST dark matter experiment," *The European Physical Journal C*, vol. 79, no. 10, Oct. 2019. DOI: 10.1140/epjc/s10052-019-7385-0. [Online]. Available: https://doi.org/10.1140%2Fepjc%2Fs10052-019-7385-0.

[12] G. Angloher *et al.*, "High-Dimensional Bayesian Likelihood Normalisation for CRESST's Background Model," 2023. arXiv: 2307.12991 [physics.ins-det].

[13] C. Grüner *et al.*, "Geant4 simulations of the influence of contamination and roughness of the detector surface on background spectra in cresst," in *Proceedings of Science*, Feb. 2024, p. 092. DOI: 10.22323/1.441.0092.

[14] C. Alduino *et al.*, "Measurement of the two-neutrino double-beta decay half-life of

130

Te with the CUORE-0 experiment," *The European Physical Journal C*, vol. 77, no. 1, Jan. 2017, ISSN: 1434-6052. DOI: 10.1140/epjc/s10052-016-4498-6. [Online]. Available: http://dx.doi.org/10.1140/epjc/s10052-016-4498-6.

[15] G. e. a. Adhikari, "Background modeling for dark matter search with 1.7 years of cosine-100 data," *The European Physical Journal C*, vol. 81, 2021. DOI: 10.1140/epjc/s10052-021-09564-0.

[16] Challis, "II. Account of Observations at the Cambridge Observatory for detecting the Planet exterior to Uranus," *Monthly Notices of the Royal Astronomical Society*, vol. 7, no. 9, pp. 145–149, Nov. 1846, ISSN: 0035-8711. DOI: 10.1093/mnras/7.9.145. eprint: https://academic.oup.com/mnras/article-pdf/7/9/145/3063436/mnras7-0145.pdf. [Online]. Available: https://doi.org/10.1093/mnras/7.9.145.

[17] R. Massey, T. Kitching, and J. Richard, "The dark matter of gravitational lensing," *Reports on Progress in Physics*, vol. 73, no. 8, p. 086 901, Jul. 2010. DOI: 10.1088/0034-4885/73/8/086901. [Online]. Available: https://doi.org/10.1088%2F0034-4885%2F73%2F8%2F086901.

[18] M. Roos, "Astrophysical and Cosmological Probes of Dark Matter," *Journal of Modern Physics*, vol. 03, no. 09, pp. 1152–1171, 2012. DOI: 10.4236/jmp.2012.329150. [Online]. Available: https://doi.org/10.4236%2Fjmp.2012.329150.

[19] D. Naumov, "The Sterile Neutrino: A short introduction," *EPJ Web of Conferences*, vol. 207, p. 04 004, Jan. 2019. DOI: 10.1051/epjconf/201920704004.

[20] K. G. Begeman, A. H. Broeils, and R. H. Sanders, "Extended rotation curves of spiral galaxies: dark haloes and modified dynamics," *Monthly Notices of the Royal Astronomical Society*, vol. 249, no. 3, pp. 523–537, Apr. 1991, ISSN: 0035-8711. DOI: 10.1093/mnras/249.3.523. eprint: https://academic.oup.com/mnras/article-pdf/249/3/523/18160929/mnras249-0523.pdf. [Online]. Available: https://doi.org/10.1093/mnras/249.3.523.

[21] G. Bertone, D. Hooper, and J. Silk, "Particle dark matter: Evidence, candidates and constraints," *Physics Reports*, vol. 405, no. 5, pp. 279–390, 2005, ISSN: 0370-1573. DOI: https://doi.org/10.1016/j.physrep.2004.08.031. [Online]. Available: https://www.sciencedirect.com/science/article/pii/S0370157304003515.

[22] D. Clowe *et al.*, "A direct empirical proof of the existence of dark matter," *The Astrophysical Journal*, vol. 648, no. 2, pp. L109–L113, Aug. 2006, ISSN: 1538-4357. DOI: 10.1086/508162. [Online]. Available: http://dx.doi.org/10.1086/508162.

[23] "The bullet cluster." (2006), [Online]. Available: https://chandra.si.edu/photo/2006/1e0657/ (visited on 08/23/2024).

[24] D. J. Fixsen, "The temperature of the cosmic microwave background," *The Astrophysical Journal*, vol. 707, no. 2, p. 916, Nov. 2009. DOI: 10.1088/0004-637X/707/2/916. [Online]. Available: https://dx.doi.org/10.1088/0004-637X/707/2/916.

[25] P. D. Group *et al.*, "Review of Particle Physics," *Progress of Theoretical and Experimental Physics*, vol. 2020, no. 8, p. 083C01, Aug. 2020, ISSN: 2050-3911. DOI: 10.1093/ptep/ptaa104. eprint: https://academic.oup.com/ptep/article-pdf/2020/8/083C01/34673722/ptaa104.pdf. [Online]. Available: https://doi.org/10.1093/ptep/ptaa104.

[26] P. A. R. Ade *et al.*, "Planck2013 results. xvi. cosmological parameters," *Astronomy & Astrophysics*, vol. 571, A16, Oct. 2014, ISSN: 1432-0746. DOI: 10.1051/0004-6361/201321591. [Online]. Available: http://dx.doi.org/10.1051/0004-6361/201321591.

[27] G. B. J.R. Primack, "What is the dark matter?" In *Formation and Evolution of Galaxies and Large Structures in the Universe*, J. T. T. V. J. Audouze, Ed., 1984, pp. 163–183.

[28] S. D. M. White, C. S. Frenk, and M. Davis, "Clustering in a neutrino-dominated universe," *apjl*, vol. 274, pp. L1–L5, Nov. 1983. DOI: 10.1086/184139.

[29] F. Wilczek, "The Birth of Axions," *Current Contents*, 1991.

[30] R. D. Peccei and H. R. Quinn, "CP conservation in the presence of pseudoparticles," *Phys. Rev. Lett.*, vol. 38, pp. 1440–1443, 25 Jun. 1977. DOI: 10.1103/PhysRevLett.38.1440. [Online]. Available: https://link.aps.org/doi/10.1103/PhysRevLett.38.1440.

[31] A. Fuß, "Simulation based neutron background studies for the CRESST and COSINUS dark matter search experiments," Ph.D. dissertation, TU Wien, 2022. DOI: 10.34726/hss.2022.86617.

[32] O. Buchmueller, C. Doglioni, and L.-T. Wang, "Search for dark matter at colliders," *Nature Physics*, vol. 13, no. 3, pp. 217–223, Mar. 2017. DOI: 10.1038/nphys4054. [Online]. Available: https://doi.org/10.1038%2Fnphys4054.

[33] M. Aartsen *et al.*, "The IceCube Neutrino Observatory: instrumentation and online systems," *Journal of Instrumentation*, vol. 12, no. 03, P03012–P03012, Mar. 2017. DOI: 10.1088/1748-0221/12/03/p03012. [Online]. Available: https://doi.org/10.1088%2F1748-0221%2F12%2F03%2Fp03012.

[34] M. G. Aartsen *et al.*, "Search for dark matter annihilations in the sun with the 79-string icecube detector," *Phys. Rev. Lett.*, vol. 110, p. 131 302, 13 Mar. 2013. DOI: 10.1103/PhysRevLett.110.131302. [Online]. Available: https://link.aps.org/doi/10.1103/PhysRevLett.110.131302.

[35] D. J. Thompson and C. A. Wilson-Hodge, "Fermi Gamma-Ray Space Telescope," in *Handbook of X-ray and Gamma-ray Astrophysics*, C. Bambi and A. Santangelo, Eds. Singapore: Springer Nature Singapore, 2022, pp. 1–31, ISBN: 978-981-16-4544-0. DOI: 10.1007/978-981-16-4544-0_58-1. [Online]. Available: https://doi.org/10.1007/978-981-16-4544-0_58-1.

[36] J. W. Foster, Y. Park, B. R. Safdi, Y. Soreq, and W. L. Xu, "Search for dark matter lines at the galactic center with 14 years of fermi data," *Physical Review D*, vol. 107, no. 10, May 2023, ISSN: 2470-0029. DOI: 10.1103/physrevd.107.103047. [Online]. Available: http://dx.doi.org/10.1103/PhysRevD.107.103047.

[37] T. SAAB, "An Introduction to Dark Matter Direct Detection Searches & Techniques," in *The Dark Secrets of the Terascale*, WORLD SCIENTIFIC, Feb. 2013, pp. 711–738. DOI: 10.1142/9789814390163_0011. [Online]. Available: https://doi.org/10.1142%2F9789814390163_0011.

[38] E. Aprile *et al.*, "Low-mass dark matter search using ionization signals in xenon100," *Phys. Rev. D*, vol. 94, p. 092 001, 9 Nov. 2016. DOI: 10.1103/PhysRevD.94.092001. [Online]. Available: https://link.aps.org/doi/10.1103/PhysRevD.94.092001.

[39] E. Aprile *et al.*, "Dark matter search results from a one ton-year exposure of xenon1t," *Phys. Rev. Lett.*, vol. 121, p. 111 302, 11 Sep. 2018. DOI: 10.1103/PhysRevLett.121.111302. [Online]. Available: https://link.aps.org/doi/10.1103/PhysRevLett.121.111302.

[40] P. Agnes *et al.*, "Low-mass dark matter search with the darkside-50 experiment," *Phys. Rev. Lett.*, vol. 121, p. 081 307, 8 Aug. 2018. DOI: 10.1103/PhysRevLett.121.081307. [Online]. Available: https://link.aps.org/doi/10.1103/PhysRevLett.121.081307.

[41] D. S. Akerib *et al.*, "Results from a search for dark matter in the complete lux exposure," *Phys. Rev. Lett.*, vol. 118, p. 021 303, 2 Jan. 2017. DOI: 10.1103/PhysRevLett.118.021303. [Online]. Available: https://link.aps.org/doi/10.1103/PhysRevLett.118.021303.

[42] X. Cui *et al.*, "Dark matter results from 54-ton-day exposure of pandax-ii experiment," *Phys. Rev. Lett.*, vol. 119, p. 181 302, 18 Oct. 2017. DOI: 10.1103/PhysRevLett.119.181302. [Online]. Available: https://link.aps.org/doi/10.1103/PhysRevLett.119.181302.

[43] Q. Arnaud, D. Asner, J.-P. Bard, A. Brossard, and et al., "First results from the news-g direct dark matter search experiment at the lsm," *Astroparticle Physics*, vol. 97, 2018. DOI: https://doi.org/10.1016/j.astropartphys.2017.10.009..

[44] A. H. Abdelhameed *et al.*, "First results from the CRESST-III low-mass dark matter program," *Physical Review D*, vol. 100, no. 10, Nov. 2019, ISSN: 2470-0029. DOI: 10.1103/physrevd.100.102002. [Online]. Available: http://dx.doi.org/10.1103/PhysRevD.100.102002.

[45] R. Agnese *et al.*, "New results from the search for low-mass weakly interacting massive particles with the cdms low ionization threshold experiment," *Phys. Rev. Lett.*, vol. 116, p. 071 301, 7 Feb. 2016. DOI: 10.1103/PhysRevLett.116.071301. [Online]. Available: https://link.aps.org/doi/10.1103/PhysRevLett.116.071301.

[46] A. Aguilar-Arevalo *et al.*, "Search for low-mass wimps in a 0.6 kg day exposure of the damic experiment at snolab," *Phys. Rev. D*, vol. 94, p. 082 006, 8 Oct. 2016. DOI: 10.1103/PhysRevD.94.082006. [Online]. Available: https://link.aps.org/doi/10.1103/PhysRevD.94.082006.

[47] L. Hehn *et al.*, "Improved edelweiss-iii sensitivity for low-mass wimps using a profile likelihood approach," *The European Physical Journal C*, vol. 76, no. 10, Oct. 2016, ISSN: 1434-6052. DOI: 10.1140/epjc/s10052-016-4388-y. [Online]. Available: http://dx.doi.org/10.1140/epjc/s10052-016-4388-y.

[48] R. Bernabei *et al.*, *Dark matter: Dama/libra and its perspectives*, 2022. arXiv: 2209.00882 [hep-ex]. [Online]. Available: https://arxiv.org/abs/2209.00882.

[49] K. Freese, M. Lisanti, and C. Savage, "Colloquium: Annual modulation of dark matter," *Reviews of Modern Physics*, vol. 85, no. 4, pp. 1561–1581, Nov. 2013, ISSN: 1539-0756. DOI: 10.1103/revmodphys.85.1561. [Online]. Available: http://dx.doi.org/10.1103/RevModPhys.85.1561.

[50] G. A. et al., "The cosinus project: Perspectives of a nai scintillating calorimeter for dark matter search.," *Eur. Phys. J. C 76, 441*, 2016. DOI: https://doi.org/10.1140/epjc/s10052-016-4278-3.

[51] A. H. Abdelhameed *et al.*, "First results from the CRESST-III low-mass dark matter program," *Physical Review D*, vol. 100, no. 10, Nov. 2019, ISSN: 2470-0029. DOI: 10.1103/physrevd.100.102002. [Online]. Available: http://dx.doi.org/10.1103/PhysRevD.100.102002.

[52] M. Ambrosio *et al.*, "Vertical muon intensity measured with MACRO at the Gran Sasso laboratory," *Physical Review D*, vol. 52, pp. 3793–3802, 7 Oct. 1995. DOI: 10.1103/PhysRevD.52.3793. [Online]. Available: https://link.aps.org/doi/10.1103/PhysRevD.52.3793.

[53] G. Angloher *et al.*, "Results on sub-GeV dark matter from a 10 eV threshold CRESST-III silicon detector," *Physical Review D*, vol. 107, no. 12, Jun. 2023. DOI: 10.1103/physrevd.107.122003. [Online]. Available: https://doi.org/10.1103%2Fphysrevd.107.122003.

[54] A. Gütlein, G. Angloher, A. Bento, C. Bucci, and et al., "Impact of coherent neutrino nucleus scattering on direct dark matter searches based on cawo4 crystals," *Astroparticle Physics*, vol. 69, 2015. DOI: https://doi.org/10.1016/j.astropartphys.2015.03.010..

[55] A. Kinast, "Enhancing the Dark Matter Sensitivity of CRESST: Purification, Stress Reduction and 17O Enrichment of $CaWO_4$ Target Crystals," Ph.D. dissertation, TU München, 2023. [Online]. Available: https://nbn-resolving.de/urn/resolver.pl?urn:nbn:de:bvb:91-diss-20231220-1726057-1-3.

[56] F. Pröbst *et al.*, "Model for cryogenic particle detectors with superconducting phase transition thermometers," vol. 100, 1995. DOI: https://doi.org/10.1007/BF00753837.

[57] R. Strauss *et al.*, "A detector module with highly efficient surface-alpha event rejection operated in cresst-ii phase 2," *The European Physical Journal C*, vol. 75, no. 8, Jul. 2015, ISSN: 1434-6052. DOI: 10.1140/epjc/s10052-015-3572-9. [Online]. Available: http://dx.doi.org/10.1140/epjc/s10052-015-3572-9.

[58] M. Kiefer *et al.*, "In-situ study of light production and transport in phonon/light detector modules for dark matter search," *Nuclear Instruments and Methods in Physics Research Section A: Accelerators, Spectrometers, Detectors and Associated Equipment*, vol. 821, pp. 116–121, Jun. 2016. DOI: 10.1016/j.nima.2016.03.035. [Online]. Available: https://doi.org/10.1016%2Fj.nima.2016.03.035.

[59] R. J. Strauß, "Energy-dependent quenching factor measurements of cawo₄ crystals at mk temperatures and detector prototypes for direct dark matter search with cresst," en, Ph.D. dissertation, Technische Universität München, 2013, p. 197. [Online]. Available: https://mediatum.ub.tum.de/1166886.

[60] R. Strauss *et al.*, "Beta/gamma and alpha backgrounds in cresst-ii phase 2," *Journal of Cosmology and Astroparticle Physics*, vol. 2015, no. 06, pp. 030–030, Jun. 2015, ISSN: 1475-7516. DOI: 10.1088/1475-7516/2015/06/030. [Online]. Available: http://dx.doi.org/10.1088/1475-7516/2015/06/030.

[61] G. Angloher *et al.*, "Results on low mass wimps using an upgraded cresst-ii detector," *The European Physical Journal C*, vol. 74, no. 12, Dec. 2014, ISSN: 1434-6052. DOI: 10.1140/epjc/s10052-014-3184-9. [Online]. Available: http://dx.doi.org/10.1140/epjc/s10052-014-3184-9.

[62] M. Kiefer, "Improving the light channel of the cresst-ii-dark matter detectors," en, Ph.D. dissertation, Technische Universität München, 2012, p. 175. [Online]. Available: https://mediatum.ub.tum.de/1097360.

[63] M. v. Sivers *et al.*, "Influence of annealing on the optical and scintillation properties of single crystals," *Optical Materials*, vol. 34, no. 11, pp. 1843–1848, Sep. 2012. DOI: 10.1016/j.optmat.2012.05.014. [Online]. Available: https://doi.org/10.1016/j.optmat.2012.05.014.

[64] A. Kinast *et al.*, "Characterisation of low background $CaWO_4$ crystals for CRESST-III," *SciPost Phys. Proc.*, p. 031, 2023. DOI: 10.21468/SciPostPhysProc.12.031. [Online]. Available: https://scipost.org/10.21468/SciPostPhysProc.12.031.

[65] V. Mokina, "Study of surface roughness," *Project at HEPHY*,

[66] A. H. Abdelhameed *et al.*, "Geant4-based electromagnetic background model for the CRESST dark matter experiment," *The European Physical Journal C*, vol. 79, no. 10, Oct. 2019. DOI: 10.1140/epjc/s10052-019-7385-0. [Online]. Available: https://doi.org/10.1140%2Fepjc%2Fs10052-019-7385-0.

[67] N. Agafonova *et al.*, "Analysis of seasonal variations of the cosmic ray muon flux and neutrons produced by muons in the lvd detector," *Bulletin of the Russian Academy of Sciences: Physics*, vol. 75, pp. 427–430, Mar. 2011. DOI: 10.3103/S1062873811030063.

[68] M. Kimmerle, "Data Analysis in the Direct Dark Matter Search Experiment CRESST and Calculation of the corresponding Limit on the Cross Section of Dark Matter," Ph.D. dissertation, Eberhard Karls Universität Tübingen, 2010. [Online]. Available: http://nbn-resolving.de/urn:nbn:de:bsz:21-opus-55770.

[69] S. Cebrián, "Cosmogenic activation of materials," *International Journal of Modern Physics A*, vol. 32, no. 30, p. 1 743 006, Oct. 2017, ISSN: 1793-656X. DOI: 10.1142/s0217751x17430060. [Online]. Available: http://dx.doi.org/10.1142/S0217751X17430060.

[70] R. Lang *et al.*, "Electron and gamma background in cresst detectors," *Astroparticle Physics*, vol. 32, no. 6, pp. 318–324, Jan. 2010, ISSN: 0927-6505. DOI: 10.1016/j.astropartphys.2009.09.009. [Online]. Available: http://dx.doi.org/10.1016/j.astropartphys.2009.09.009.

[71] S. Cebrián, "Cosmogenic activation of materials," *International Journal of Modern Physics A*, vol. 32, no. 30, p. 1 743 006, Oct. 2017. DOI: 10.1142/s0217751x17430060. [Online]. Available: https://doi.org/10.1142%2Fs0217751x17430060.

[72] M. Haffke *et al.*, "Background measurements in the gran sasso underground laboratory," *Nuclear Instruments and Methods in Physics Research Section A: Accelerators, Spectrometers, Detectors and Associated Equipment*, vol. 643, no. 1, pp. 36–41, Jul. 2011, ISSN: 0168-9002. DOI: 10.1016/j.nima.2011.04.027. [Online]. Available: http://dx.doi.org/10.1016/j.nima.2011.04.027.

[73] R. F. Lang, "Search for Dark Matter with the CRESST Experiment," Ph.D. dissertation, TU München, 2008. [Online]. Available: https://nbn-resolving.de/urn/resolver.pl?urn:nbn:de:bvb:91-diss-20081027-677820-1-7.

[74] W. Commons. "Uranium-238 decay chain diagram." File:Decay chain(4n+2, Uranium series).svg. (2014), [Online]. Available: https://commons.wikimedia.org/wiki/File:Decay_chain%284n%2B2,_Uranium_series%29.svg.

[75] Federal Republic of Germany, represented by the Federal Ministry for the Environment, Nature Conservation, Nuclear Safety and Consumer Protection, which is in turn represented by the Federal Office for Radiation Protection. "Bundesamt für Strahlenschutz." (2023), [Online]. Available: https://www.bfs.de/ (visited on 04/14/2023).

[76] J. Allison *et al.*, "Recent developments in Geant4," *Nuclear Instruments and Methods in Physics Research Section A: Accelerators, Spectrometers, Detectors and Associated Equipment*, vol. 835, pp. 186–225, 2016, ISSN: 0168-9002. DOI: https://doi.org/10.1016/j.nima.2016.06.125. [Online]. Available: https://www.sciencedirect.com/science/article/pii/S0168900216306957.

[77] J. Allison *et al.*, "Geant4 developments and applications," *IEEE Transactions on Nuclear Science*, vol. 53, no. 1, pp. 270–278, 2006. DOI: 10.1109/TNS.2006.869826.

[78] S. Agostinelli *et al.*, "Geant4—a simulation toolkit," *Nuclear Instruments and Methods in Physics Research Section A: Accelerators, Spectrometers, Detectors and Associated Equipment*, vol. 506, no. 3, pp. 250–303, 2003, ISSN: 0168-9002. DOI: https://doi.org/10.1016/S0168-9002(03)01368-8. [Online]. Available: https://www.sciencedirect.com/science/article/pii/S0168900203013688.

[79] R. Brun and F. Rademakers, "ROOT — An object oriented data analysis framework," *Nuclear Instruments and Methods in Physics Research Section A: Accelerators, Spectrometers, Detectors and Associated Equipment*, vol. 389, no. 1, pp. 81–86, 1997, New Computing Techniques in Physics Research V, ISSN: 0168-9002. DOI: `https://doi.org/10.1016/S0168-9002(97)00048-X`. [Online]. Available: `https://www.sciencedirect.com/science/article/pii/S016890029700048X`.

[80] C. M. Poole, I. Cornelius, J. V. Trapp, and C. M. Langton, "A CAD Interface for GEANT4," *Australasian Physical & Engineering Science in Medicine*, Sep. 2012. DOI: `10.1007/s13246-012-0159-8`. [Online]. Available: `http://www.springerlink.com/content/u563877422284578`.

[81] P. Schmidt, "Time resolution for simulations," *Project Thesis at HEPHY*, 2023.

[82] A. Caldwell, D. Kollár, and K. Kröninger, "Bat – the bayesian analysis toolkit," *Computer Physics Communications*, vol. 180, no. 11, pp. 2197–2209, Nov. 2009, ISSN: 0010-4655. DOI: `10.1016/j.cpc.2009.06.026`. [Online]. Available: `http://dx.doi.org/10.1016/j.cpc.2009.06.026`.

[83] C. Grüner, "Simulation of surface roughness and its potential impact on electromagnetic background measurements," *Project Thesis at HEPHY*, 2024.

[84] A. Erb and J.-C. Lanfranchi, "Growth of high-purity scintillating $CaWO_4$ single crystals for the low-temperature direct dark matter search experiments CRESST-II and EURECA," *CrystEngComm*, vol. 15, no. 12, pp. 231–234, 2013. DOI: `https://doi.org/10.1039/C2CE26554K`.

[85] M. H. Mendenhall and R. A. Weller, "An algorithm for computing screened coulomb scattering in geant4," *Nuclear Instruments and Methods in Physics Research Section B: Beam Interactions with Materials and Atoms*, vol. 227, no. 3, pp. 420–430, Jan. 2005, ISSN: 0168-583X. DOI: `10.1016/j.nimb.2004.08.014`. [Online]. Available: `http://dx.doi.org/10.1016/j.nimb.2004.08.014`.

[86] J. F. Ziegler, M. D. Ziegler, and J. P. Biersack, "SRIM - The stopping and range of ions in matter (2010)," *Nuclear Instruments and Methods in Physics Research B*, vol. 268, no. 11-12, pp. 1818–1823, Jun. 2010. DOI: `10.1016/j.nimb.2010.02.091`.

[87] Y. Zhang *et al.*, "Damage profile and ion distribution of slow heavy ions in compounds," *Journal of Applied Physics*, vol. 105, no. 10, p. 104 901, May 2009, ISSN: 0021-8979. DOI: `10.1063/1.3118582`. eprint: `https://pubs.aip.org/aip/jap/article-pdf/doi/10.1063/1.3118582/16692502/104901\_1\_online.pdf`. [Online]. Available: `https://doi.org/10.1063/1.3118582`.

[88] Y. Zhang *et al.*, "Damage profile and ion distribution of slow heavy ions in compounds," *Journal of Applied Physics*, vol. 105, no. 10, p. 104 901, May 2009, ISSN: 0021-8979. DOI: `10.1063/1.3118582`. eprint: `https://pubs.aip.org/aip/jap/article-pdf/doi/10.1063/1.3118582/16692502/104901\_1\_online.pdf`. [Online]. Available: `https://doi.org/10.1063/1.3118582`.

[89] F. Reindl, "Exploring light dark matter with cresst-ii low-threshold detectors," en, Ph.D. dissertation, Technische Universität München, 2016, p. 206. [Online]. Available: `https://mediatum.ub.tum.de/1294132`.

[90] "Live chart of nuclides." (2023), [Online]. Available: `https://www-nds.iaea.org/relnsd/vcharthtml/VChartHTML.html` (visited on 08/26/2024).

A | Additional Fits to Measured Data

For convenience of the reader, important fits are replaced in a bigger format in this section. All sidewaysfigures show simulated spectra from bulk contamination or bulk- and surface contamination (coloured, filled histograms). The simulated spectra are fitted to the experimental data of TUM40 [11] or TUM93A [55] (black, open histogram) using a Gaussian likelihood fit normalisation method and Bliss [12].

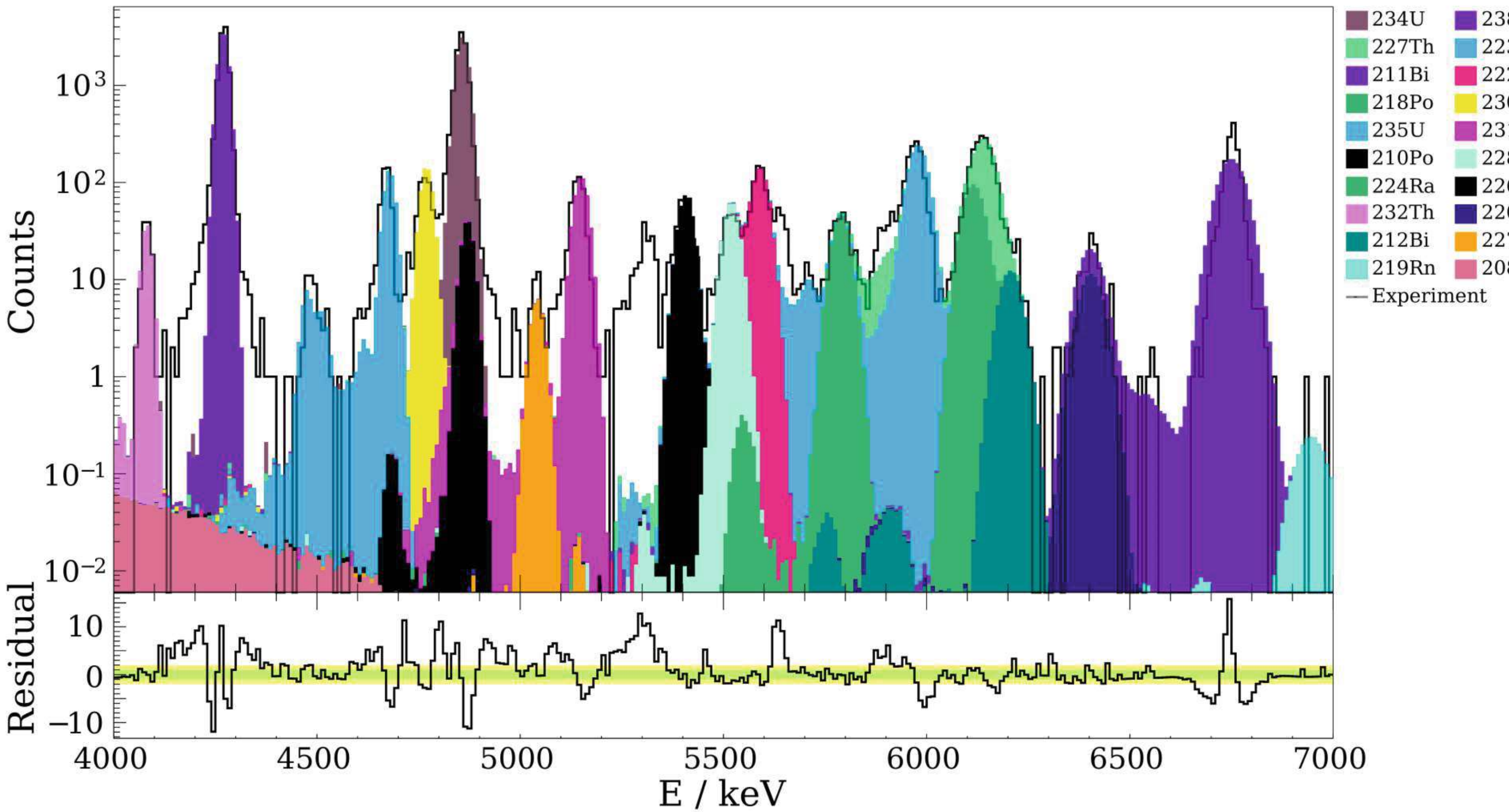

Figure A.1: Simulated spectra for the high energy range (colored, filled histograms) combined via the likelihood normalization method [12] and fitted to the experimental energy data (black, open histogram) of CRESST's TUM40 detector [84]. Figure adapted from [12]. Origin: Figure 5.1.

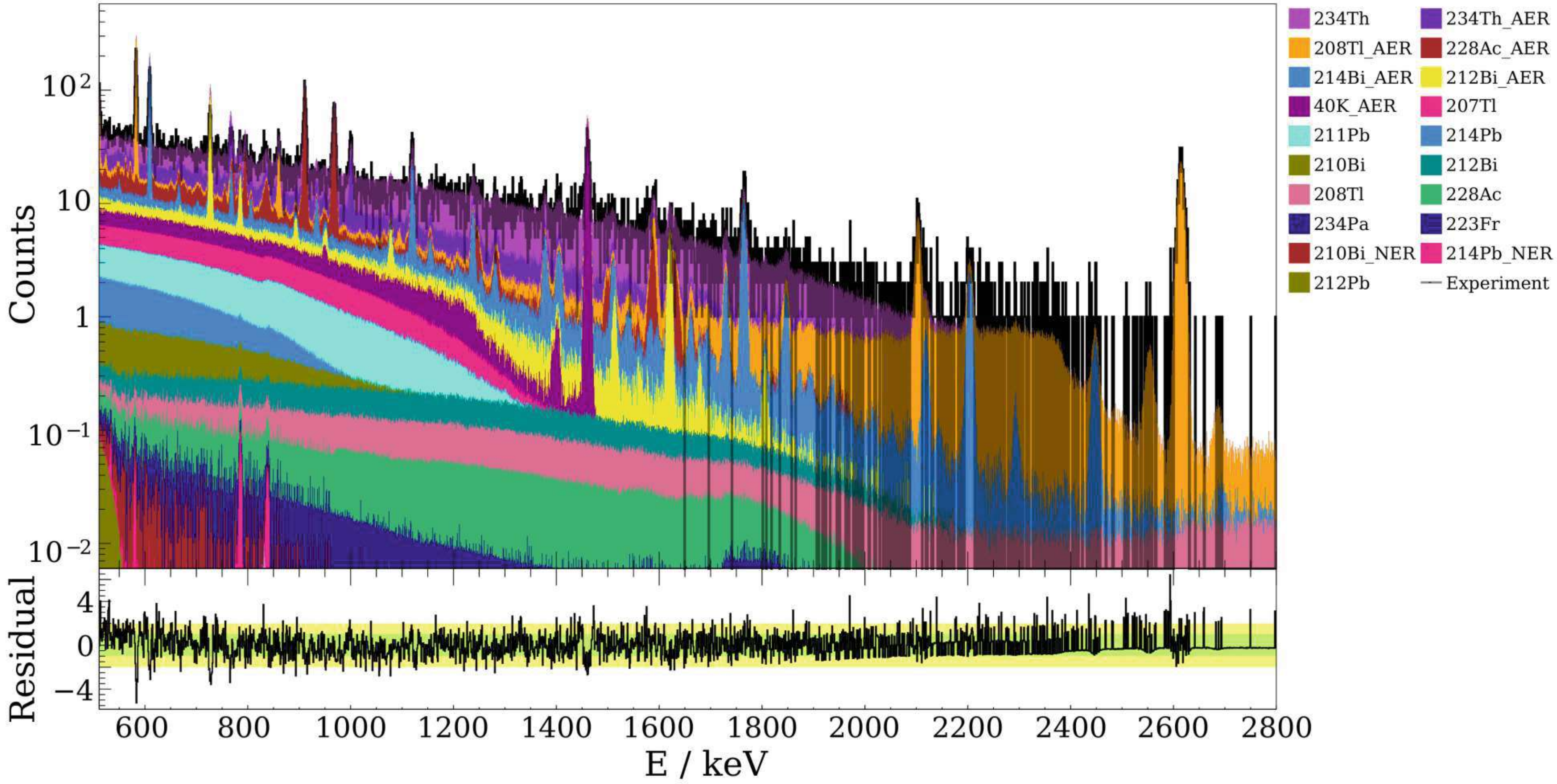

Figure A.2: Simulated spectra for medium energy range (colored, filled histograms) combined via the likelihood normalization method [12] and fitted to the experimental energy data (black, open histogram) of CRESST's TUM40 detector [84]. Figure adapted from [12]. Addendum to original Figure 5.1.

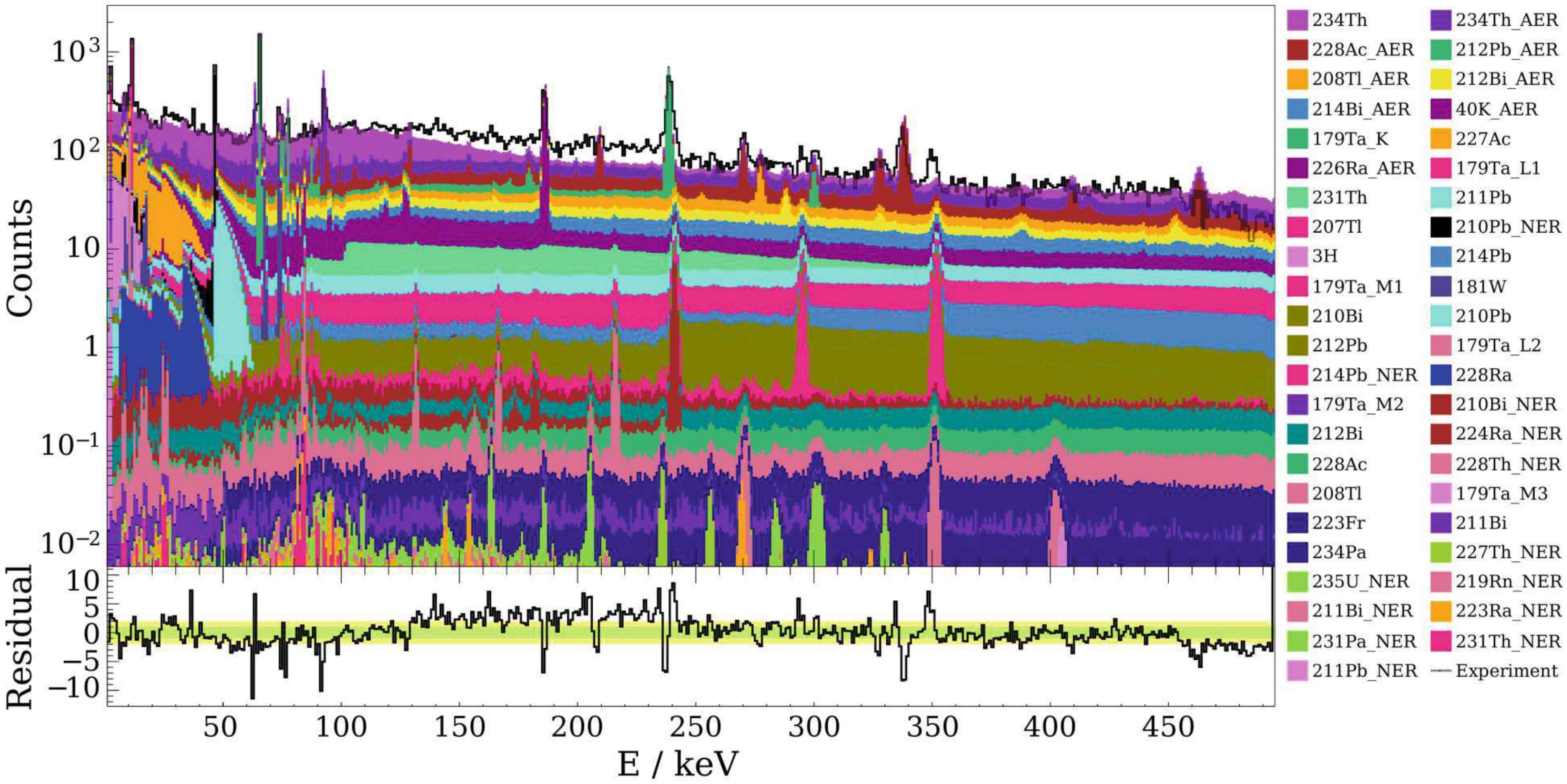

Figure A.3: simulated spectra for the low energy range (colored, filled histograms) combined via the likelihood normalization method [12] and fitted to the experimental energy data (black, open histogram) of CRESST's TUM40 detector [84]. Figure adapted from [12]. Addendum to original Figure 5.1.

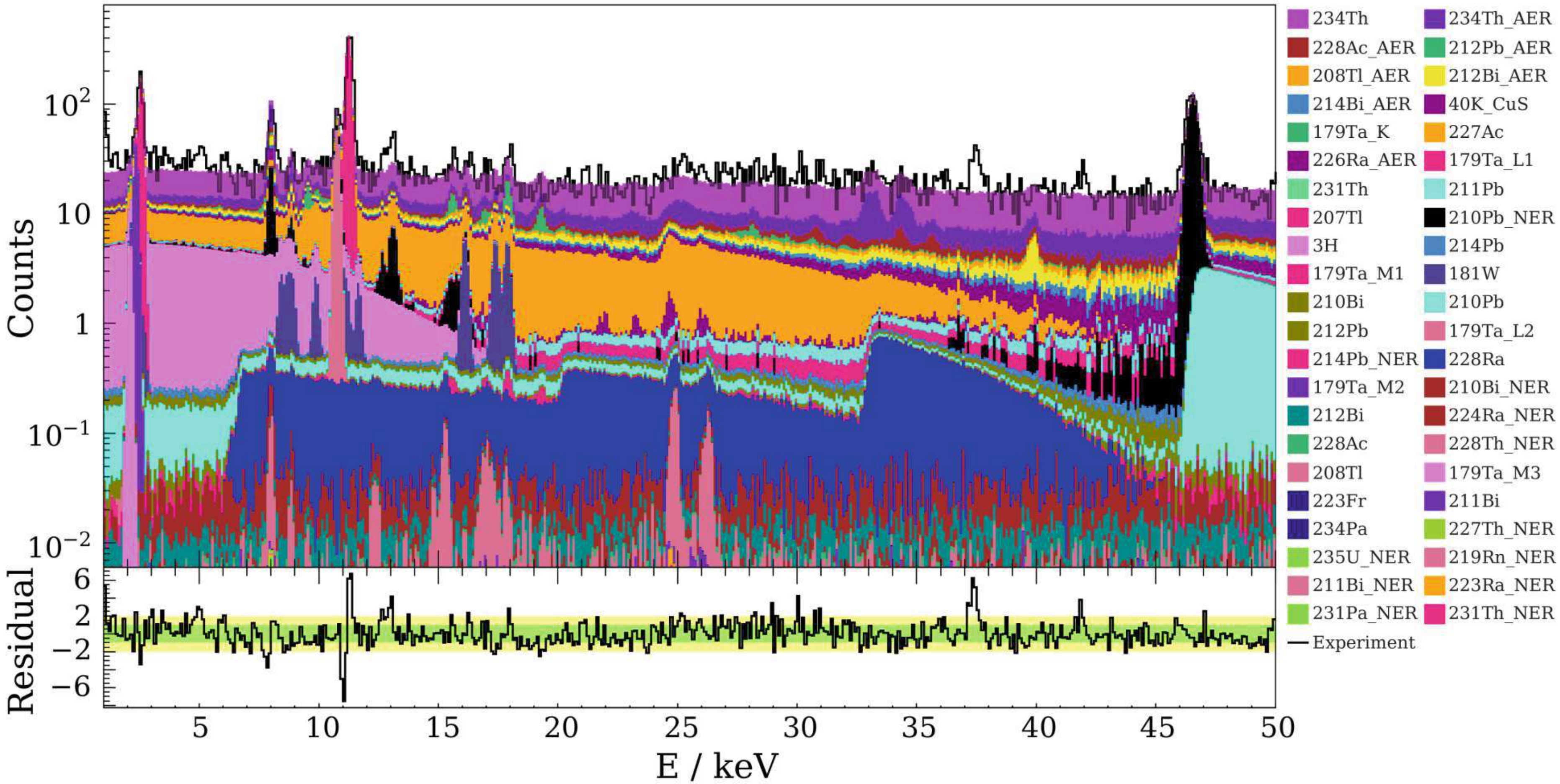

Figure A.4: Simulated spectra for lowest energy range including the ROI (colored, filled histograms) combined via the likelihood normalization method [12] and fitted to the experimental energy data (black, open histogram) of CRESST's TUM40 detector [84]. Figures adapted from [12]. Addendum to original Figure 5.1.

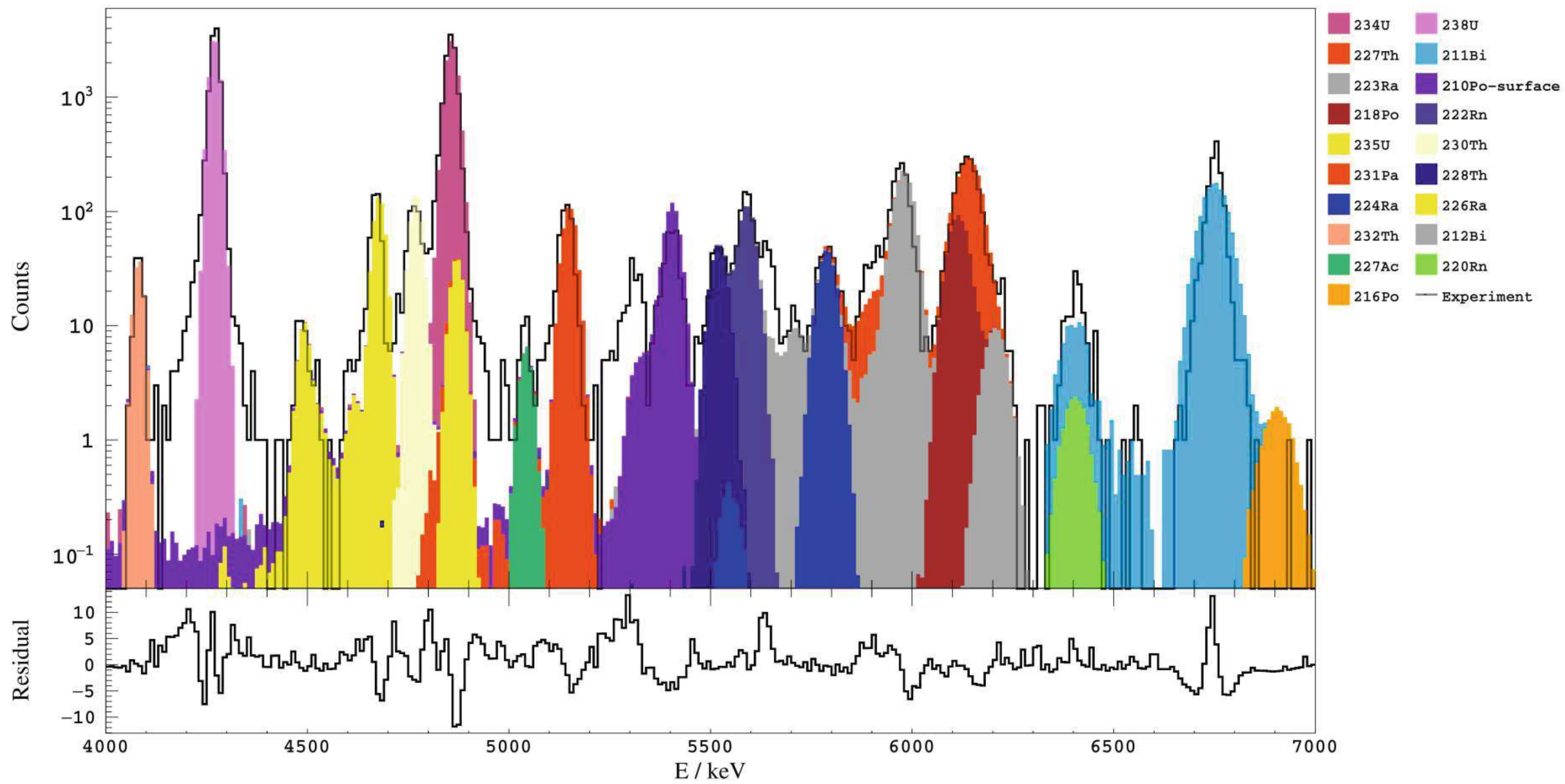

Figure A.5: Fit of simulated energy deposition templates (colored, filled histograms) including a template for surface roughness and contamination by ^{210}Po, following a distribution, to the measured data (black, open histogram) of TUM40, done with Bliss [12, 60]. The α and the α + ^{206}Pb peak can be seen. Origin: Figure 6.8

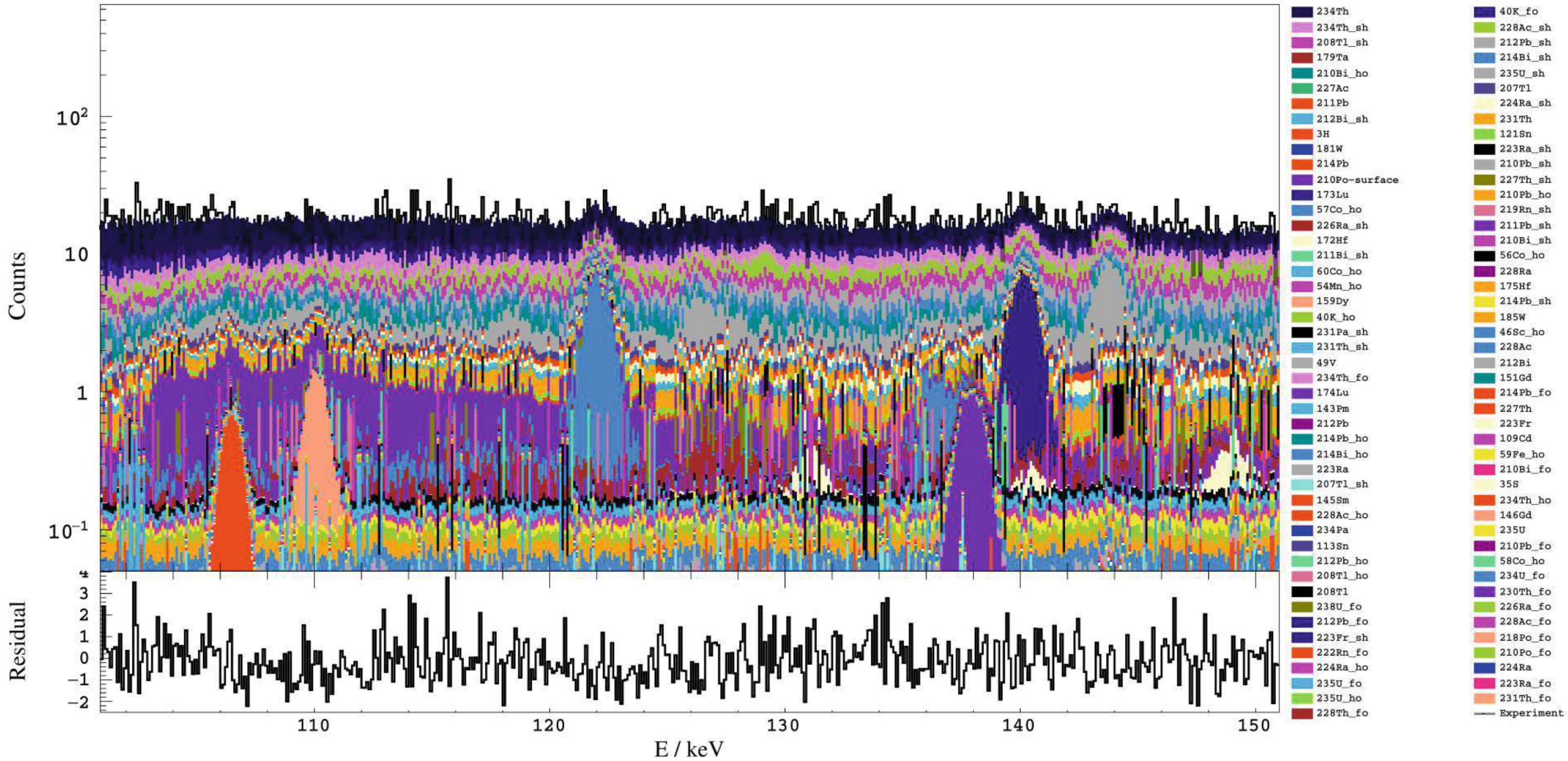

Figure A.6: Fit of simulated energy deposition templates (colored, filled histograms) including a template for surface roughness and contamination by ^{210}Po, following a distribution, to the measured data (black, open histogram) of TUM40, done with Bliss [12, 60]. The energy deposition of the widened ^{206}Pb peak (~ 103 keV) is colored in purple. Origin: Figure 6.8

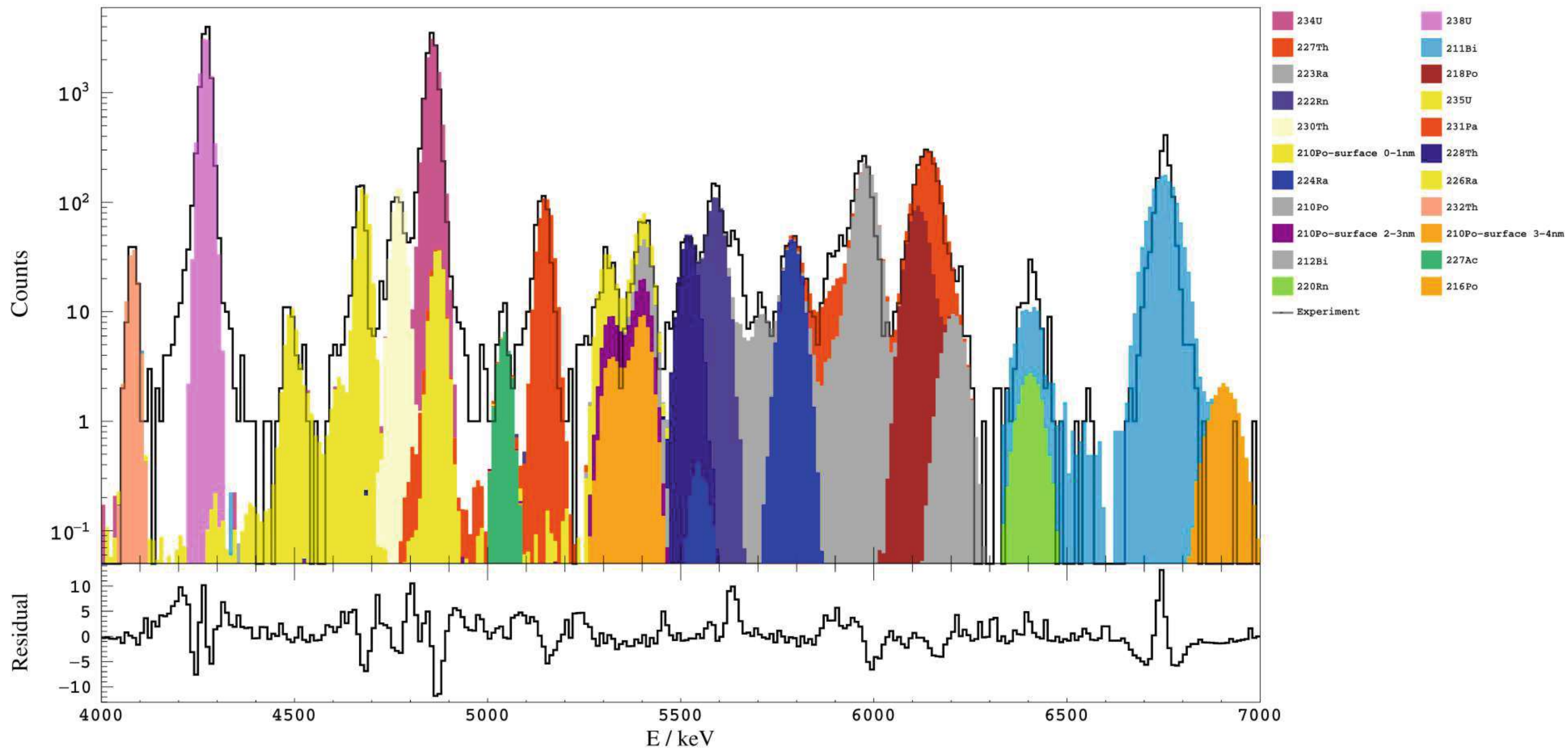

Figure A.7: Simulated spectra caused by α-decaying bulk- and surface-contaminants (colored, filled histograms) fitted [12, 66] to experimental data (black, open histogram) of CRESST's TUM40 detector [84] using Bliss. Several templates for surface roughness contamination are modelled by uniformly placing ^{210}Po nuclei in different 1 nm thick layers shifted to different depths in the range of nm below the rough crystal surface. Three layers from 0 to 1 nm, 2 to 3 nm and 3 to 4 nm are visible. Origin: Figure 6.10

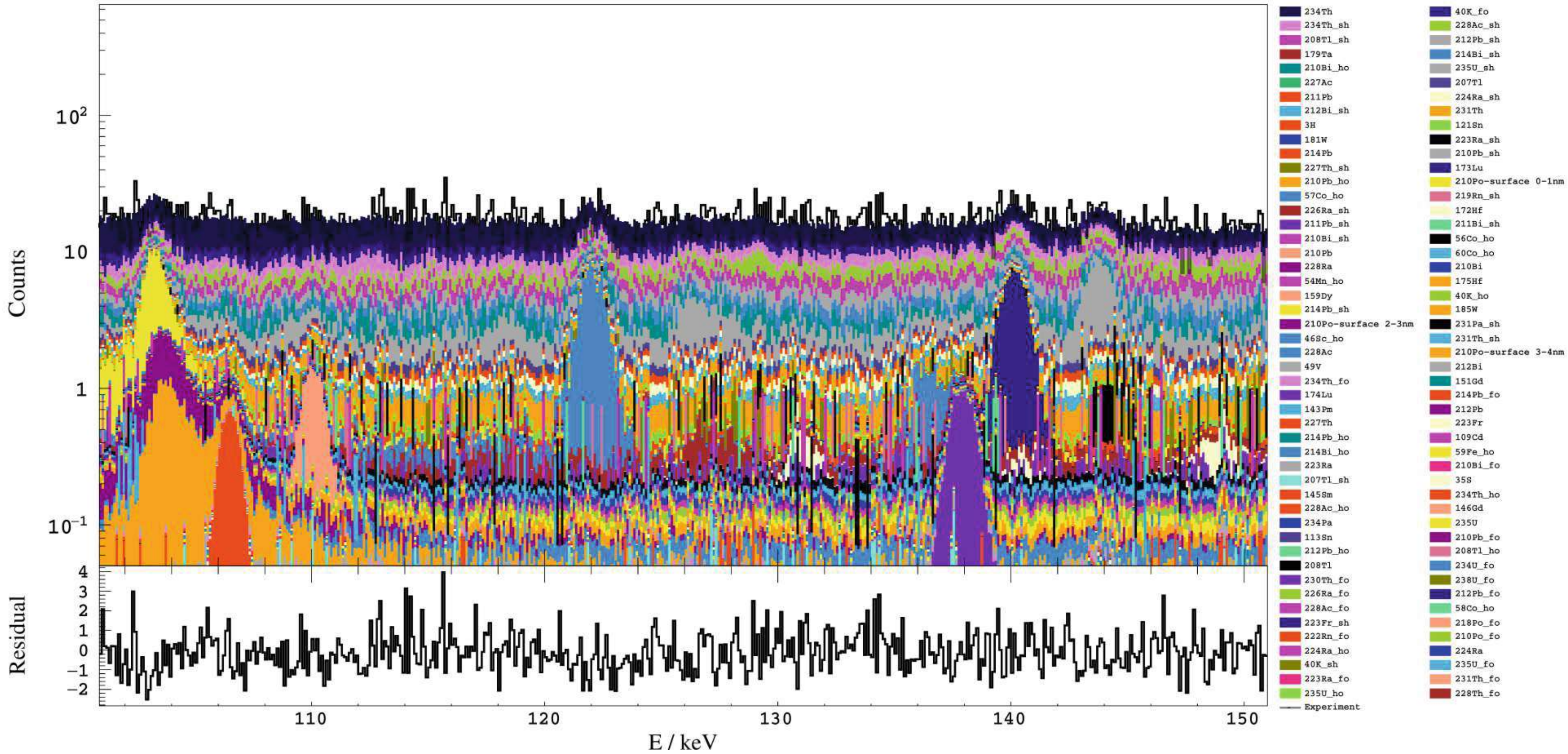

Figure A.8: Simulated spectra caused by α-decaying bulk- and surface-contaminants (colored, filled histograms) fitted [12, 66] to experimental data (black, open histogram) of CRESST's TUM40 detector [84] using Bliss. Several templates for surface roughness contamination are modelled by uniformly placing ^{210}Po nuclei in different 1 nm thick layers shifted to different depths in the range of nm below the rough crystal surface. Three layers from 0 to 1 nm, 2 to 3 nm and 3 to 4 nm are visible. Origin: Figure 6.10

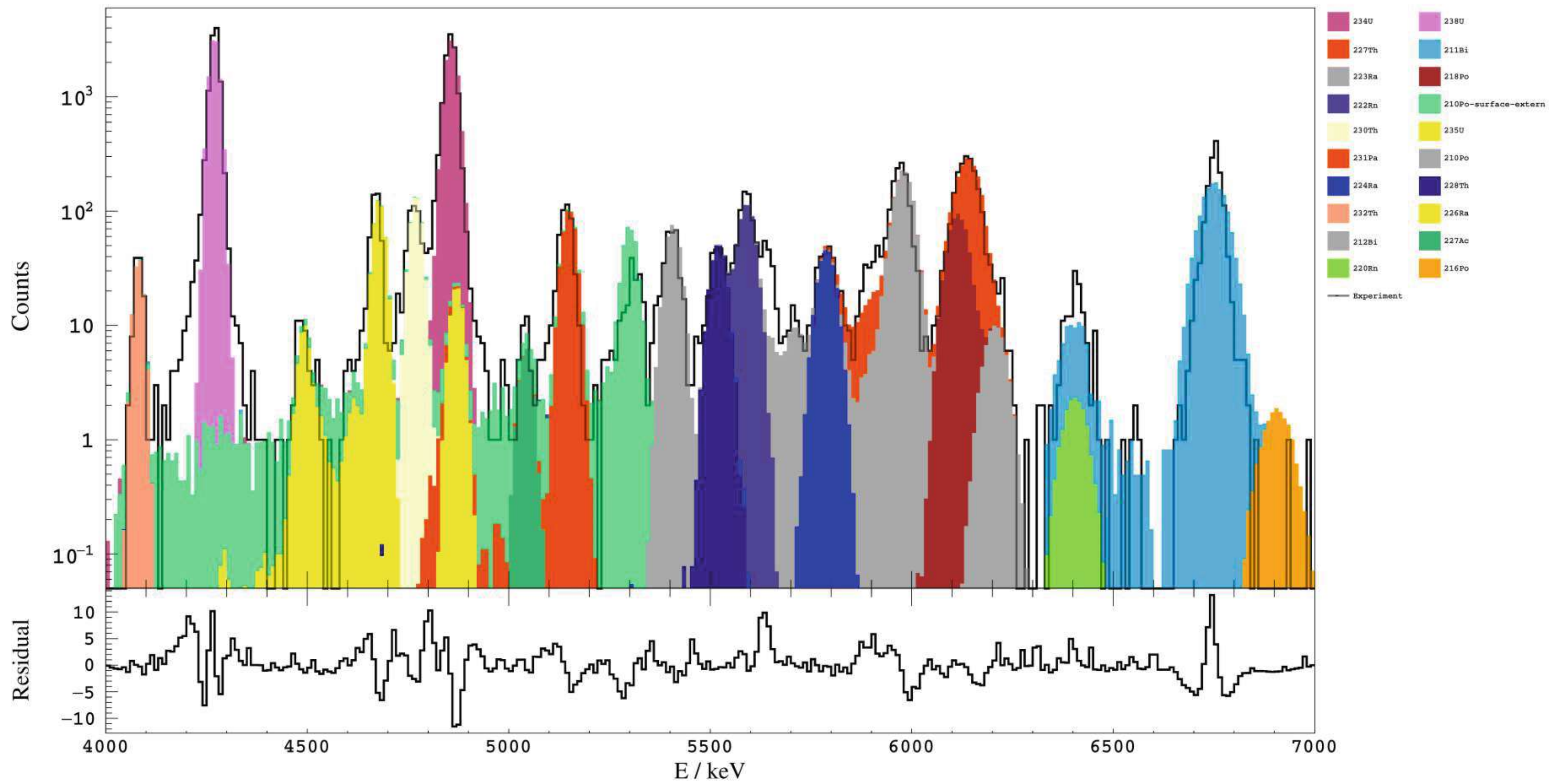

Figure A.9: Simulated spectra caused by α-decaying bulk- and surface contamination (colored, filled histograms) fitted [12, 66] to experimental data (black, open histogram) of CRESST's TUM40 detector [84]. The surface contamination of ^{210}Po is placed below the rough surface of an external crystal, following a distribution based on the ^{212}Rn decay chain. The rough, contaminated surface is facing the detector with a distance of ~ 1 cm. Origin: Figure 6.14

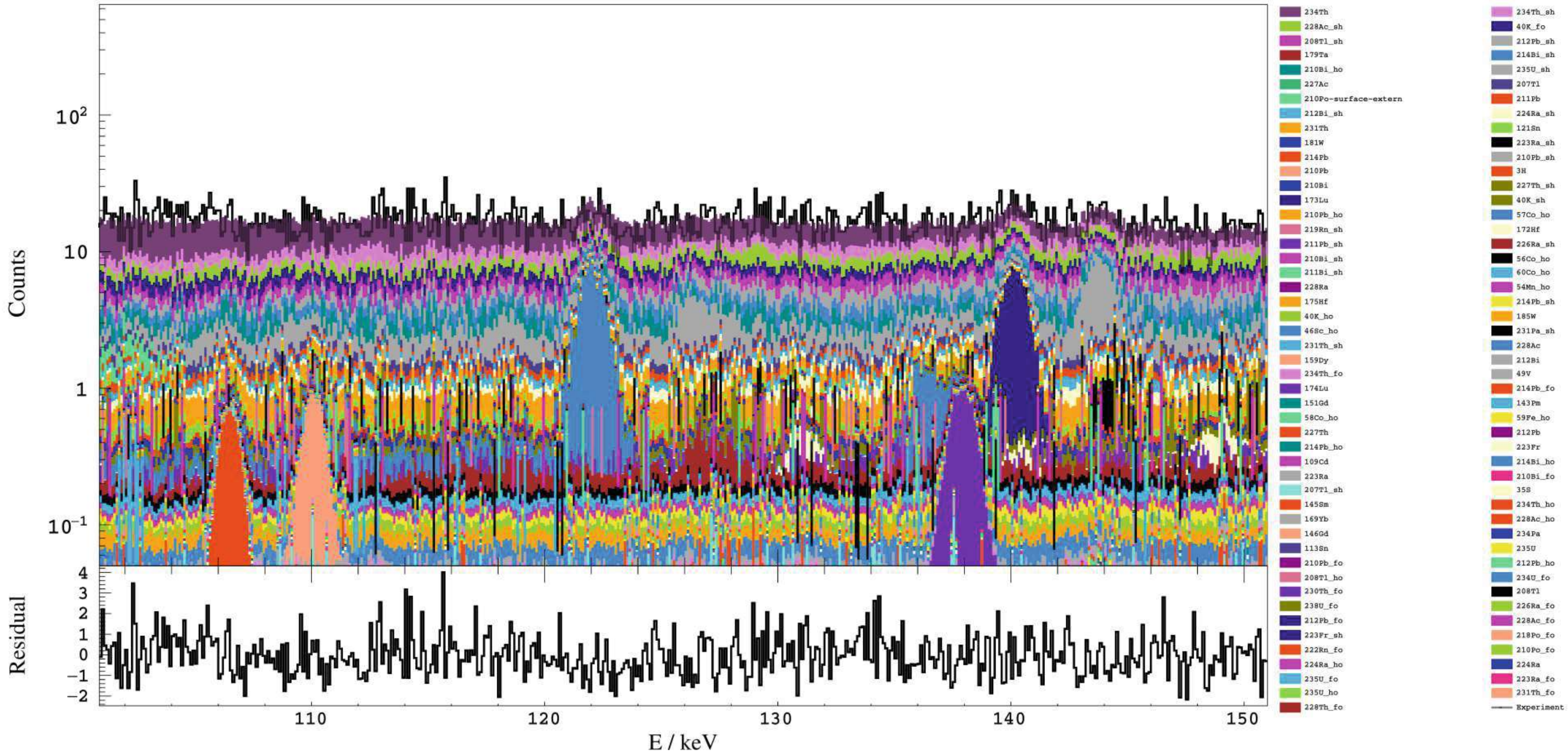

Figure A.10: Simulated spectra caused by α-decaying bulk- and surface contamination (colored, filled histograms) fitted [12, 66] to experimental data (black, open histogram) of CRESST's TUM40 detector [84]. The surface contamination of ^{210}Po is placed below the rough surface of an external crystal, following a distribution based on the ^{212}Rn decay chain. The rough, contaminated surface is facing the detector with a distance of $\sim 1\,$cm. Origin: Figure 6.14

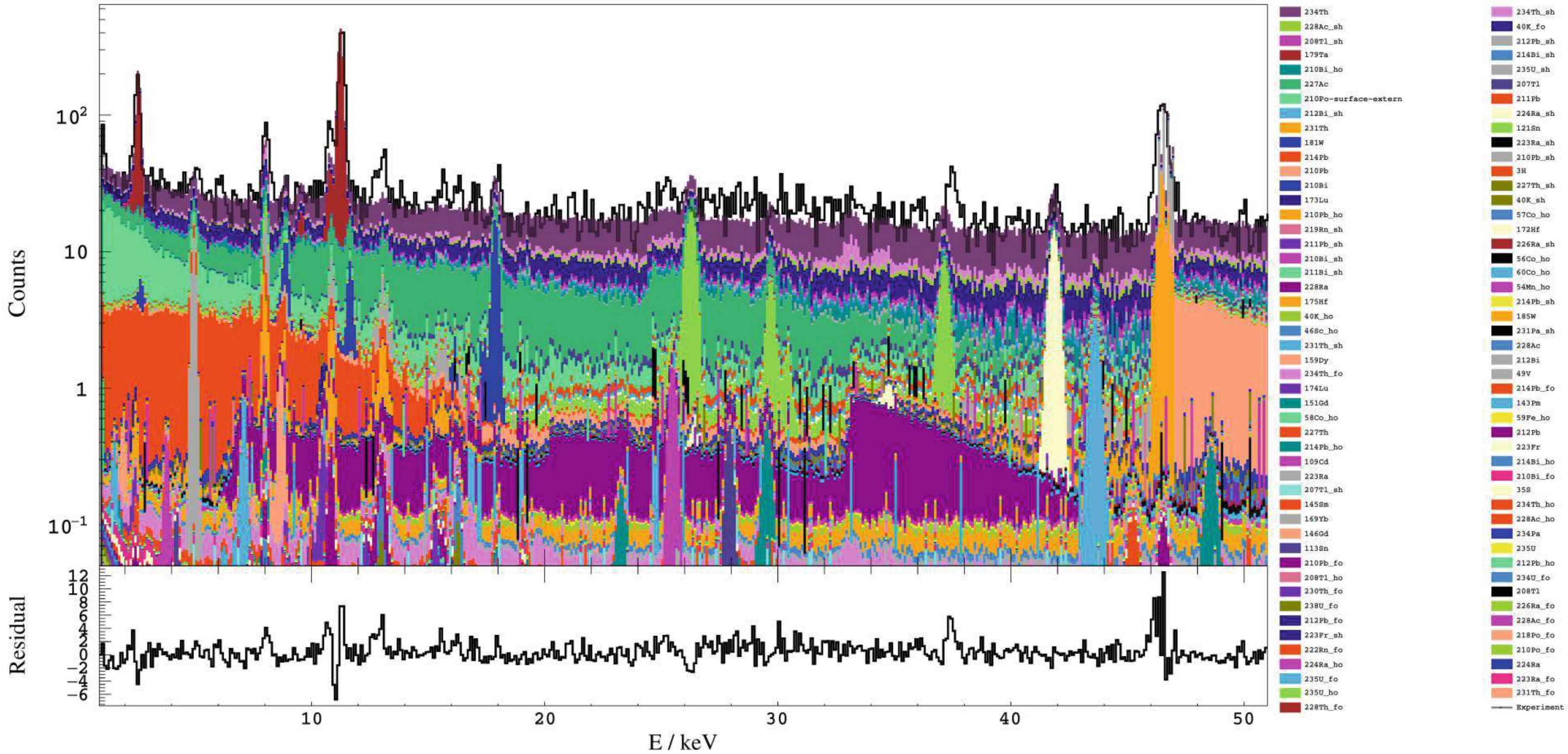

Figure A.11: Simulated spectra caused by α-decaying bulk- and surface contamination (colored, filled histograms) fitted [12, 66] to experimental data (black, open histogram) of CRESST's TUM40 detector [84]. The surface contamination of ^{210}Po is placed below the rough surface of an external crystal, following a distribution based on the ^{212}Rn decay chain. The rough, contaminated surface is facing the detector with a distance of $\sim 1\,$cm. Origin: Figure 6.14

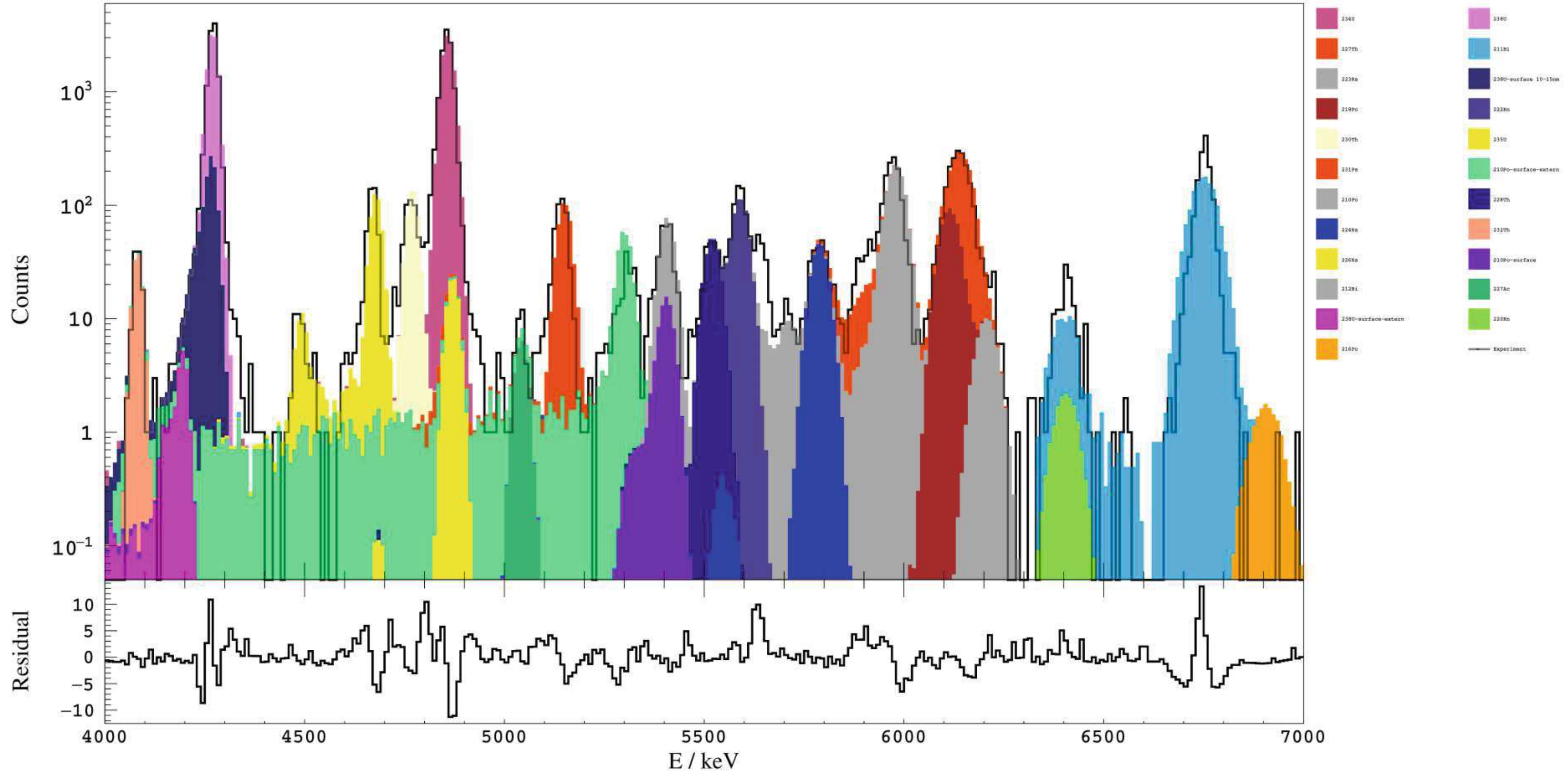

Figure A.12: Simulated spectra caused by α-decaying bulk- and surface contamination (colored, filled histograms) fitted [12, 66] to experimental data (black, open histogram) of CRESST's TUM40 detector [84]. Surface contamination of ^{238}U is uniformly placed in a layer of 15 nm below the rough surface of the external crystal and in three layers from 0-5 nm, 5-10 nm and 10-15 nm below the rough surface of the detector crystal. All rough surfaces are represented by 5 µm high and wide spikes. Origin: Figure 6.17

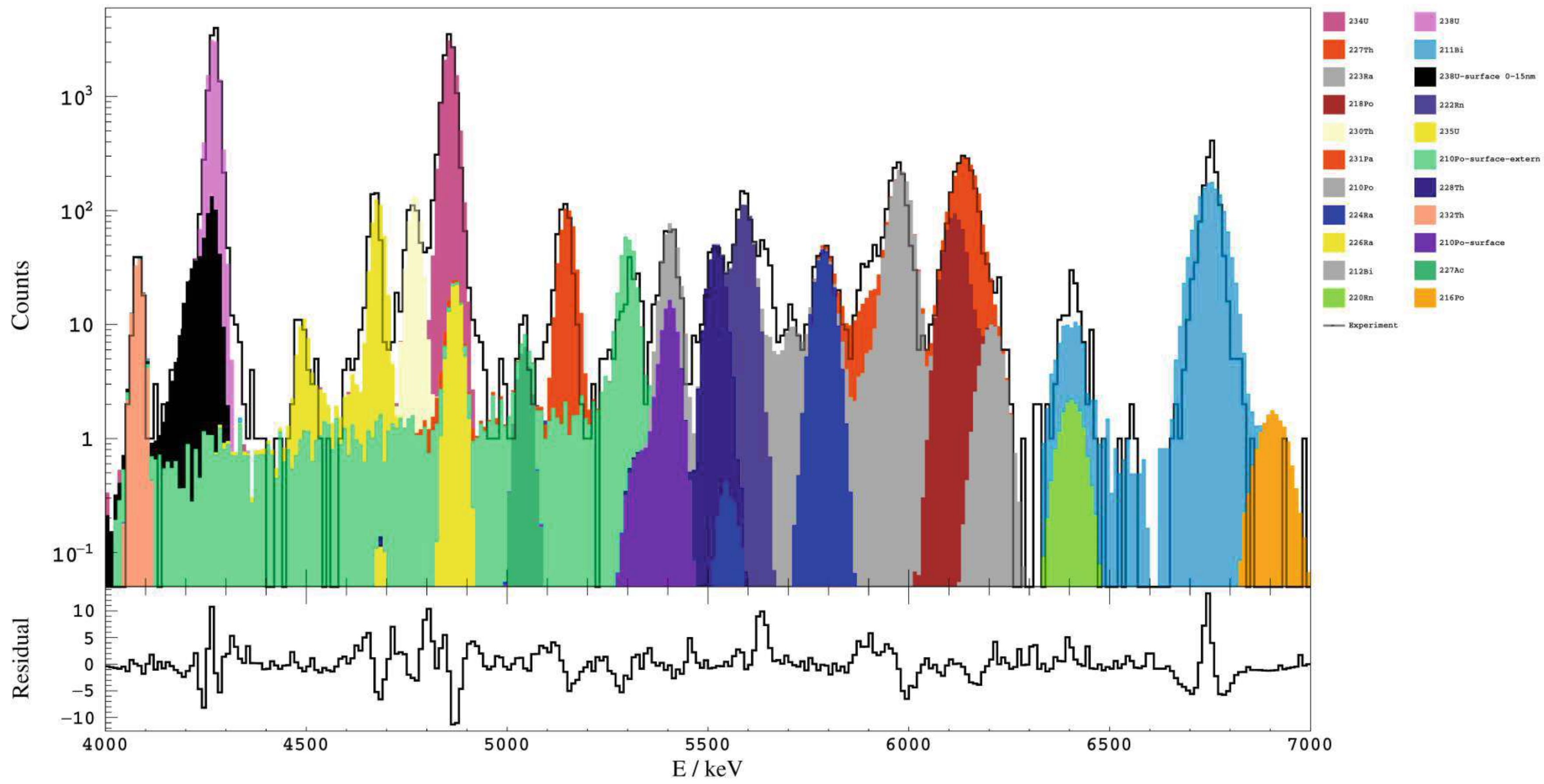

Figure A.13: Simulated spectra caused by α-decaying bulk- and surface contamination (colored, filled histograms) fitted [12, 66] to experimental data (black, open histogram) of CRESST's TUM40 detector [84]. Four surface contamination energy deposition templates are added. Two for the nuclei ^{210}Po and ^{238}U. Each adding a surface contamination from an external rough surface facing the target detector with a distance of 0.5 cm and a surface contamination of the target crystal itself. ^{210}Po is placed below the rough surface following a simulated ^{210}Po distribution from the ^{222}Rn decay chain. ^{238}U is uniformly placed in a 15 nm thick layer below the rough surface. The rough surfaces are emulated by spikes of 5 µm height and width. Origin: Figure 6.18

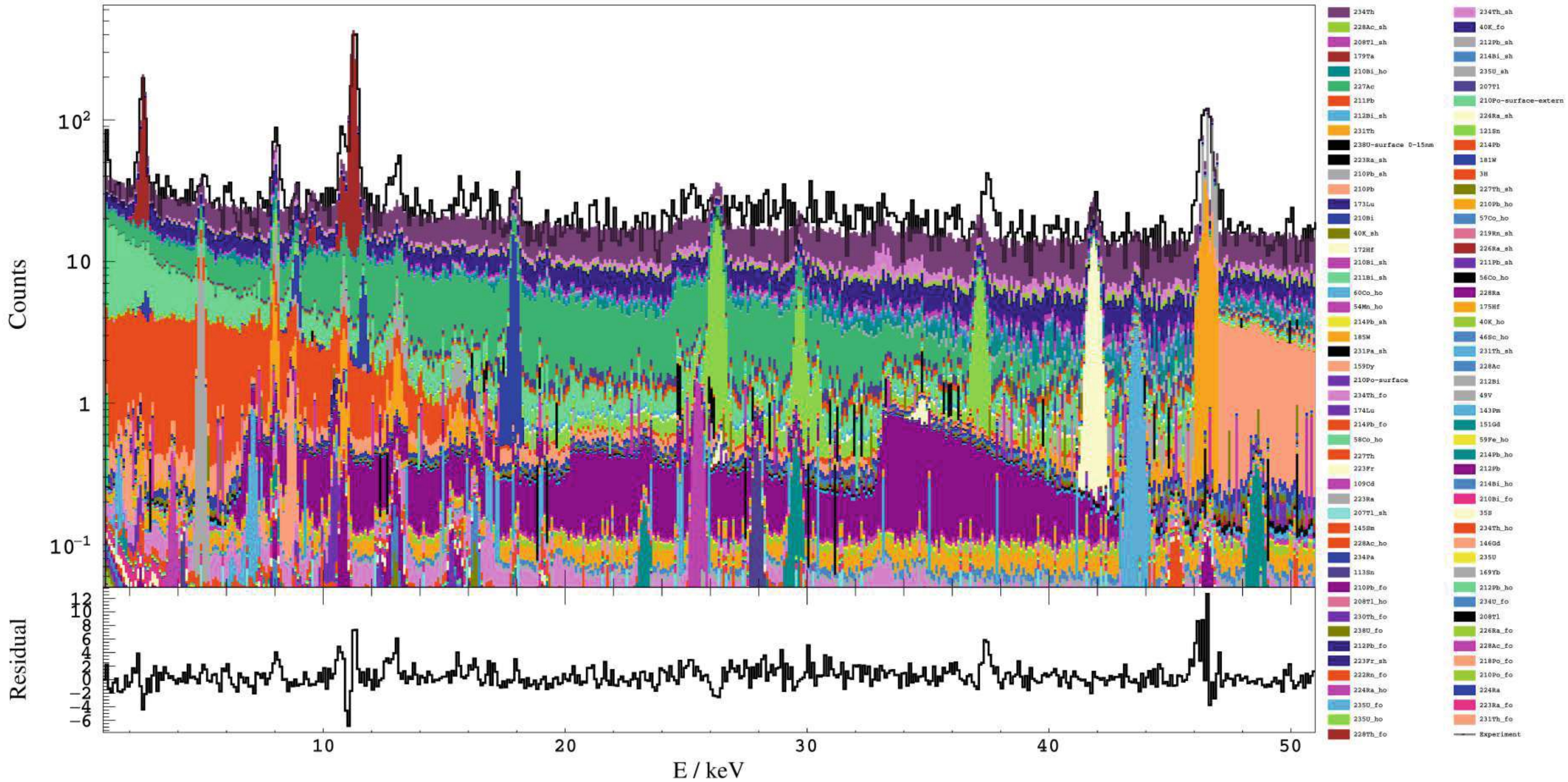

Figure A.14: Simulated spectra caused by α-decaying bulk- and surface contamination (colored, filled histograms) fitted [12, 66] to experimental data (black, open histogram) of CRESST's TUM40 detector [84]. Four surface contamination energy deposition templates are added. Two for the nuclei ^{210}Po and ^{238}U. Each adding a surface contamination from an external rough surface facing the target detector with a distance of 0.5 cm and a surface contamination of the target crystal itself. ^{210}Po is placed below the rough surface following a simulated ^{210}Po distribution from the ^{222}Rn decay chain. ^{238}U is uniformly placed in a 15 nm thick layer below the rough surface. The rough surfaces are emulated by spikes of 5 µm height and width. Origin: Figure 6.18

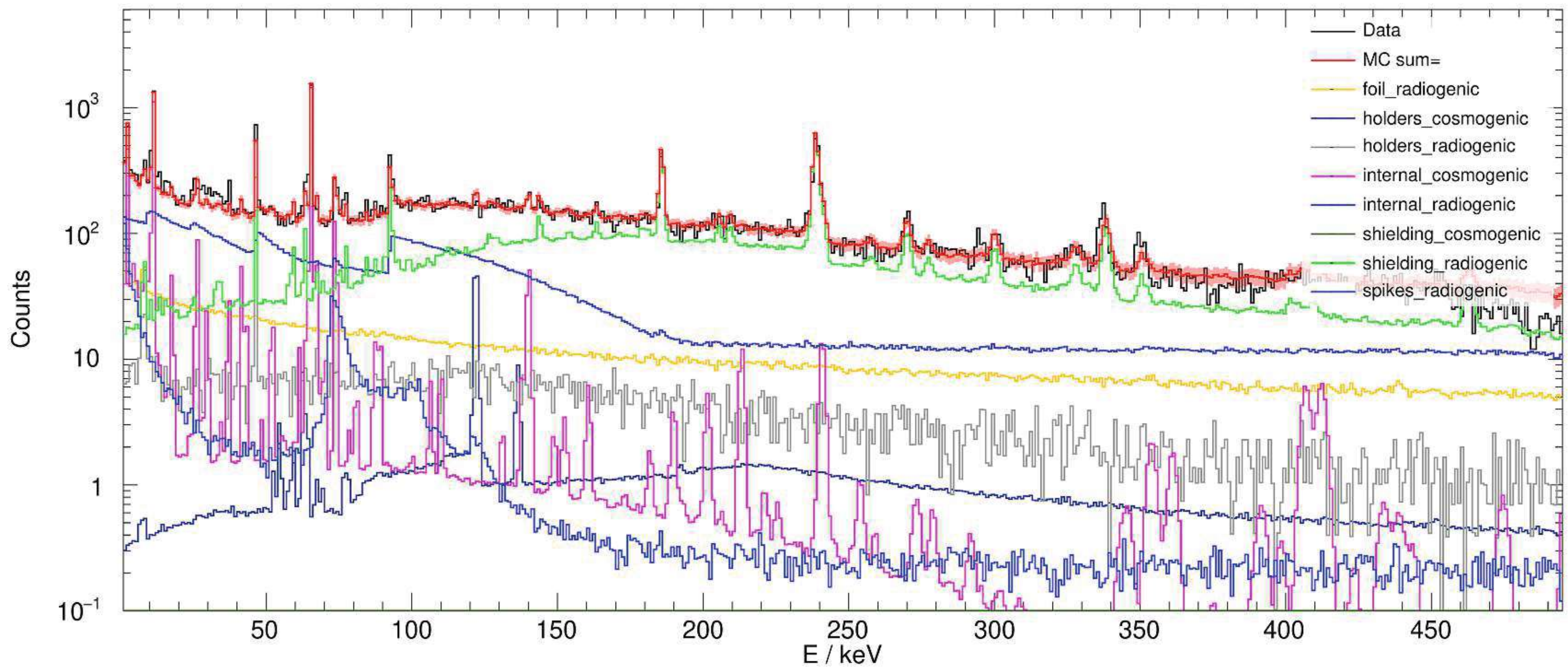

Figure A.15: Simulated spectra caused by α-decaying bulk- and surface contamination (colored, filled histograms) fitted [12, 66] to experimental data (black, open histogram) of CRESST's TUM40 detector [84]. Four surface contamination energy deposition templates are added. Two for the nuclei ^{210}Po and ^{238}U. Each adding a surface contamination from an external rough surface facing the target detector with a distance of 0.5 cm and a surface contamination of the target crystal itself. ^{210}Po is placed below the rough surface following a simulated ^{210}Po distribution from the ^{222}Rn decay chain. ^{238}U is uniformly placed in a 15 nm thick layer below the rough surface. The rough surfaces are emulated by spikes of 5 µm height and width. The figure shows the contributions grouped to different sources for the lower energy range. Origin: Figure 6.18

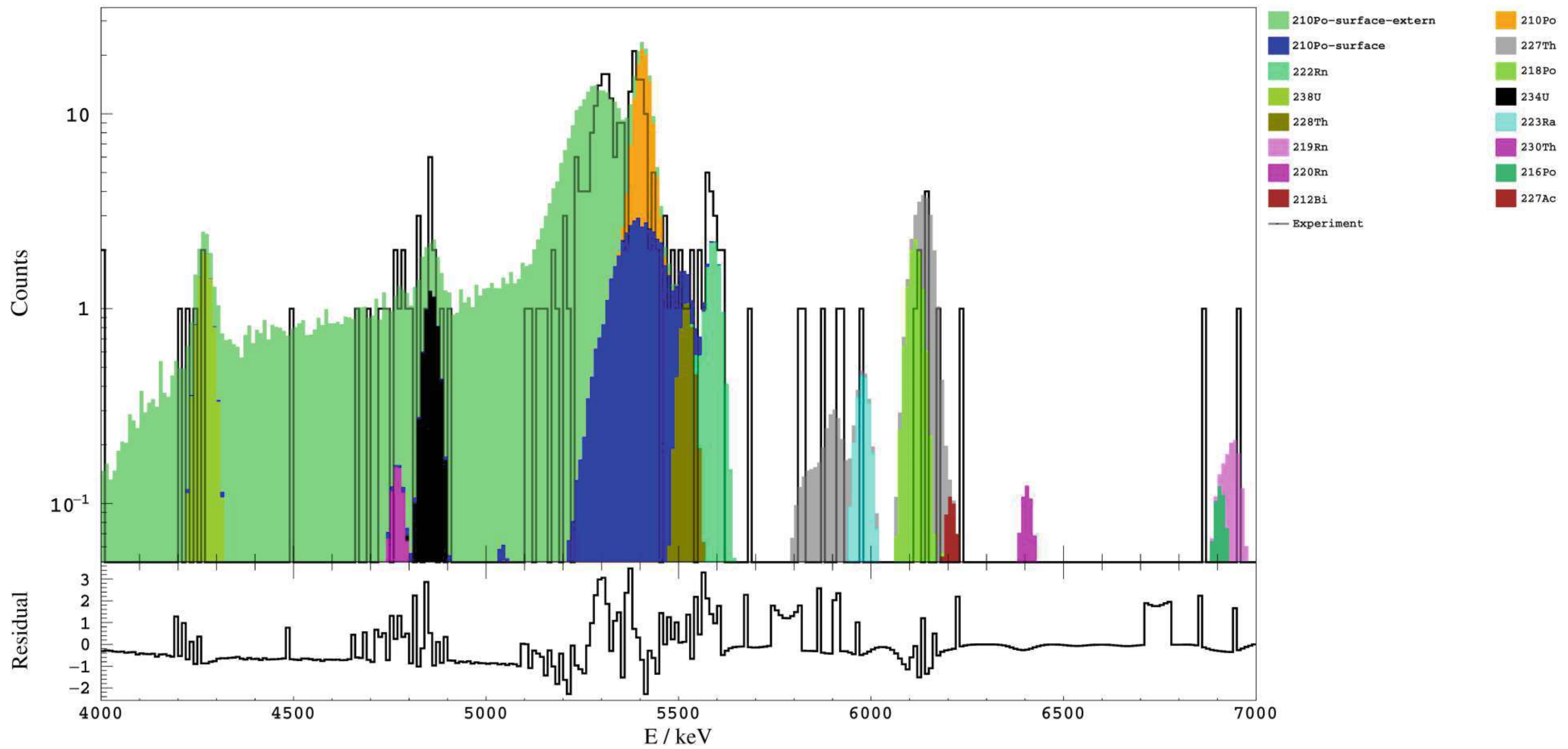

Figure A.16: Simulated spectra caused by bulk- and surface contamination (colored, filled histograms) fitted [12, 66] to experimental data (black, open histogram) of CRESST's TUM93A detector. Four surface contamination energy deposition templates are added. Two for the nuclei ^{210}Po and ^{238}U. Each adding a surface contamination from an external rough surface facing the target detector with a distance of 0.5 cm and a surface contamination of the target crystal itself. ^{210}Po is placed below the rough surface following a simulated ^{210}Po distribution from the ^{222}Rn decay chain. ^{238}U is uniformly placed in a 15 nm thick layer below the rough surface. The rough surfaces are emulated by spikes of 5 µm height and width. Origin: Figure 6.19

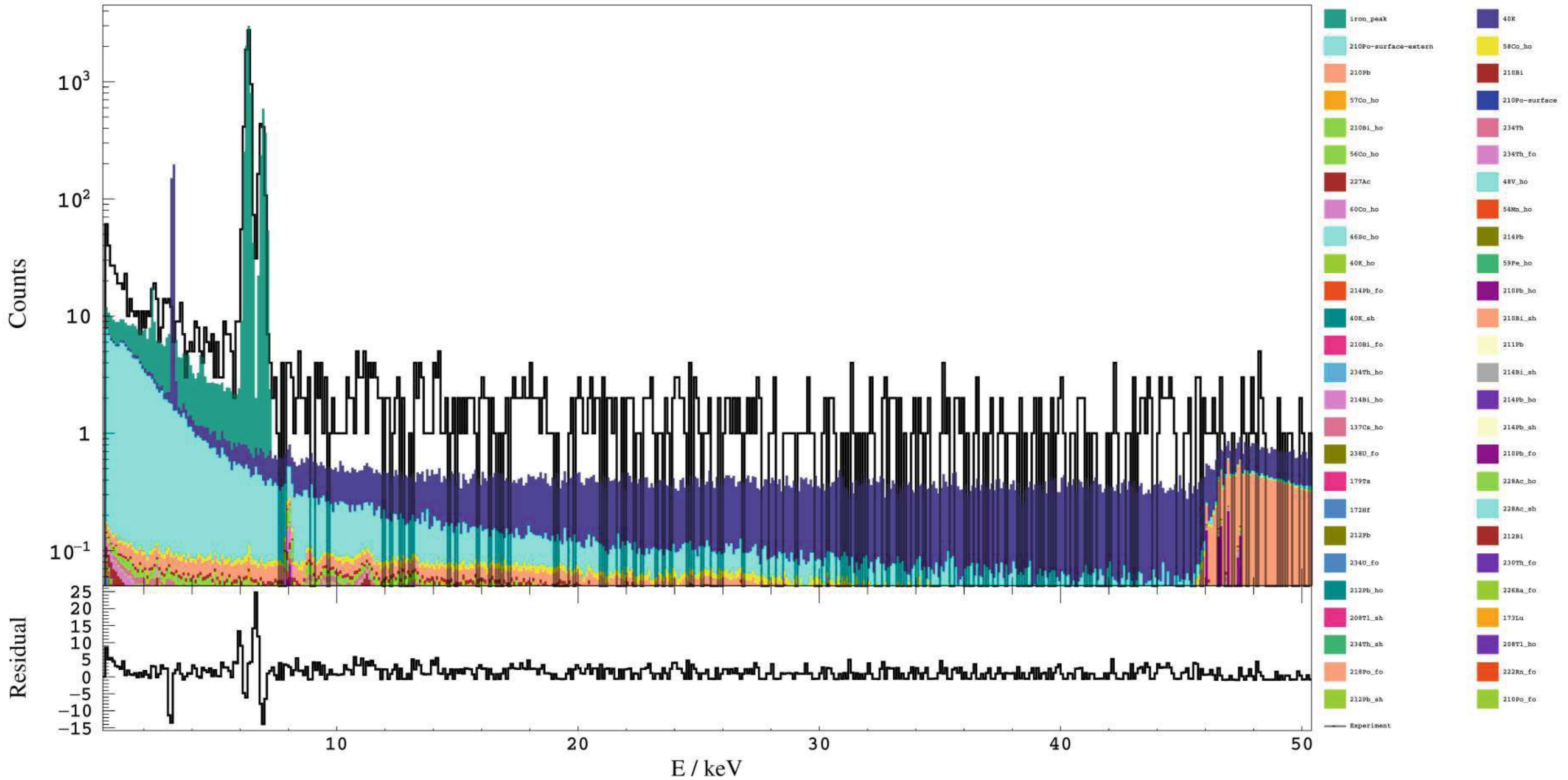

Figure A.17: Simulated spectra caused by bulk- and surface contamination (colored, filled histograms) fitted [12, 66] to experimental data (black, open histogram) of CRESST's TUM93A detector. Four surface contamination energy deposition templates are added. Two for the nuclei ^{210}Po and ^{238}U. Each adding a surface contamination from an external rough surface facing the target detector with a distance of 0.5 cm and a surface contamination of the target crystal itself. ^{210}Po is placed below the rough surface following a simulated ^{210}Po distribution from the ^{222}Rn decay chain. ^{238}U is uniformly placed in a 15 nm thick layer below the rough surface. The rough surfaces are emulated by spikes of 5 µm height and width. Origin: Figure 6.19

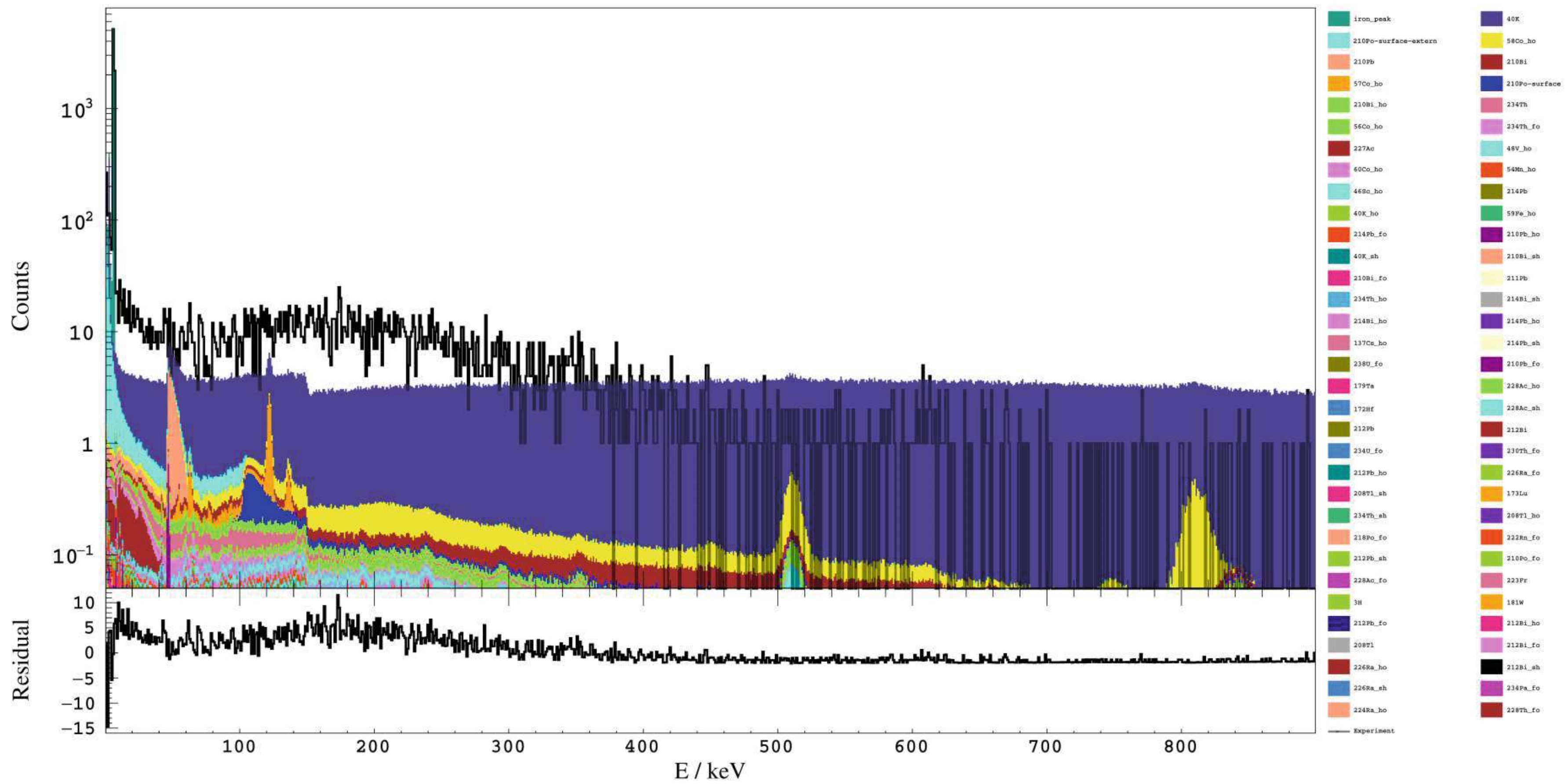

Figure A.18: Simulated spectra caused by bulk- and surface contamination (colored, filled histograms) fitted [12, 66] to experimental data (black, open histogram) of CRESST's TUM93A detector. Four surface contamination energy deposition templates are added. Two for the nuclei ^{210}Po and ^{238}U. Each adding a surface contamination from an external rough surface facing the target detector with a distance of 0.5 cm and a surface contamination of the target crystal itself. ^{210}Po is placed below the rough surface following a simulated ^{210}Po distribution from the ^{222}Rn decay chain. ^{238}U is uniformly placed in a 15 nm thick layer below the rough surface. The rough surfaces are emulated by spikes of 5 µm height and width. Origin: Figure 6.19

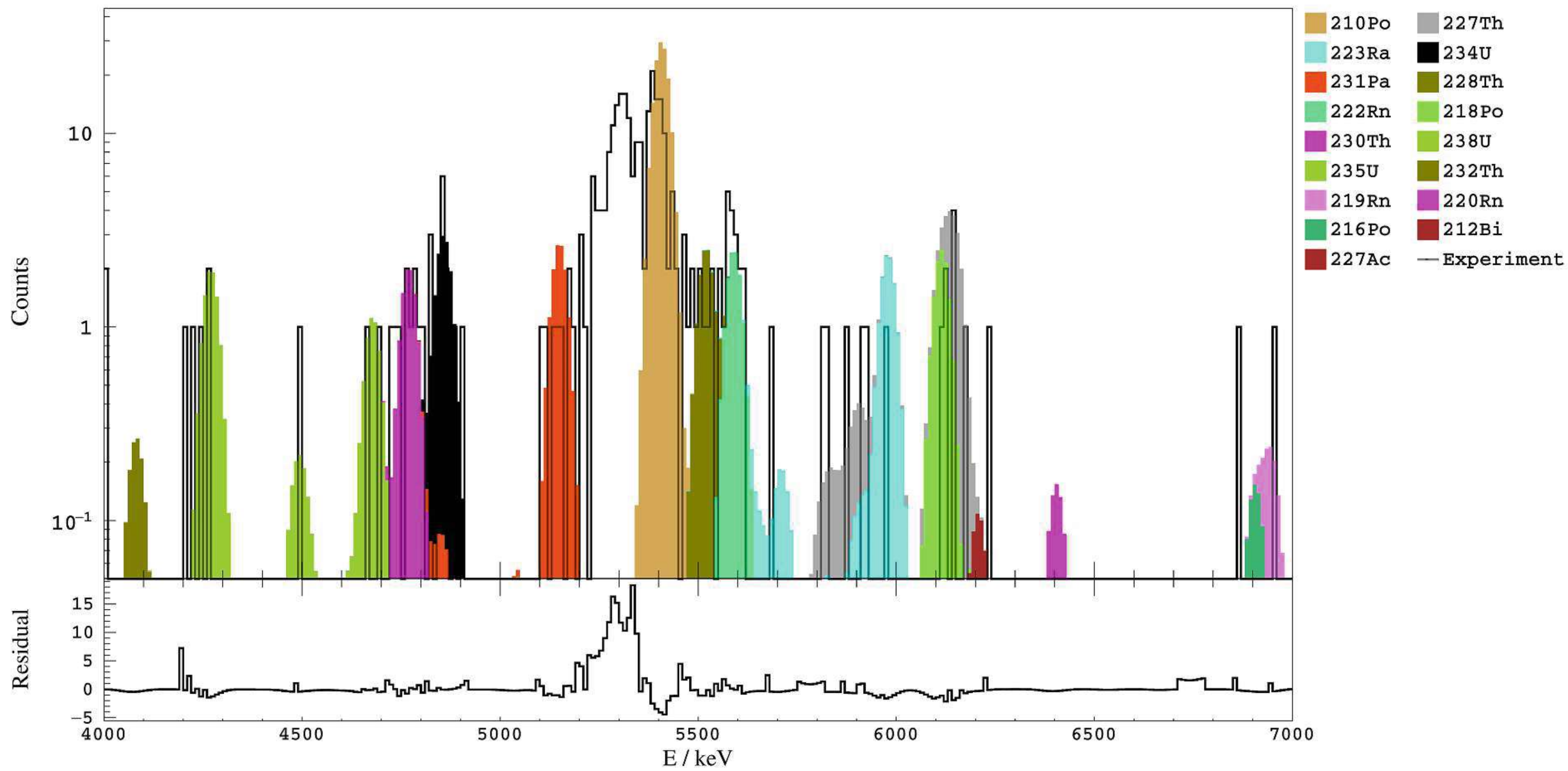

Figure A.19: Simulated spectra caused by bulk- and surface contamination (colored, filled histograms) fitted [12, 66] to experimental data (black, open histogram) of CRESST's TUM93A detector.

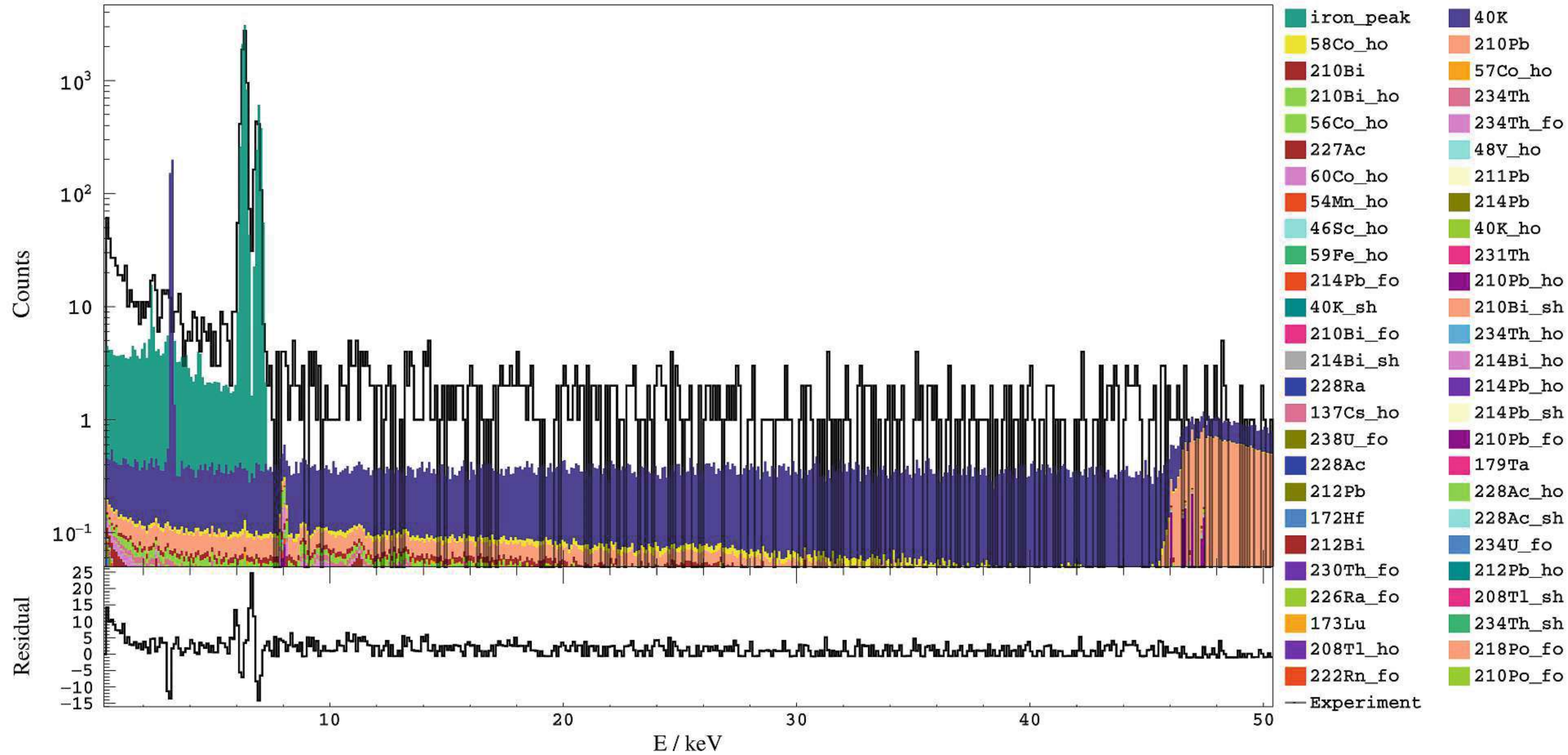

Figure A.20: Simulated spectra caused by bulk- and surface contamination (colored, filled histograms) fitted [12, 66] to experimental data (black, open histogram) of CRESST's TUM93A detector.

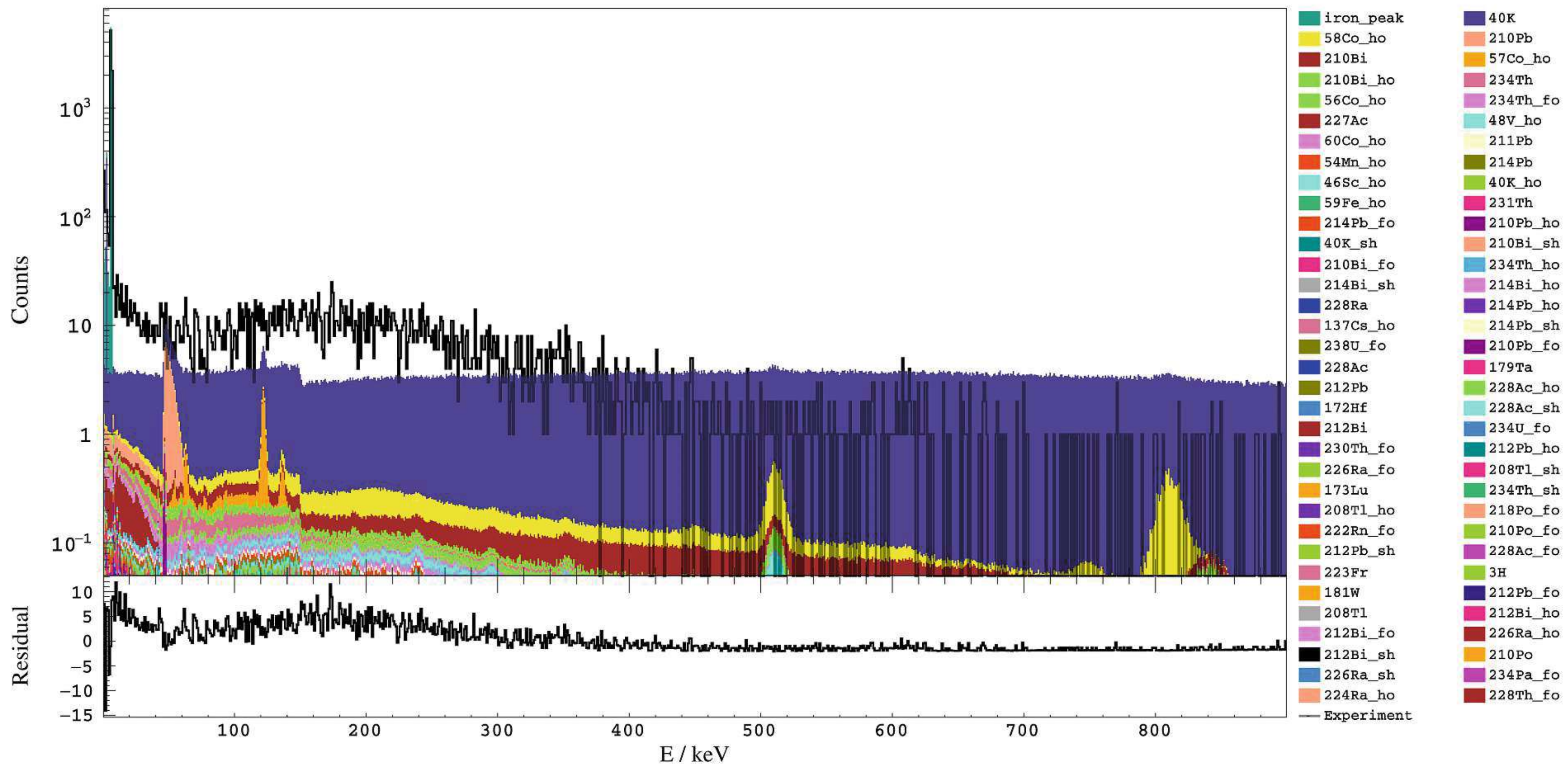

Figure A.21: Simulated spectra caused by bulk- and surface contamination (colored, filled histograms) fitted [12, 66] to experimental data (black, open histogram) of CRESST's TUM93A detector.

B Additional Figures

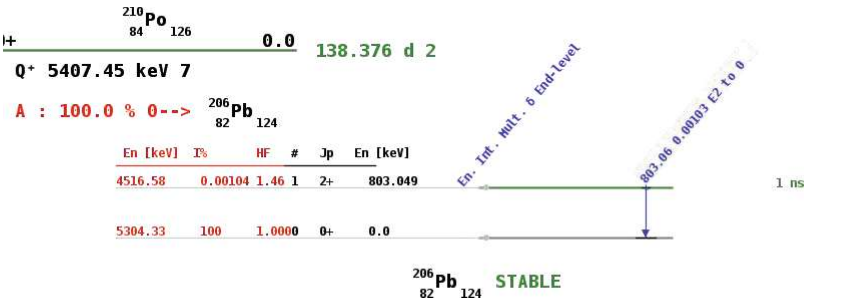

Figure B.1: The ^{210}Po decay has a Q value of 5407.45 keV. Both decay remnants, α particle and ^{206}Pb have almost always the same kinetic energy. Figure take from [90].

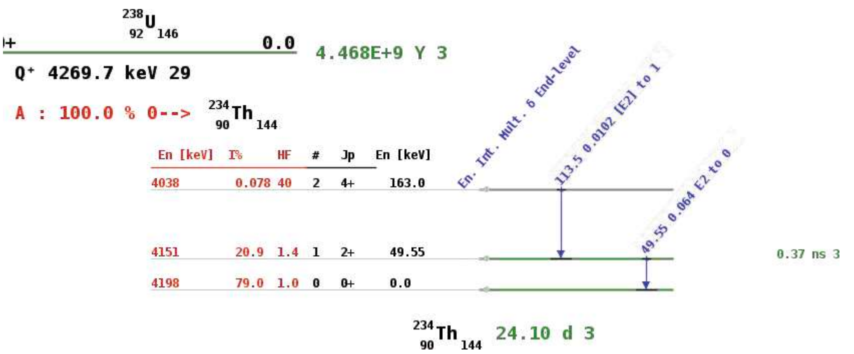

Figure B.2: The ^{238}U decay has a Q value of 4269.7 keV, however the α particle and ^{234}Th can have different energies after the decay due to possible excitation of ^{234}Th. Figure take from [90].

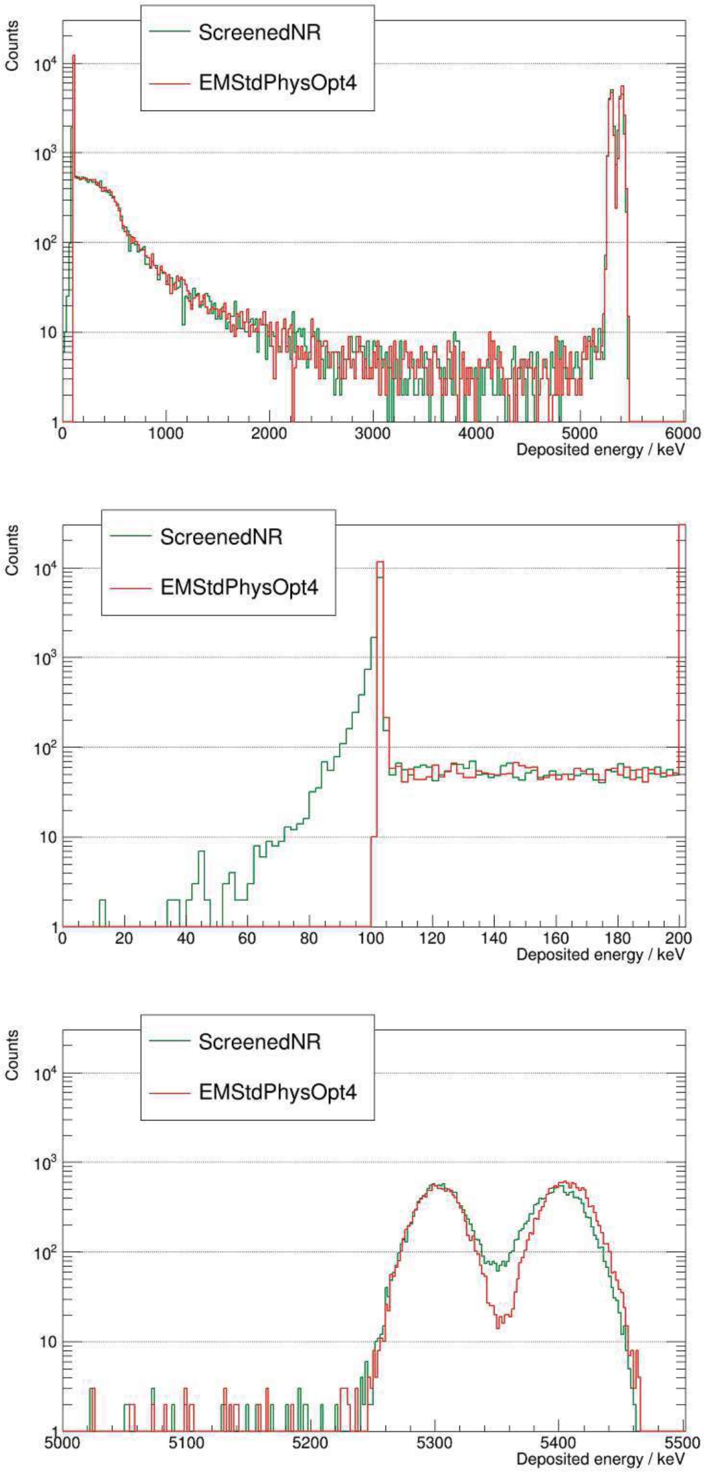

Figure B.3: 2e4 ^{210}Po are exactly placed the surface of 5 µm high and wide spikes of a $CaWO_4$ crystal. Two different physics implementations are used: ScreenedNuclearRecoil and EmStandardPhysicsOption_4. Detector resolution of TUM40 is applied to the data. Three different energy ranges are presented: 0-6000 keV (top), 0-200 keV (middle), and 5000-5500 keV (bottom).

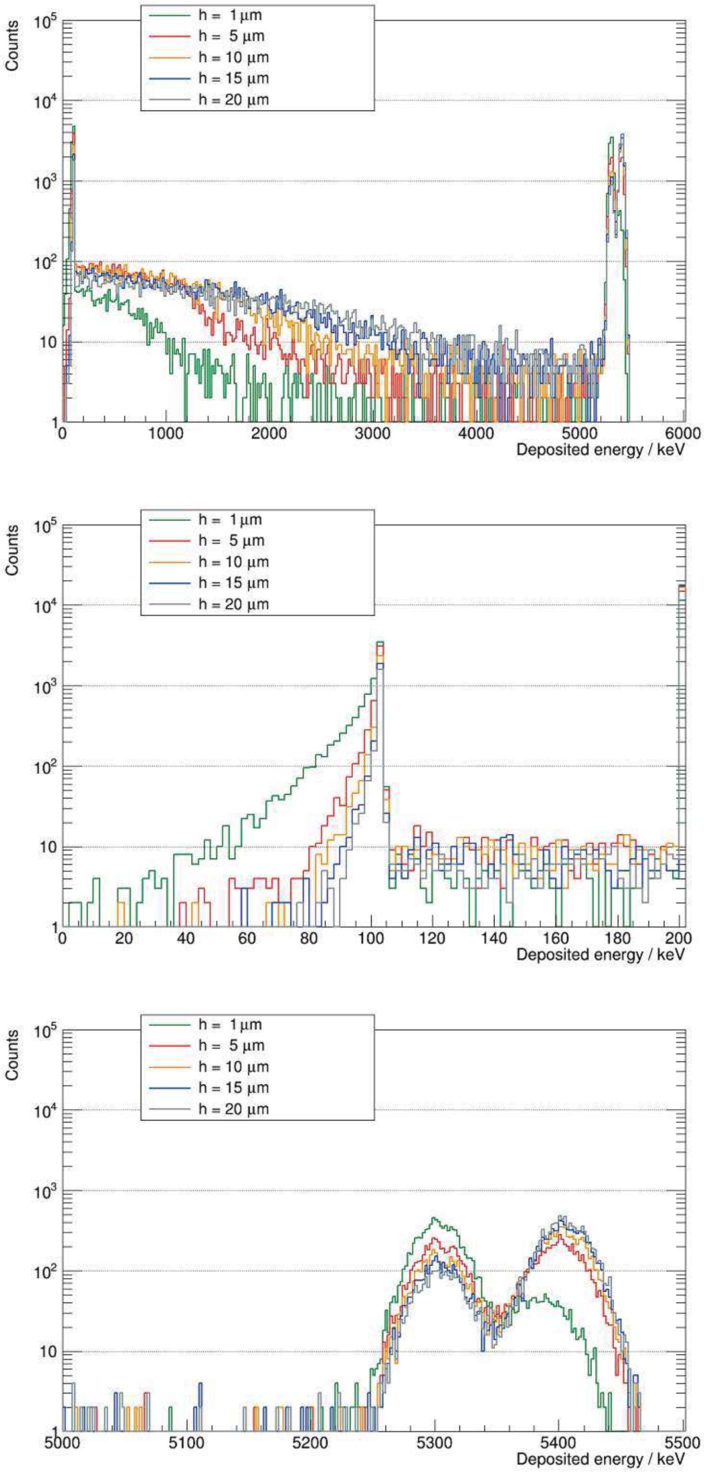

Figure B.4: 5e4 ^{210}Po are placed exactly at the rough surface of a $CaWO_4$ crystal. Five different spike heights h are simulated. Their width is fixed at 5 µm. Detector resolution of TUM40 is applied to the data. Three different energy ranges are presented: 0-6000 keV (top), 0-200 keV (middle), and 5000-5500 keV (bottom).

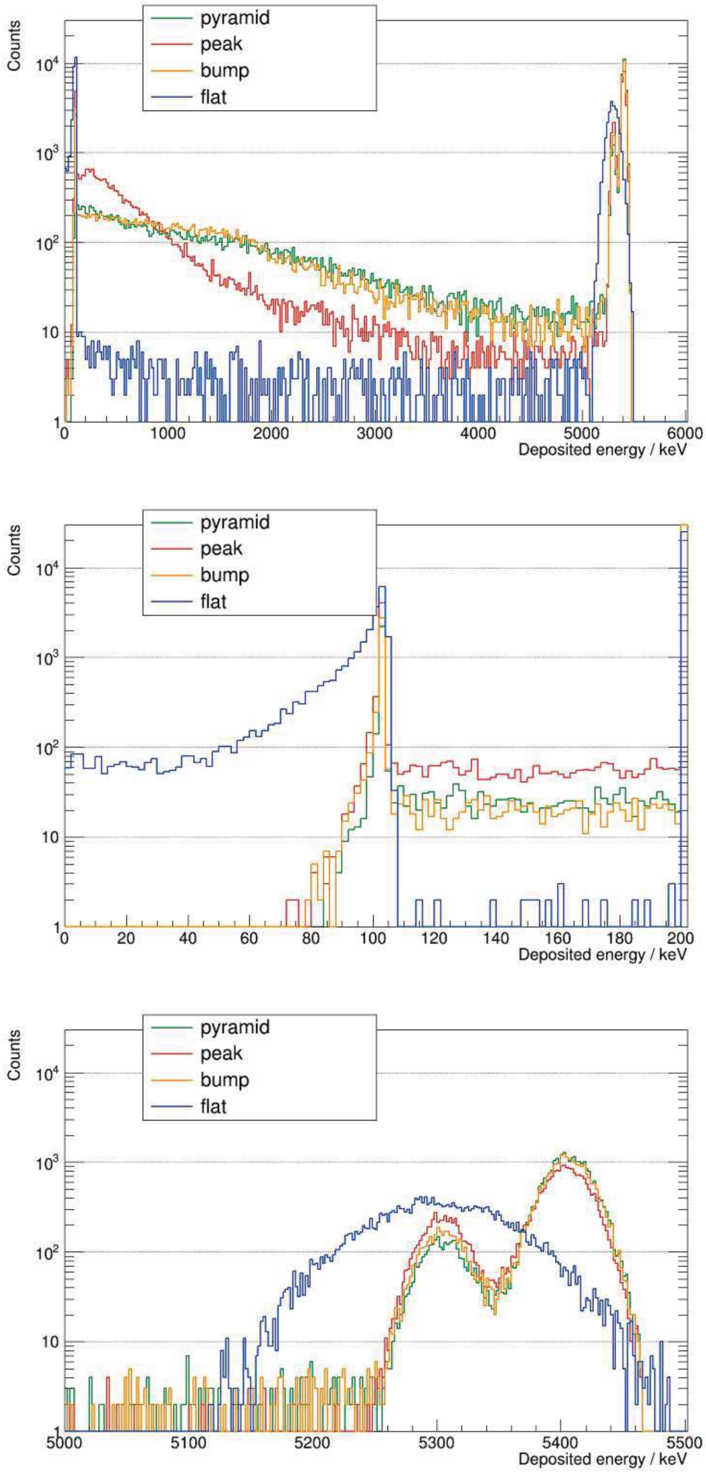

Figure B.5: 5e4 ^{210}Po nuclei placed on a rough surface with different spike forms of 10 µm height and width and a flat surface of a $CaWO_4$ crystal. Detector resolution of TUM40 is applied to the data. Three different energy ranges are presented: 0-6000 keV (top), 0-200 keV (middle), and 5000-5500 keV (bottom).

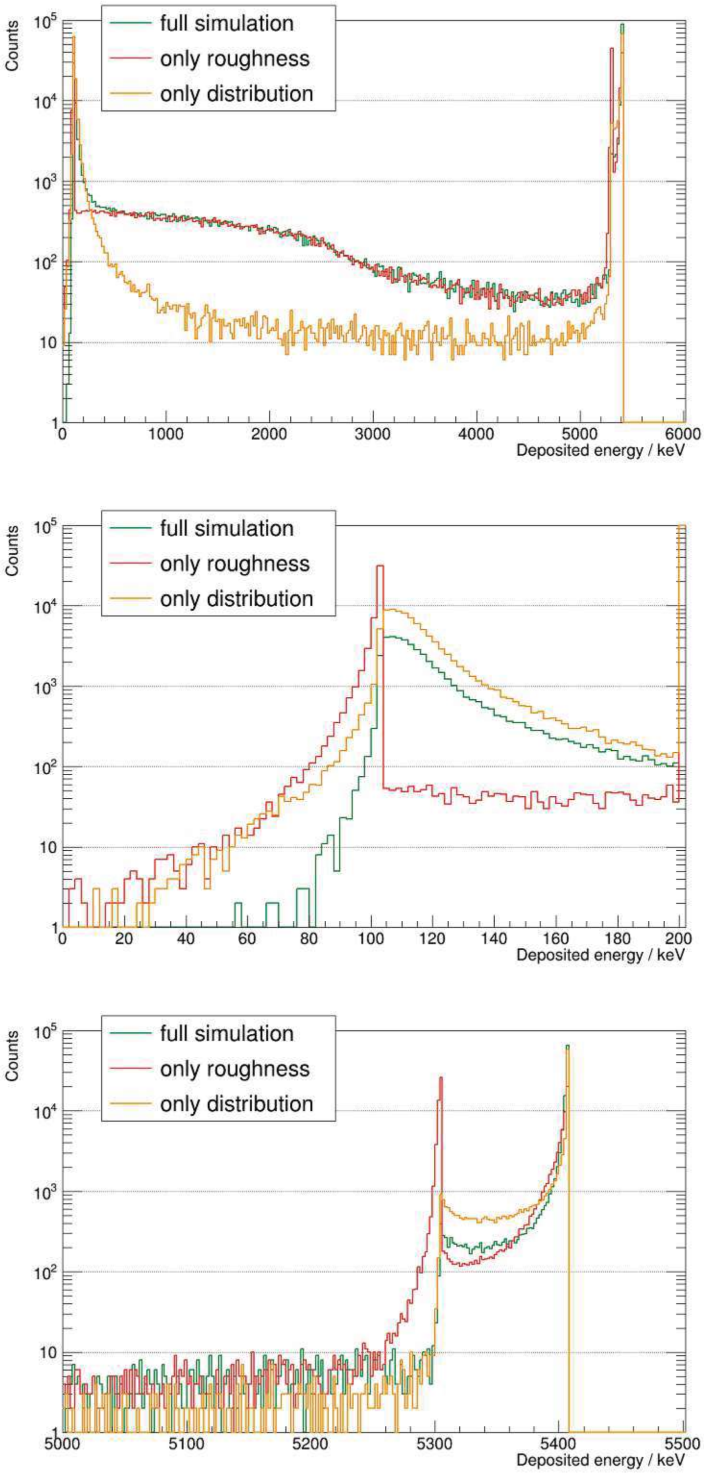

Figure B.6: 2e5 ^{210}Po are placed below the rough surface of a $CaWO_4$ crystal. For the placement of ^{210}Po a distribution was used. The distribution represents a simulated distribution of ^{210}Po below the surface from exposure to ^{222}Rn. The spikes have a height and width of 5 µm. Detector resolution of TUM40 was applied to the data. Three different energy ranges are presented: 0-6000 keV (top), 0-200 keV (middle), and 5000-5500 keV (bottom).

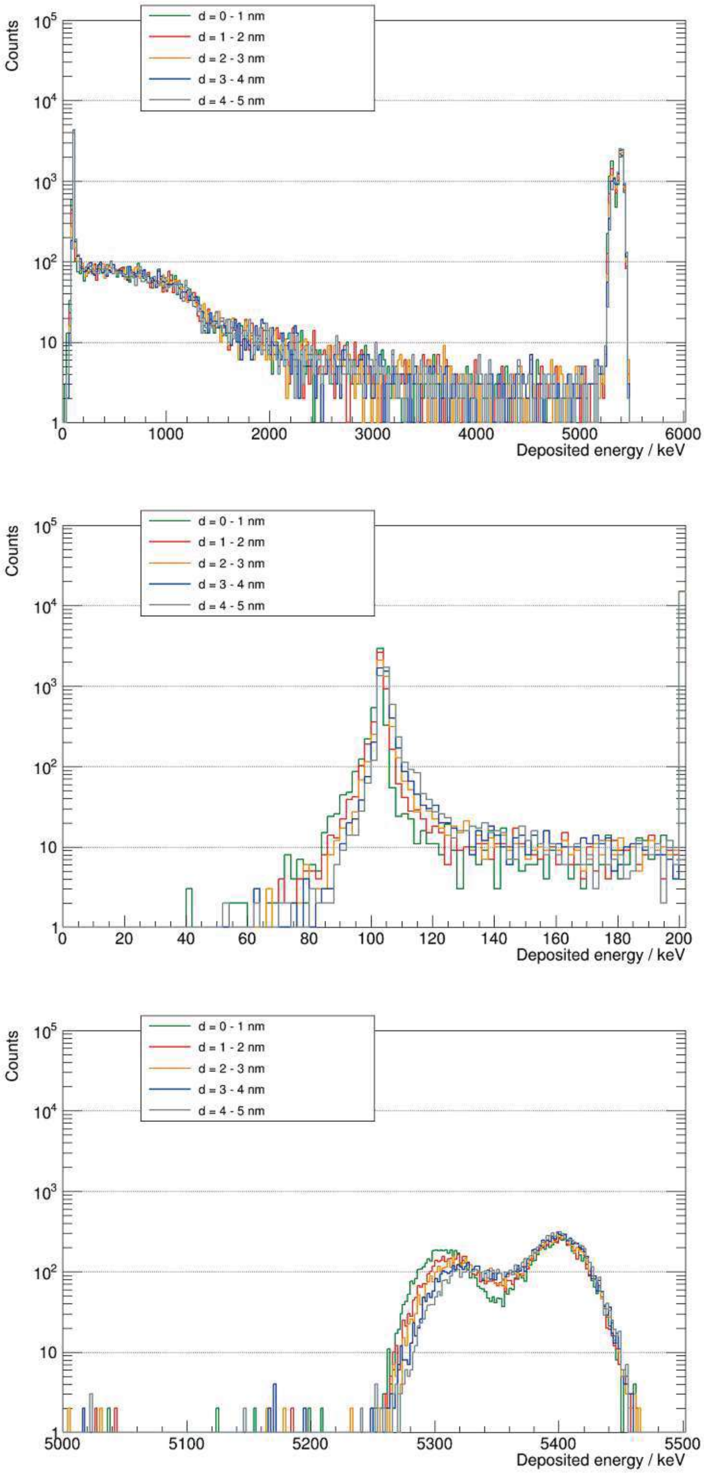

Figure B.7: 5e4 ^{210}Po are placed in different layers withing the depth d below the rough surface of a $CaWO_4$ crystal. Inside the layers the ^{210}Po are uniformly distributed. The spikes have a height and width of 5 µm. Five different layers are simulated. Detector resolution of TUM40 is applied to the data. Three different energy ranges are presented: 0-6000 keV (top), 0-200 keV (middle), and 5000-5500 keV (bottom).

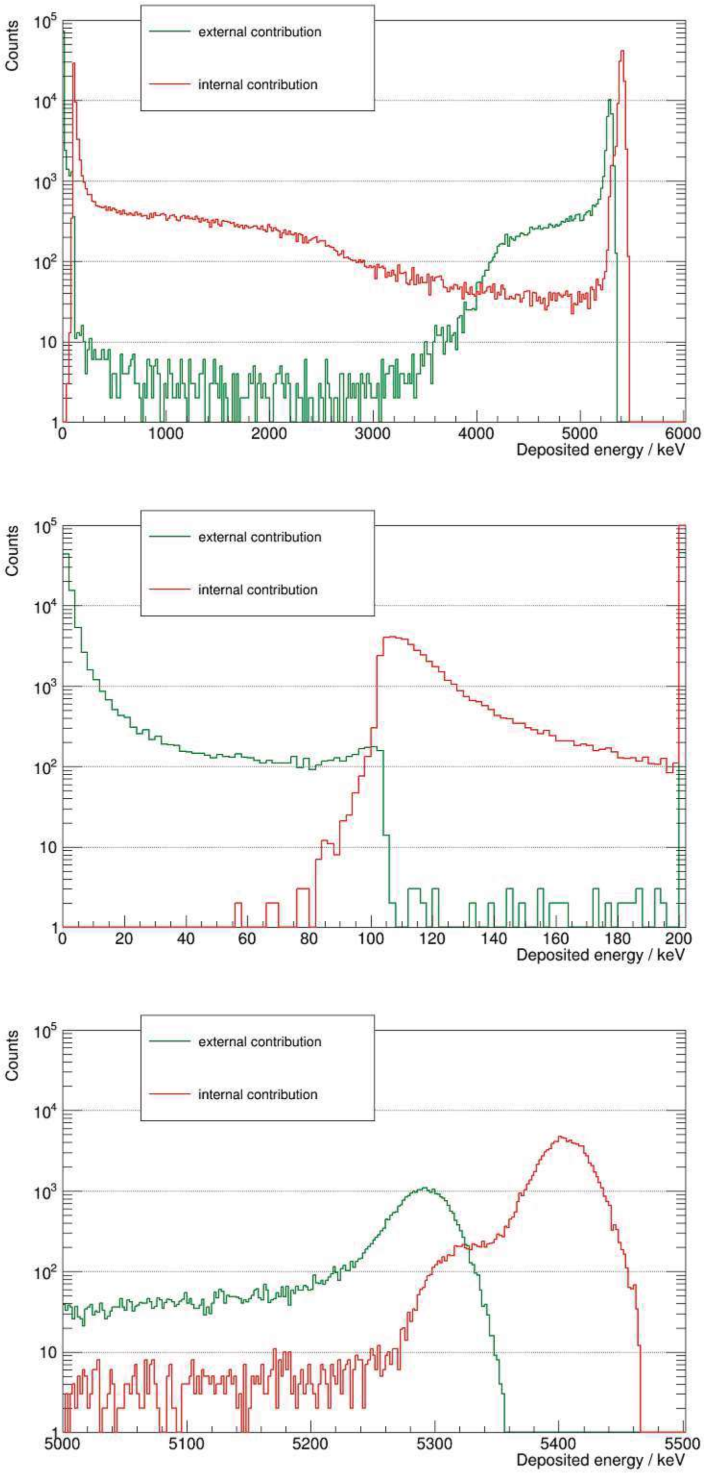

Figure B.8: Comparison of the energy deposition spectra of ^{210}Po placed below the surface of an external source (labeled external contribution) and the target crystal (labeled internal contribution) separately, following a simulated distribution based on the ^{222}Rn decay chain. Both, the external source and the target crystal are out of $CaWO_4$ and have a roughness represented by 5 µm high and wide spikes. The contaminated and roughened surface of the source and the target are facing each other with a distance of approximately 0.5 cm. Detector resolution of TUM40 is applied to the data. Three different energy ranges are presented: 0-6000 keV (top), 0-200 keV (middle), and 5000-5500 keV (bottom).

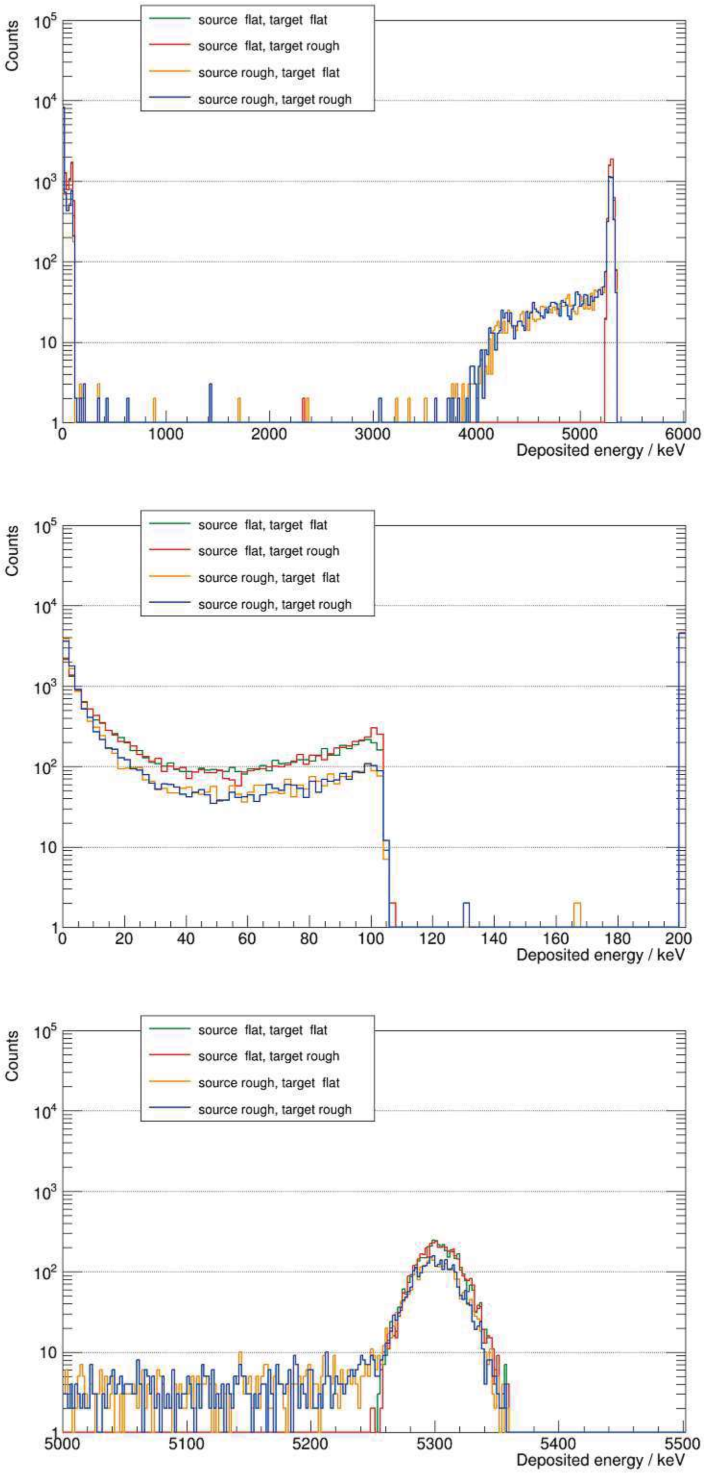

Figure B.9: ^{210}Po are uniformly placed in a 10 nm thick layer below the surface of an external rough surface facing the target crystal with a distance of $\sim$ 0.5 cm. Both, the external source and the target crystal are out of $CaWO_4$ and are either polished or have a roughness represented by 5 µm high and wide spikes. Detector resolution of TUM40 is applied to the data. Three different energy ranges are presented: 0-6000 keV (top), 0-200 keV (middle), and 5000-5500 keV (bottom).

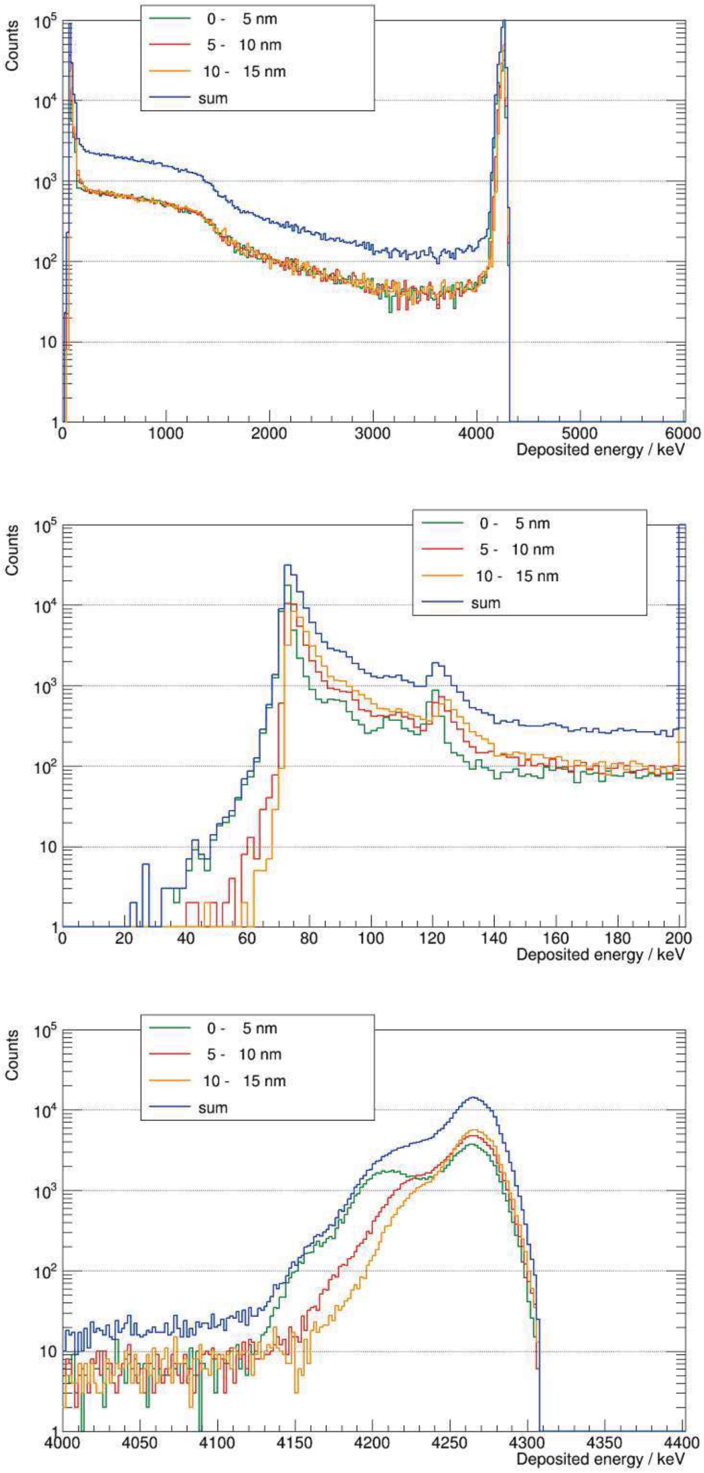

Figure B.10: ^{238}U are uniformly placed in three 5 nm thick layers below the rough surface of the detector crystal out of $CaWO_4$. The roughness is represented by 5 µm high and wide spikes. Detector resolution of TUM40 is applied to the data. Three different energy ranges are presented: 0-6000 keV (top), 0-200 keV (middle), and 4000-4400 keV (bottom).

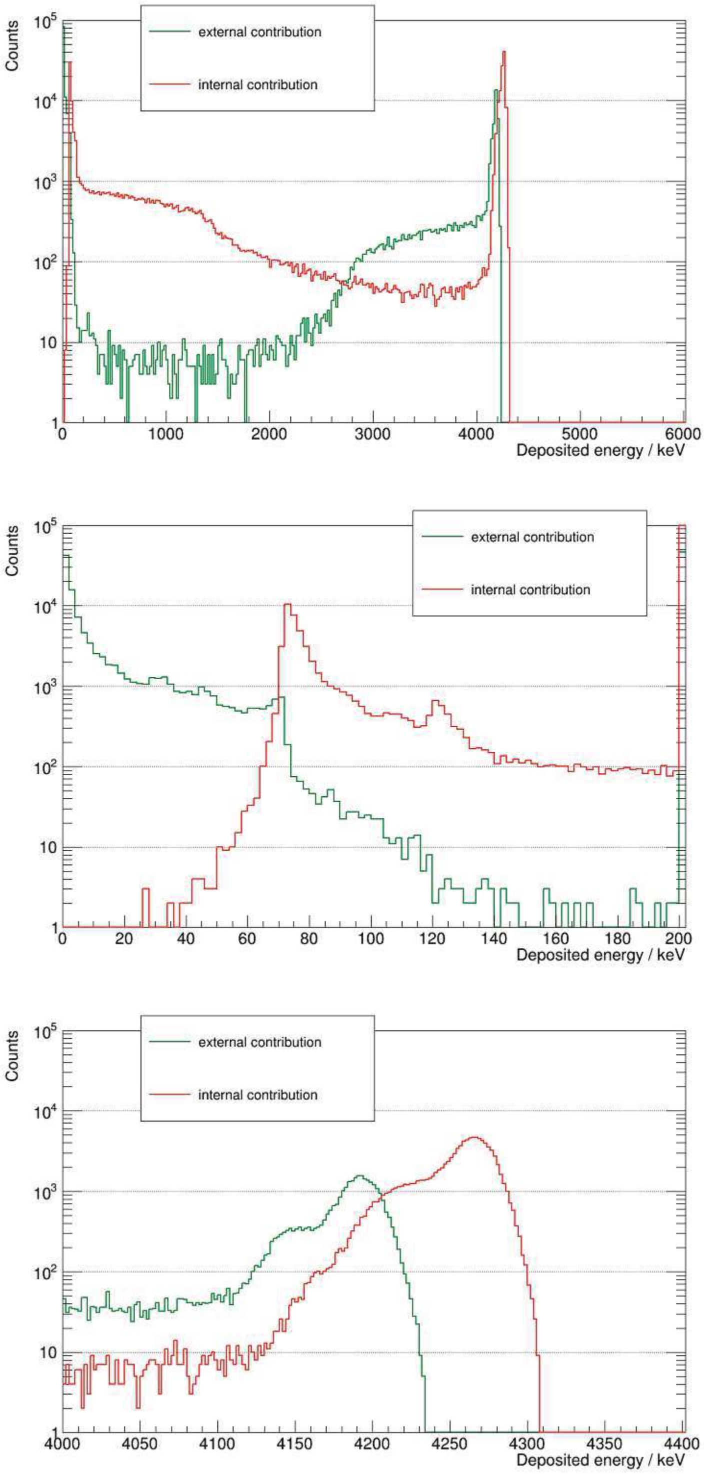

Figure B.11: ^{238}U are uniformly placed in 15 nm thick layers below the rough surface of an external and the target crystal. The contaminated surface of the external crystal is facing the target crystal with a distance of $\sim$ 0.5 cm. The rough surfaces are represented by spikes with 5 µm height and width. Detector resolution of TUM40 is applied to the data. Three different energy ranges are presented: 0-6000 keV (top), 0-200 keV (middle), and 4000-4400 keV (bottom).

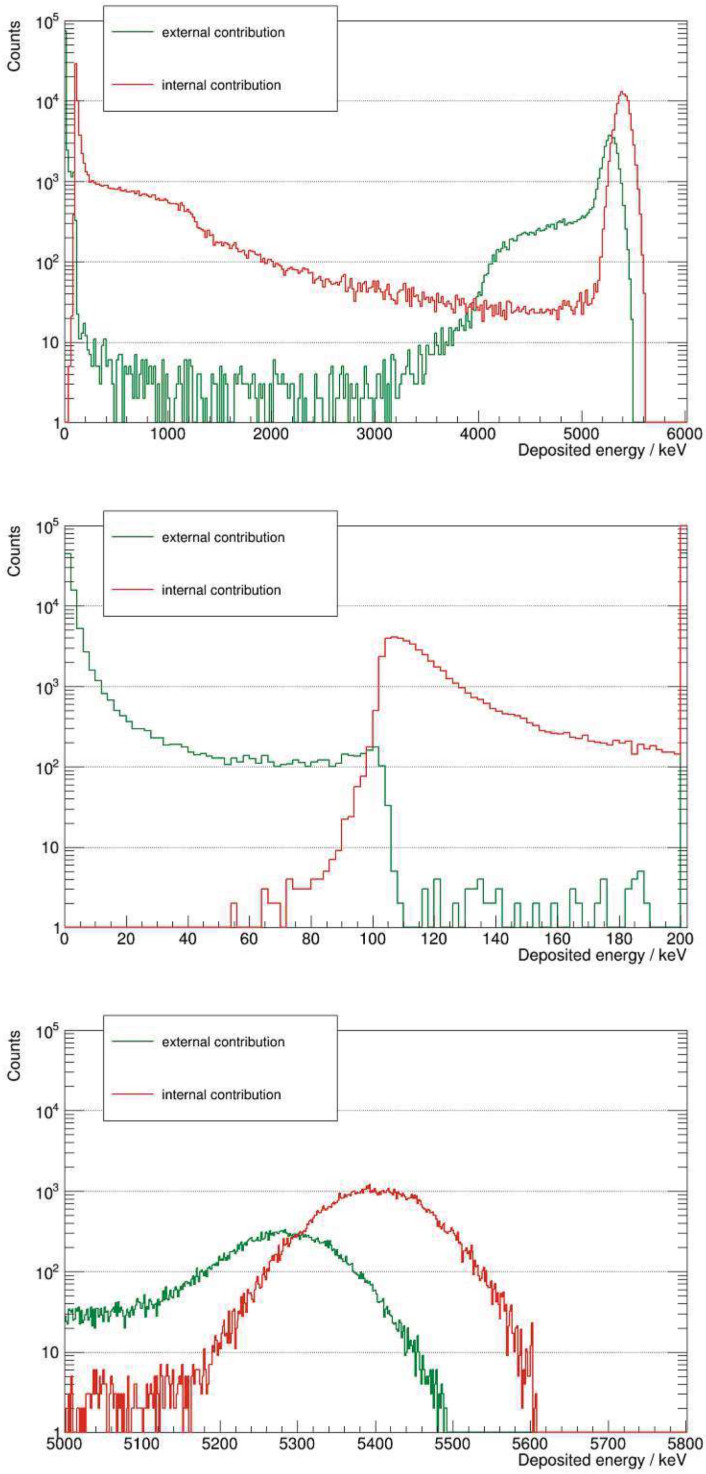

Figure B.12: Comparison of the energy deposition spectra of ^{210}Po placed below the surface of an external source (labeled external contribution) and the target crystal (labeled internal contribution) separately, following a simulated distribution based on the ^{222}Rn decay chain. Both, the external source and the target crystal are out of $CaWO_4$ and have a roughness represented by 5 µm high and wide spikes. The contaminated and roughened surface of the source and the target are facing each other with a distance of approximately 0.5 cm. Detector resolution of DetA is applied to the data. Three different energy ranges are presented: 0-6000 keV (top), 0-200 keV (middle), and 5000-5800 keV (bottom).

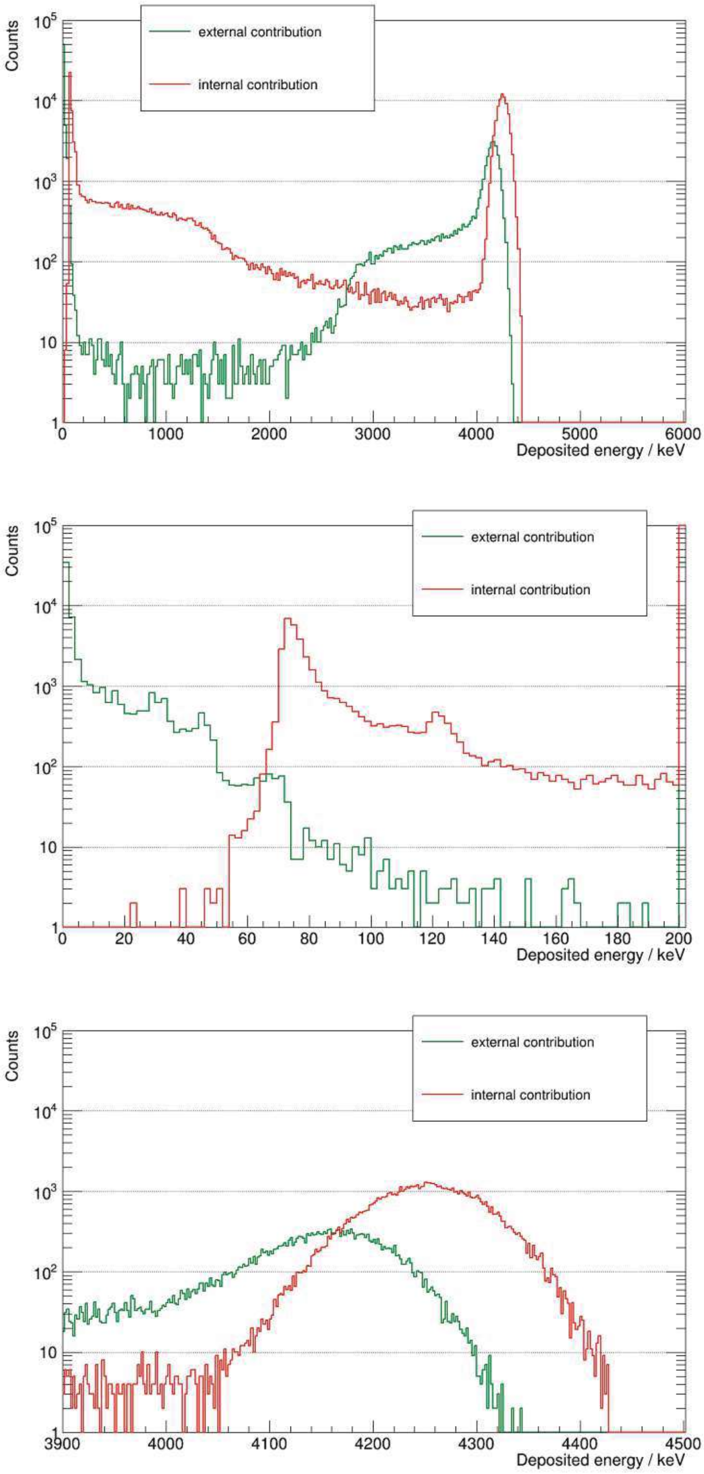

Figure B.13: ^{238}U are uniformly placed in 15 nm thick layers below the rough surface of an external and the target crystal. The contaminated surface of the external crystal is facing the target crystal with a distance of ~ 0.5 cm. The rough surfaces are represented by spikes with 5 µm height and width. Detector resolution of DetA is applied to the data. Three different energy ranges are presented: 0-6000 keV (top), 0-200 keV (middle), and 3900-4500 keV (bottom).